Mobile to Mobile Channel Modelling for Wireless Communications

Prasad T Samarasinghe

B.Sc.(Honours) (University of Moratuwa, Sri Lanka)
M. Eng. (University of Moratuwa, Sri Lanka)

November 2013

A thesis submitted for the degree of Doctor of Philosophy
of The Australian National University

Australian National University

Research School of Engineering
College of Engineering and Computer Science
The Australian National University

Declaration

The contents of this thesis are the results of original research and have not been submitted for a higher degree to any other university or institution.

Much of the work in this thesis has been published or to be submitted for publication as journal papers or conference proceedings. These papers are:

Published

1. P.T. Samarasinghe, R.A. Kennedy, T.D. Abhayapala, and T.A. Lamahewa, Space-time cross correlation between signals at moving receiver, in Information, Communications and Signal Processing, 2009. ICICS 2009. 7th International Conference on, Macau, China, Dec. 2009, pp. 1-5.
2. P. T. Samarasinghe, T. A. Lamahewa, T. D. Abhayapala, and R. A. Kennedy, 3D mobile-to-mobile wireless channel model, in Australian Communications Theory Workshop (AusCTW), Canberra, Australia, Feb. 2010, pp. 30-34.
3. P. T. Samarasinghe, T. A. Lamahewa, T. D. Abhayapala, and R. A. Kennedy, 2D Mobile-to-Mobile wireless channel model, in Signal Processing and Communication Systems (ICSPCS), 2010 4th International Conference on, Gold Coast, Australia, Dec. 2010, pp. 1-6.
4. P. T. Samarasinghe, T. D. Abhayapala, T. A. Lamahewa, and R. A. Kennedy, Second-order statistics of 2D non-isotropic mobile-to-mobile wireless channels, in Personal Indoor and Mobile Radio Communications (PIMRC), 2011 IEEE 22nd International Symposium on, Toronto, Canada, Sep. 2011, pp. 1667-1671.

Submission pending

1. P. T. Samarasinghe, T. D. Abhayapala, T. A. Lamahewa, and R. A. Kennedy, Generalized Level-Crossing Rate and Average Fade Duration in 2D and 3D Mobile-to-Mobile Wireless Channels, EURASIP Journal on Wireless Communications and Networking.
2. P. T. Samarasinghe, T. D. Abhayapala, T. A. Lamahewa, and R. A. Kennedy, Space-Frequency Correlation in Mobile-to-Mobile Multi-carrier Systems, International Journal of Antennas and Propagation.

The research represented in this thesis has been performed jointly with Prof. Rodney A. Kennedy, Prof. Thushara D. Abhayapala, Dr. Tharaka A. Lamahewa. The substantial majority of this work was my own.

Prasad T. Samarasinghe
Research School of Engineering ,
The Australian National University,
Canberra ACT 0200,
Australia.

Acknowledgements

There are many who deserve my sincere thanks. First and foremost, I would like to express my sincere gratitude to Prof. Rodney Kennedy and Prof. Thushara Abhayapala for their continuous support, patience, motivation, enthusiasm, and immense knowledge. This thesis would never be a reality if not for the review, comments and guidance of them. I am indebted to Prof. Kennedy for motivating me to complete this thesis. Prof. Abhayapala should be specially mentioned in introducing me to the ANU research community and most importantly understanding me at difficult situations.

My sincere thanks to Dr. Tharaka Lamahewa for his guidance, support and friendship during my research at ANU. All the members of the Signal Processing group are thanked for the friendly and supportive research environment, specially Ms. Lesley Goldburg and Ms. Elspeth Davies, for their assistance in administrative work.

My parents are also mentioned for the encouragement and best wishes given to me. I appreciate the patience and cooperation of my children all throughout.

Finally, I would like to thank my wife, Pradeepa. She was always there cheering me up and standing by me through the good and bad times .

Abstract

Wireless communication has been experiencing many recent advances in mobile to mobile (M2M) applications. M2M communication systems differ from conventional fixed to mobile systems by having both transmitter and receiver in low elevation and in motion. This raises the need to come up with new channel models and perform statistical analysis on M2M communication channels looking from a different perspective. This need motivated us to perform the research outlined in this thesis.

In reviewing the literature we found that though in general the M2M channel models are sparse, a major gap exists in the non geometrical stochastic based mathematical channel models. In filling this gap, we develop a novel mathematical non geometrical stochastic multiple input multiple output (MIMO) M2M channel model for two dimensional (2D) and three dimensional (3D) scattering environments. This model is based on the underlying physics of free space wave propagation and can be used as a framework for any environment by selecting suitable complex scattering gain functions. In addition, we extend this novel model to multicarrier M2M which is the first multicarrier channel model in the non geometrical stochastic M2M category.

Based on our novel M2M channel model, we carry out an extensive analysis in space-time correlation, space-frequency correlation and second order channel statistics. With the choice of suitable parameters, this analysis and channel model can be used for any wireless environment. Thus, we claim that our novel channel model together with the analysis performed in this thesis can be taken as a generalized framework.

A significant contribution of our analysis is the consideration of the impact of transmitter and receiver speed to space-time and space-frequency correlation,

which is not available in the literature. Using a von Mises-Fisher distribution as the angular power distribution, the usefulness of the derived temporal correlation function is discussed. The simulation results corroborate the fact that both space-time and space-frequency correlations are reduced when transmitter or receiver speed increases. The rate of reduction of space-time correlation in von Mises-Fisher distribution scattering environment is more than in the isotropic environment.

Under second order channel statistics, we consider Rice, Rayleigh and Nakagami fading channels in four different non-isotropic scattering environments with angle of departure (AoD) and angle of arrival (AoA) distributions given by (i) separable Truncated Gaussian, (ii) separable von-Mises, (iii) truncated Gaussian bivariate and (iv) truncated Laplacian bivariate distributions. We show that the major second order statistics, namely, the level crossing rate (LCR) and the average fade duration (AFD), in different fading channels can be expressed in terms of known scattering coefficients of the AoD and AoA distributions.

As the channel models and their respective measurements provide reliable knowledge of the channel for the design and analysis of M2M systems, the proposed channel model and the corresponding analysis will be useful for the design, testing and performance evaluation of future M2M communication systems.

List of Acronyms

2D	two dimensional
3D	three dimensional
AAoA	main azimuth angle of Arrival
AAoD	main azimuth angle of departure
AFD	average fade duration
AoA	angle of arrival
AoD	angle of departure
ARN	aeronautical radio navigation
AWGN	additive white Gaussian noise
CDF	cumulative distribution function
DB	double bounced
DSRC	dedicated short range communication
EAoA	main elevation angle of arrival
EAoD	main elevation angle of departure
F2M	fixed to mobile
FDTD	finite difference in time domain
GBSPM	geometry based stochastic physical models
GSA	global mobile suppliers association
IFFT	inverse fast fourier transform
ITS	intelligent transportation systems
LCR	level crossing rate
LoS	line of sight

LS	Line Spectrum
LTE	long term evolution
M2M	mobile to mobile
MGTR	modified geometrical two ring
MIMO	multiple input multiple ouput
MLS	microwave landing system
MMEDS	Modified Method of Exact Doppler Spreads
MoM	method of moments
NGSPM	non geometrical stochastic physical models
NLoS	non line of sight
OFDM	orthogonal frequency division multiplexing
PDF	probability distribution function
PER	packet error rate
PSD	power spectral density
RT	ray tracing
SBR	single bounced receive
SBT	single bounced transmit
SBTR	single bounce two ring
SBTS	single bounce two sphere
SISO	single input single ouput
SoS	sum of sinusoids
SS	spectrum sampling
STF	space-time frequency
TDL	tap delay line
VANET	vehicular ad hoc networks
VBS	virtual base stations
WAVE	wireless access in a vehicular environment
WLAN	wireless local area network

Notations

$\boldsymbol{A}^T$	transpose of matrix $\boldsymbol{A}$
$\boldsymbol{a}^T$	transpose of vector $\boldsymbol{a}$
$\boldsymbol{a}^*$	complex conjugate of vector $\boldsymbol{a}$
$\boldsymbol{a} \cdot \boldsymbol{b}$	denotes the inner product between vectors $\boldsymbol{a}$ and $\boldsymbol{b}$.
$\| \boldsymbol{a} \|$	euclidian norm of vector $\boldsymbol{a}$
$\| \boldsymbol{A} \|^2$	squared norm of matrix $\boldsymbol{A}$
$\lvert \boldsymbol{A} \rvert$	determinant of matrix $\boldsymbol{A}$
$\delta(\cdot)$	Dirac delta function
$E\{\cdot\}$	mathematical expectation
$\boldsymbol{I}_n$	$n \times n$ identity matrix
$\mathbb{S}^1$	unit circle
$\mathbb{S}^2$	unit sphere

List of Figures

List of Tables

Contents

Chapter 1

Introduction

We present a brief introduction to mobile to mobile (M2M) communication systems emphasizing their potential for fulfilling the high capacity demands in future mobile wireless communication networks. We motivate the research and summarize the main thesis contributions. In the final section we provide an outline and organization of the thesis.

1.1 An Overview of M2M Systems

In the literature one can find various definitions for M2M systems. Some refer to it as "machine to machine communications" where technologies allow both wireless and wired systems to communicate with other devices with the same ability, while others refer to "mobile to mobile" communications where technologies allow both ends of the wireless systems to communicate while they are moving. In this thesis we focus on the latter mobile to mobile communication.

A communication system in which both the transmitter and receiver are in motion is referred to as a M2M communication system. These systems differ from conventional fixed to mobile (F2M) radio systems where the base station is fixed and its elevation is typically high. In modern communications, such as inter-vehicular communications, mobile ad hoc wireless networks, relay-based cellular radio networks and intelligent transport systems, M2M systems play a major role [1].

In inter-vehicular communications, a main moving vehicle communicates with one or more other moving vehicles in different locations. This situation is a common scenario in cases of emergency or disaster events between rescue squads, emergency vehicles and military or security squad vehicles [2].

Mobile ad hoc networks can be viewed as a collection of autonomous nodes or terminals that communicate together by forming a multi-hop radio network where connectivity is decentralized [3]. The individual nodes can join or leave the network at any time and because of the node movements, their network topology may be temporal (time-varying). Various types of new networks, such as vehicular ad hoc networks (VANET), emerged as a result of the development in mobile ad hoc networks. VANETs have the ability to provide communication between vehicles and between vehicles and road side units. In addition VANETs play an important role in recently introduced concepts such as smart cities and living labs and give the benefits of pollution and congestion reduction, accidents prevention and safer roads [4].

Relays in wireless networks are commonly used to extend the coverage and increase the capacity of the network. Relay-based cellular radio networks mainly consist of a base station, a few relay stations and a large number of mobile stations [2].

Intelligent transport systems will play an important role in a more efficient use of existing infrastructure. The safety and reliability demands of these systems are extremely important since driver functions are (partly) automated [5]. Dedicated short range communication (DSRC) and wireless access in a vehicular environment (WAVE) are emerging standards for intelligent transport systems focussed on improving traveler safety, efficiency and productivity [6].

The dedicated IEEE standard for vehicular communications is 802.11p, also known as WAVE (IEEE, 2010). The European equivalent is the ETSI standard intelligent transportation systems (ITS)-G5 (ETSI, 2010). Both standards operate in the 5.9 GHz band and are mainly based on the well-known wireless local area network (WLAN) standard IEEE 802.11a (IEEE, 2007).

In order to enhance the performance of M2M communication systems for the applications given above and to meet the challenges introduced by the development of future M2M radio transmission systems, a detailed understanding of M2M radio

channels is essential.

1.2 Research Framework

The main objectives of the thesis including a brief motivation followed by a summary of our contributions are given in this section.

1.2.1 Motivation

As per the statistics given by Global mobile Suppliers Association (GSA), by the end of year 2012 global mobile market consisted of 6.39 billion subscriptions including 68.33 million long-term evolution (LTE) subscribers. Though research in the F2M discipline is matured, M2M research is still in its infancy. In order to cater the growing demand for M2M applications, extensive M2M research is essential, especially in the physical layer as even a small improvement in the physical layer may result in order of magnitude improvement in the real application. This need motivates us to carry out our research to develop novel realistic channel models together with extensive analysis.

1.2.2 Specific Contributions

In designing and developing wireless M2M communication systems, channel modeling and simulations play a major role. The available M2M channel model categorization in the literature is depicted in Fig. 1.1 where our contributions in this thesis lie in the areas labeled in bold.

Specifically, the contributions from our research in the areas mentioned above can be summarized as follows.

- Under stochastic channel models, though, one can find many geometry based models in the literature, non geometry based models are very sparse. In filling this gap, we introduce our novel mathematical non geometrical stochastic M2M channel model for two dimensional (2D) and three dimensional (3D) scattering environments in Chapter 3. This model is based on the underlying

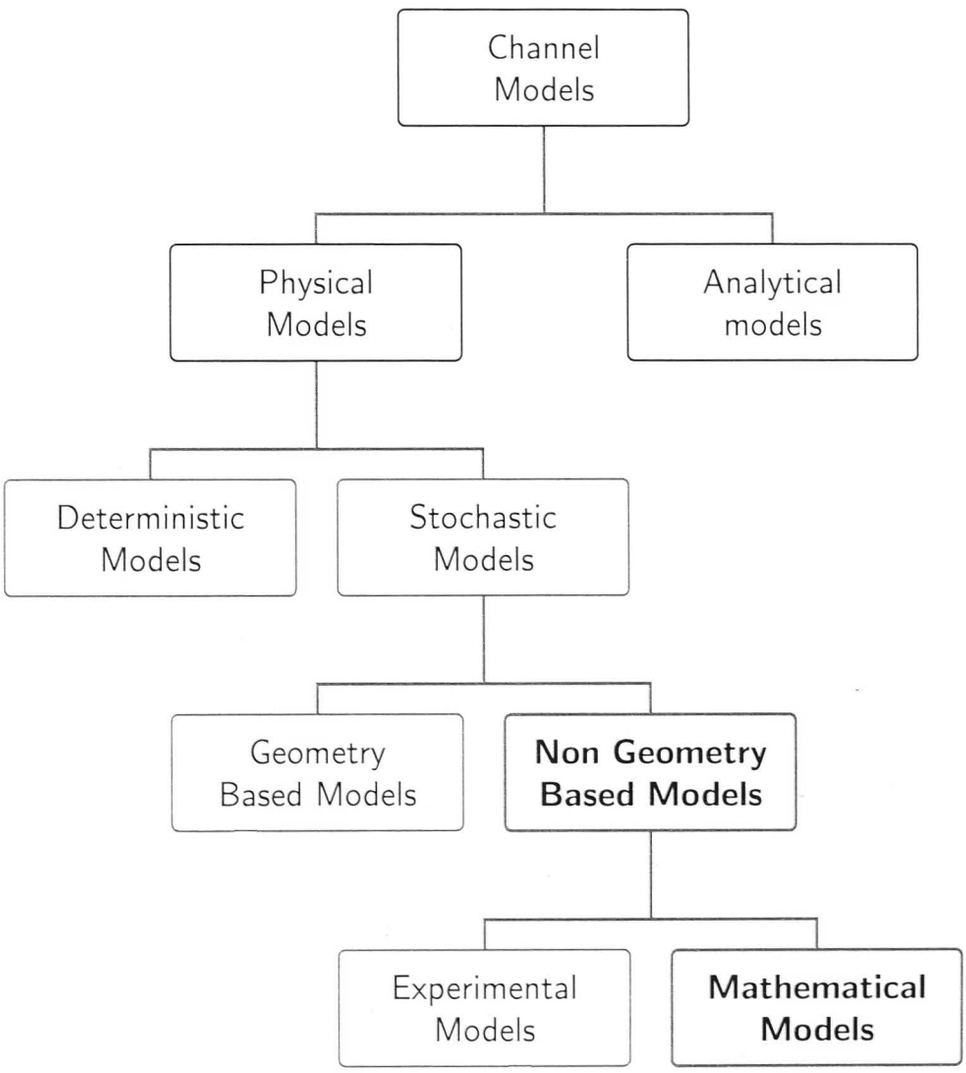

Figure 1.1: The available M2M channel model categorization (Thesis contribution areas are indicated in bold).

physics of free space wave propagation and can be used as a framework for any environment by selecting suitable complex scattering gain functions.

- Further, we extend this novel model to multicarrier M2M which is the first multicarrier channel model in the non geometrical stochastic M2M category.
- In addition, we carry out an extensive analysis in space-time correlation, space-frequency correlation and second order channel statistics on our novel M2M channel model. With the choice of suitable parameters, these analyses and channel models can be used for virtually any wireless environment. Thus, we claim that our novel channel model together with the analysis performed in this thesis can be taken as a generalized framework.
- A significant contribution of our analysis is the consideration of the impact of transmitter and receiver velocities on space-time and space-frequency correlation, which is not available in the literature prior to our work.

1.3 Thesis Outline

The rest of this thesis is organized as follows:

Chapter 2 – categorizes most of the M2M channel models available in the literature. Together with the models, we discuss the available channel measurements and simulation methods for M2M. The last section of Chapter 2 presents an summary of the chapter.

Chapter 3 – introduces our novel M2M channel model for 2D and 3D scattering environments, which can be used as a framework for any scattering environment by selecting a suitable scattering gain function. We claim this novel model to be the only available mathematical non geometrical stochastic M2M channel model to be found the literature to date. In addition, this model is further extended to obtain the multicarrier M2M channel model.

Chapter 4 – develops space-time cross correlation and channel temporal correlation for the M2M channel model introduced in Chapter 2, which is for both 2D and 3D scattering environments. Further, this chapter discusses

the effect of transmitter velocity, receiver velocity, angle of arrival (AoA) and angle of departure (AoD) on channel temporal correlation in addition to the effects of time delay and receiver antenna spacings in 2D and 3D M2M scattering environments.

Chapter 5 – scrutinizes the impact of space-frequency correlation in multicarrier M2M channel model for 2D and 3D scattering environments. As shown in the literature, space-frequency correlation will help design multiple antenna transmitters and receivers. Thus, an analysis of space-frequency correlation simulations for multicarrier M2M channel model is given in this chapter.

Chapter 6 – focuses on second-order channel statistics, mainly level crossing rate and average fade duration for the novel M2M channel model. We corroborate the analysis with simulations and those results with available experimental results in the literature.

Chapter 7 – concludes the thesis elaborating on the main findings and pointing out future research directions.

Chapter 2

Review of Mobile to Mobile Channel Models, Measurements and Simulations

Modeling the propagation channel in communication systems has been of interest from the beginnings of such systems, as it helps in performance evaluation, parameter optimization, and testing of such systems. With the advancement in mobile to mobile (M2M) communication systems, the need for better channel models arises. Many researchers have contributed towards this need and a collection of channel models can be found in the literature. We have summarized the categories of these existing channel models, as shown in Fig. 1.1 from Chapter 1.

In analyzing the literature we have found many drawbacks as well as opportunities for improvement in channel models. While this chapter gives details on the existing M2M channel models, the chapters to follow point out when and where our novel channel model surpasses the models described in this chapter. The first part of this chapter deals with the available M2M channel models while the latter sections discuss channel measurements related to M2M channels and available simulation methods.

2.1 Channel Modeling

The term channel refers to the medium between the transmitting antenna and the receiving antenna. As the wireless signal travels from the transmitting antenna to the receiving antenna, its characteristics change based on the distance between the two antennas, the path(s) taken by the signal, transmitter velocity, receiver velocity and the environment around the path. The channel can consist of a number of components which may cause the transmitted signal to undergo multiple reflections, refractions, and diffractions. Reliable transmission of a signal through a communication channel faces challenges such as delay and phase shift, noise and interference, path loss and shadowing [7]. In order to determine the characteristics of the received signal from the transmitted signal, we can model the medium between the transmitter and receiver. This model of the medium is called channel model.

Modeling parameters can be decided mainly based on temporal aspects and spatial aspects. While fading signal envelopes, Doppler shifts of received signals and received power level distributions are the main components in temporal aspects, spatial aspects characterize the angle of arrival, angle of departure and the distribution of arriving waves.

2.2 Mobile to Mobile Channel Modeling

Recently introduced M2M communication systems permit both transmitter and receiver to be mobile whereas the earlier fixed to mobile (F2M) radio channels had the base station fixed. These M2M systems have become an essential part in modern communication such as inter-vehicular communications, mobile ad hoc wireless networks, relay-based cellular radio networks and intelligent transport systems [1]. In modeling M2M systems we face additional challenges in both the transmitter movement and having a more challenging scattering environment around the transmitter.

In order to face those additional challenges and upcoming problems in M2M channel modeling, a literature review was performed as the first step of our research. This literature review will be detailed in this chapter starting with our

classification of existing M2M channel models.

2.3 M2M Channel Model Classification

This section is devoted for the analysis of currently available M2M channel models. The models proposed so far can be mainly categorized based on the type of channel that is being considered or the modeling approach taken. Few of the common models under channel type are narrowband (flat fading) versus wideband (frequency selective) models and time-varying versus time-invariant models. As the main aim of our thesis is based on the analysis of M2M channel modeling, we perform the classification of channel models with the modeling approach.

In approaching M2M channel models, we first present the existing classification of F2M channels referenced in [8]. Under this classification, F2M channels are broadly divided into physical models and analytical models. The main difference in these two classification is that analytical models consider wave propagation together with antenna configuration while physical models consider the propagation mechanisms independent of the antenna configuration [8].

Physical channel models can be further split into:

Deterministic models – where the physical propagation parameters are characterized in a completely deterministic manner (examples are ray tracing and stored measurement data),

Geometry-based stochastic models [2, 9–11] – where the model is characterized by the laws of wave propagation applied to specific transmitter (Tx), receiver (Rx), and scatterer geometries, which are chosen in a stochastic manner, and

Non geometric stochastic models [12] – where physical parameters (angle of departure (AoD), angle of arrival (AoA), delay, etc.) are determined in a completely stochastic way by prescribing underlying probability distribution functions without assuming an underlying geometry.

This characterization appears in [13].

Similarly analytical models can also be divided mainly into propagation motivated models and correlation-based models. While the first model characterizes the impulse response through propagation parameters the latter models the channel matrix statistically in terms of the correlations between the matrix entries. Popular models under the propagation-motivated models include finite scatterer model [14], the maximum entropy model [15], and the virtual channel representation [16] while Kronecker model [17] and the Weichselberger model [18] are for the correlation-based models.

We extend the above F2M classification to M2M channel models. The available M2M models in the literature could be categorized only under physical models and each of the sub-models for M2M will be discussed in detail in the sections to follow.

2.3.1 Deterministic Physical Models

The goal of deterministic physical models (DPM) is to reproduce the physical radio propagation process for a given environment. This is achieved through storing the geometric and electromagnetic characteristics of the environment in files and simulating the process. As the DPM are based on the environment reproduction, their results have a good level of accuracy and they can be used to replace measurements where it is difficult to carry out the measurement process in real world. The main drawback of these models is that each model represent one specific environment at a given time and multiple runs are needed to represent different environments [8].

A variety of models are discussed under DPM such as method of moments (MoM), finite difference in time domain (FDTD) and ray tracing (RT) models. Out of these, RT models are considered to be the most appropriate for radio propagation, at least in urban areas. RT models use the theory of geometrical optics to treat reflection and transmission on plane surfaces and diffraction on rectilinear edges [19]. As RT models consider waveguiding effects and diffraction effects they are proved to give very accurate results. For M2M channel models, RT model is the only model available under deterministic physical model category.

The first RT model for M2M was introduced in [20] where the approach consists of three major parts: the modeling of the road traffic, the modeling of the environment adjacent to the road lane and the modeling of the wave propagation between

the vehicles. A ray-optical approach is used to model the wave propagation, which allows for wideband as well as narrowband analysis of the channel.

2.3.2 Geometry-Based Stochastic Physical Models

The Geometry-Based Stochastic Physical Models (GBSPM) are similar to RT models discussed above but the difference between them is that the locations of the scatterers of GBSPM are taken from a statistical distribution [21]. The main advantage of GBSPM is its adaptability to different scenarios by changing the shape of the scattering region such as one-ring, two-ring, etc. [21]. The first GBSPM for isotropic single input single output (SISO) M2M Rayleigh fading channels was proposed in [2]. The available GBSPM are discussed in this section and the symbols used are summarized in Table 2.1 and Table 2.2.

Akki and Harber Model

Akki and Harber [2] were the first to propose a M2M channel model. This channel model is based on the concept that the scatterers and reflectors in the vicinity of the mobile transmitter will scatter or reflect most of the transmitted energy and will tend to modify the directional pattern of the transmitting antenna. A basic assumption used in this model is that omnidirectional antennas are used by both transmitting and receiving vehicles. By taking Re $\{A_0 u(t) e^{j\omega_0 t}\}$ as the transmitted signal ($u(t) = e^{j\omega t}$) and $\Delta\phi$ as the received signal due to scatterers and reflectors in the incremental angle around the azimuthal ϕ_{Ri}, the channel as a filter with time-varying transfer function $H(f,t)$ is given by

$$H(f,t) = \sum_{i=1}^{n} Q(\phi_{Ri}, t) e^{-j(\omega_0+\omega)\tau_i}, \tag{2.1}$$

where the radial frequencies ω_0 and ω are carrier and input signal frequencies, respectively. The signal is assumed to be received from n azimuthal angles and $Q(\phi_{Ri}, t)$ is defined as a complex Gaussian process whose magnitude value is the

Parameter description	Symbol
Local scatterers around the transmitter	$S_T^{(m)}(m = 1, 2, \dots)$
Local scatterers around the receiver	$S_R^{(n)}(n = 1, 2, \dots)$
AoD	$\phi_T^{(m)}$
AoA	$\phi_R^{(n)}$
The distance between the transmitter and the receiver	D
The antenna spacings at the transmitter	δ_T
The antenna spacings at the receiver	δ_R
Radius of local scatterers around the transmitter	R_T
Radius of local scatterers around the receiver	R_R
The tilt angle between the x-axis and the orientation of the antenna array at the transmitter	β_T
The tilt angle between the x-axis and the orientation of the antenna array at the receiver	β_R
The transmitter velocity	v_T
The receiver velocity	v_R
The angle of Transmitter motion	α_T
The angle of Receiver motion	α_R
The numbers of local scatterers around the transmitter	M
The numbers of local scatterers around the receiver	N
Free space wave number	$k_0 = 2\pi/\lambda$
Carrier wavelength	λ
Maximum Doppler frequencies caused by the movement of the transmitter	$f_{T_{max}} = v_T/\lambda$
Maximum Doppler frequencies caused by the movement of the receiver	$f_{R_{max}} = v_R/\lambda$
Transmitter antenna elements	n_T
Receiver antenna elements	n_R

Table 2.1: Parameters used in Geometry-Based Stochastic Physical Models

envelope of the signal received from the azimuthal angle $\phi_{Ri} \pm \Delta\phi/2$. Then,

$$Q(\phi_{Ri}, t) = r_i e^{j[(\omega_{Ri}+\omega_{Ti})t+\phi_i]}, \tag{2.2}$$

where r_i is a Rayleigh distributed random variable and ϕ_i' is uniformly distributed in $[0, 2\pi)$ with

$$\phi_i = \phi_i' - (\omega_{Ri} + \omega_{Ti})\tau_i, \tag{2.3}$$

where τ_i denotes the central (mean) value of time delay. The radial frequencies ω_{Ri} and ω_{Ti}, are independent Doppler shifts given by

$$\omega_{Ri} = \frac{2\pi}{\lambda} v_R \cos\phi_{Ri}, \tag{2.4}$$

and

$$\omega_{Ti} = \frac{2\pi}{\lambda} v_T \cos\phi_{Ti}, \tag{2.5}$$

where ϕ_{Ri} and ϕ_{Ti} are random angles of incidence on the receiver and on the scatterers near the transmitter, respectively. They are assumed to be independent.

The final transfer function of this channel model becomes,

$$H(f, t) = \sum_{i=1}^{n} r_i e^{j[(\omega_{Ri}+\omega_{Ti})t+\phi_i]} e^{-j\omega\tau_i}. \tag{2.6}$$

The channel model shows that each path is dispersive in both time and frequency, and reduces to time dispersive path if the mobile transmitter is stationary [2].

The Geometrical Two-Ring Model

The geometrical two-ring model for a narrowband M2M multiple input multiple output (MIMO) channel [22] as shown in Fig. 2.2 is discussed in this section.

Though for simplicity, an elementary antenna configuration where both the transmitter and the receiver are equipped with only two omnidirectional antennas is considered in this model, this model can be extended to any number of antennas. The transmitter and the receiver are assumed to be both mobile and no line of sight (LoS) path exists between them.

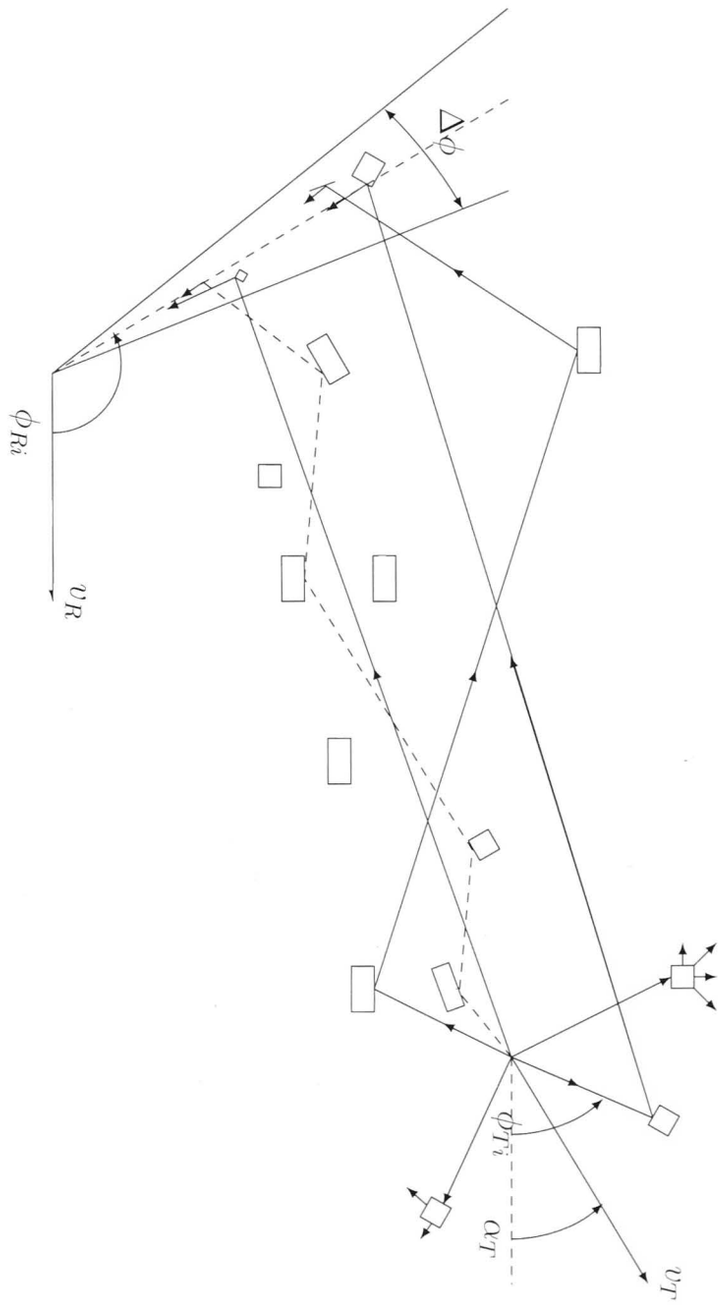

Figure 2.1: Akki and Harber model.

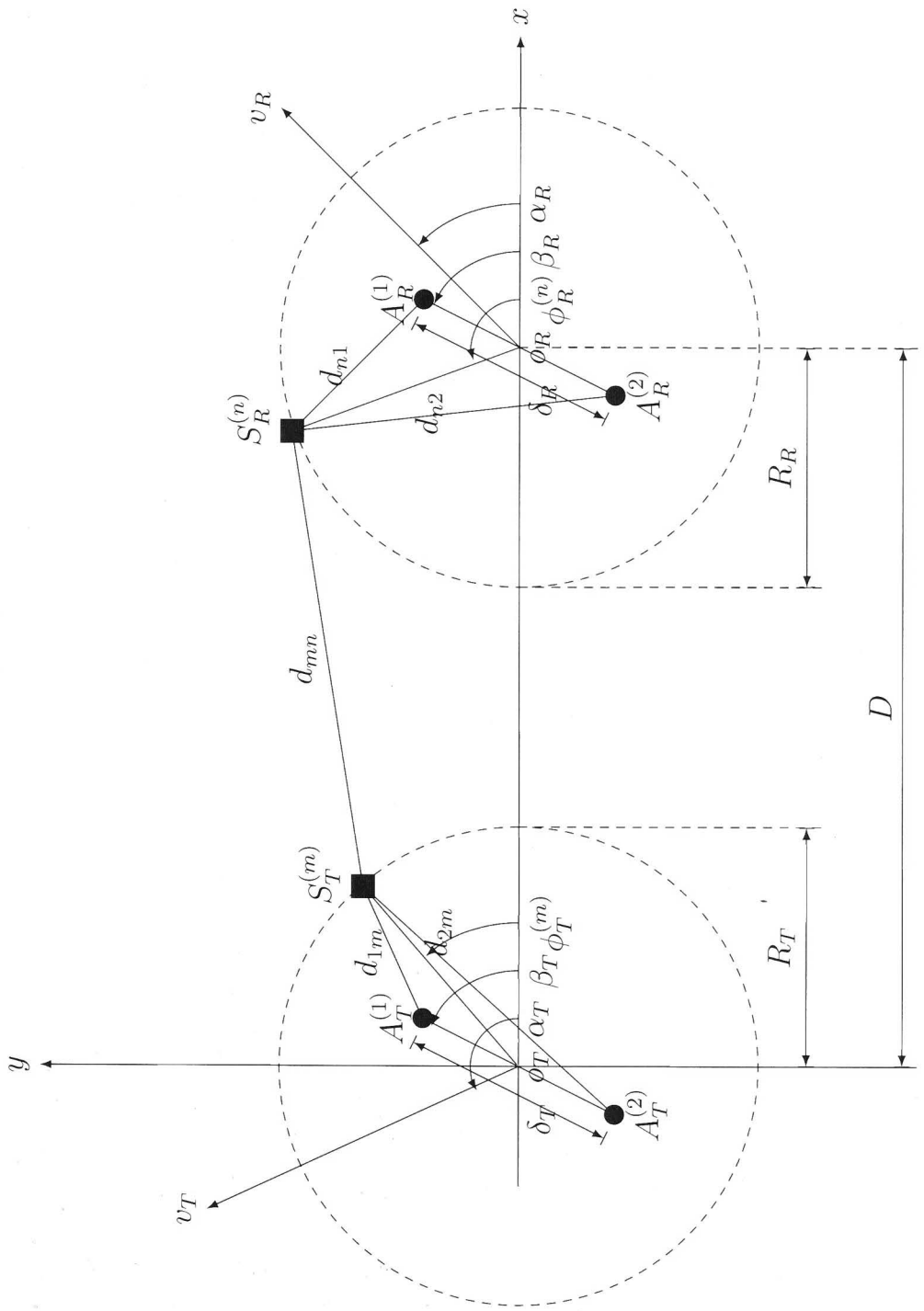

Figure 2.2: The geometrical two-ring model for a 2×2 MIMO channel with local scatterers around a mobile transmitter MS_T (left) and a mobile receiver MS_R (right).

General assumptions made on this model are:

1. The transmitter and the receiver are surrounded by a large number of local scatterers.

2. Due to the high path loss, the contributions of remote scatterers to the total received power are not considered, only local scattering is considered.

3. All waves reaching the receiver antenna array are equal in power.

4. The radii R_T and R_R are small in comparison with D.

5. Condition
$$\max\{\delta_T, \delta_R\} \ll \min\{R_T, R_R\}$$
applies as the antenna spacings δ_T and δ_R are generally small in comparison with the radii R_T and R_R.

6. Each scatterer $S_T^{(m)}$ on the ring around the transmitter introduces an infinitesimal constant gain $E_m = 1/\sqrt{M}$ and a random phase shift θ_m.

7. On the receiver side, each scatterer $S_R^{(n)}$ introduces a constant gain $E_n = 1/\sqrt{N}$ and a random phase shift θ_n.

8. The phase shifts θ_m and θ_n are assumed to be independent, identically distributed (i.i.d.) random variables with a uniform distribution over the interval $[0, 2\pi)$.

From the geometrical two-ring model shown in Fig. 2.2 we can observe that the m^{th} homogeneous plane wave is emitted from the first antenna element $A_T^{(1)}$ of the transmitter. This plane wave travels over the local scatterers $S_T^{(m)}$ and $S_R^{(n)}$ before received on the first antenna element $A_R^{(1)}$ of the receiver. Based on this, the diffuse component of the channel describing the link from $A_T^{(1)}$ to $A_R^{(1)}$ can be written as:

$$h_{11}(\vec{r_R}) = \lim_{M,N\to\infty} \sum_{m,n=1}^{M,N} E_{mn} e^{j(\theta_{mn} + \vec{k}_T^{(m)} \cdot \vec{r}_T - \vec{k}_R^{(n)} \cdot \vec{r}_R - k_0 D_{mn})}, \tag{2.7}$$

where E_{mn} and θ_{mn} denote the joint gain and joint phase shift caused by the interaction of the scatterers $S_T^{(m)}$ and $S_R^{(n)}$, respectively, $\overrightarrow{k}_T^{(m)}$ is the wave vector pointing in the propagation direction of the m^{th} transmitted plane wave, and $\overrightarrow{r}_T$ denotes the spatial translation vector of the transmitter, $\overrightarrow{k}_R^{(n)}$ is the wave vector pointing in the propagation direction of the n^{th} received plane wave, $\overrightarrow{r}_R$ denotes the spatial translation vector of the receiver, D_{mn} is the length of the total distance which a plane wave travels from $A_T^{(1)}$ to $A_R^{(1)}$ via the scatterers $S_T^{(m)}$ and $S_R^{(n)}$.

Based on the assumptions given above, the joint gains E_{mn} and joint phases θ_{mn} in (2.7) can be expressed as:

$$E_{mn} = E_m \cdot E_n = 1/\sqrt{MN} \tag{2.8}$$

$$\theta_{mn} = (\theta_m + \theta_n) \mod 2\pi \tag{2.9}$$

where mod denotes the modulo operation. The variables θ_{mn} are i.i.d. random variables uniformly distributed over $[0, 2\pi)$.

The phase changes $\overrightarrow{k}_T^{(m)} \cdot \overrightarrow{r}_T$ and $\overrightarrow{k}_R^{(n)} \cdot \overrightarrow{r}_R$ in (2.7) are due to the motion of the transmitter and receiver, respectively, and can be expressed as:

$$\overrightarrow{k}_T^{(m)} \cdot \overrightarrow{r}_T = 2\pi f_{T_{\max}} \cos(\phi_T^{(m)} - \alpha_T)t \tag{2.10}$$

$$\overrightarrow{k}_R^{(n)} \cdot \overrightarrow{r}_R = -2\pi f_{R_{\max}} \cos(\phi_R^{(n)} - \alpha_R)t \tag{2.11}$$

In this model, the $\phi_T^{(m)}$ and $\phi_R^{(n)}$ are independent random variables determined by the distribution of the local scatterers. Furthermore, the phase change $k_0 D_{mn}$ in (2.7) is due to the total distance traveled and can be written as:

$$k_0 D_{mn} = \frac{2\pi}{\lambda}(d_{1m} + d_{mn} + d_{n1}) \tag{2.12}$$

where d_{1m}, d_{mn} and d_{n1} are the lengths as illustrated in Fig. 2.2. These distances can be approximated by using $R_T \gg \delta_T$, $R_R \gg \delta_R$, and $\sqrt{1+x} \approx 1 + x/2 (x \ll 1)$ as follows:

$$d_{1m} \approx R_T - \frac{\delta_T}{2} \cos(\phi_T^{(m)} - \beta_T) \tag{2.13}$$

$$d_{mn} \approx D + R_R \cos\phi_R^{(n)} - R_T \cos\phi_T^{(m)} \tag{2.14}$$

$$d_{n1} \approx R_R - \frac{\delta_R}{2}\cos(\phi_R^{(n)} - \beta_R) \tag{2.15}$$

Finally, using the above equations, the diffuse component of the link from $A_T^{(1)}$ to $A_R^{(1)}$ is approximately expressed as:

$$h_{11}(t) = \lim_{M,N\to\infty} \frac{1}{\sqrt{MN}} \sum_{m,n=1}^{M,N} g_{mn} e^{j[(2\pi(f_T^{(m)} + f_R^{(n)}) + \theta_{mn} + \theta_0)]} \tag{2.16}$$

where

$$g_{mn} = a_m b_n c_{mn}, \tag{2.17}$$

$$a_m = e^{j\pi(\delta_T/\lambda)\cos(\phi_T^{(m)} - \beta_T)}, \tag{2.18}$$

$$b_n = e^{j\pi(\delta_R/\lambda)\cos(\phi_R^{(n)} - \beta_R)}, \tag{2.19}$$

$$c_{mn} = e^{j\frac{2\pi}{\lambda}(R_T\cos\phi_T^{(m)} - R_R\cos\phi_R^{(n)})}, \tag{2.20}$$

$$f_T^{(m)} = f_{T_{\max}}\cos(\phi_T^{(m)} - \alpha_T), \tag{2.21}$$

$$f_R^{(n)} = f_{R_{\max}}\cos(\phi_R^{(n)} - \alpha_R), \tag{2.22}$$

and

$$\theta_0 = -\frac{2\pi}{\lambda}(R_T + D + R_R). \tag{2.23}$$

While the diffuse component $h_{22}(t)$ of the link from $A_T^{(2)}$ to $A_R^{(2)}$ can be obtained from (2.16) by replacing a_m and b_n by their respective complex conjugates a_m^* and b_n^*, the diffuse components $h_{12}(t)$ and $h_{21}(t)$ can directly be obtained from (2.7) by performing the substitutions $a_m \to a_m^*$, and $b_n \to b_n^*$, respectively. The stochastic channel matrix, $H(t)$, which describes completely the reference model of the above two-ring MIMO frequency nonselective Rayleigh fading channel can be derived by the combination of the four diffuse components $h_{ij}(t)(i,j = 1,2)$ of the $A_T^{(j)}$ to $A_R^{(i)}$

link, resulting in

$$H(t) = \begin{pmatrix} h_{11}(t) & h_{12}(t) \\ h_{21}(t) & h_{22}(t) \end{pmatrix}. \tag{2.24}$$

The Geometrical Double-Ring Model

One of the main disadvantages of the Geometrical two-ring model [22] is that the complex faded envelope depends on the distance between scatterers and antenna elements which is an unknown parameter in most simulation trials. The Geometrical Double-Ring Model discussed in this section is based on the "double-ring" geometrical model proposed in [23]. This model is for MIMO M2M Rayleigh fading channels [24], where the complex faded envelope is not dependent on the distance between scatterers and antenna elements.

General assumptions made on this model are:

1. A narrowband MIMO communication system with n_T transmit and n_R receive omnidirectional antenna elements

2. The radio propagation environment is characterized by two dimensional(2D) scattering with non line of sight (NLoS) conditions between the transmitter and the receiver.

3. MIMO channel can be described by an $n_R \times n_T$ matrix

$$H(t) = \left[h_{ij}(t)\right]_{n_R \times n_T}$$

   of complex faded envelopes.

4. The number of local scatterers around the transmitter and the receiver is infinite.

Fig. 2.3 shows a geometrical "double-ring" model for MIMO M2M channel with $n_T = n_R = 2$ antenna elements.

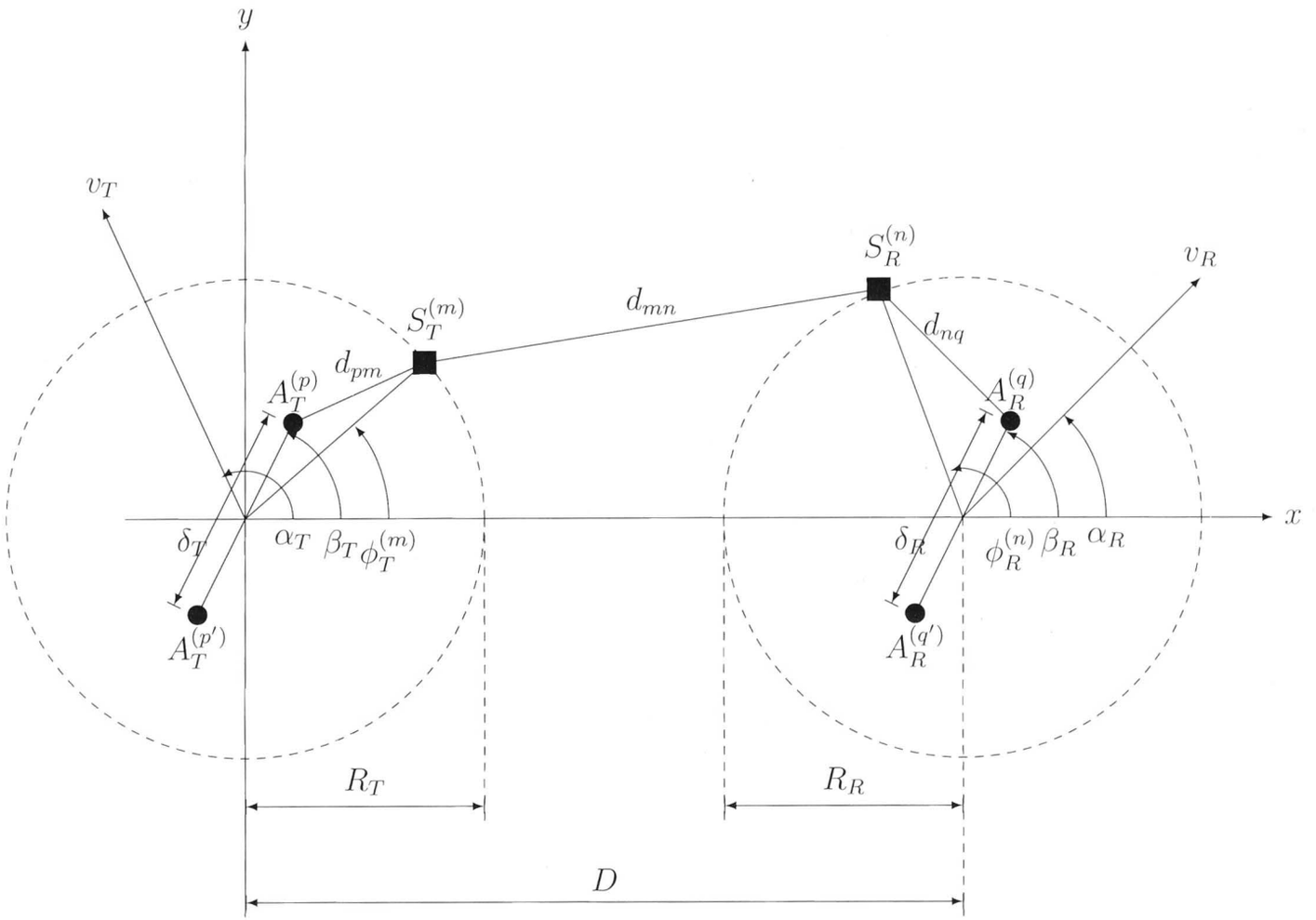

Figure 2.3: The geometrical "double-ring" model for a 2×2 MIMO channel with local scatterers around a mobile transmitter MS_T (left) and a mobile receiver MS_R (right).

The received complex faded envelope can be approximated by

$$h_{pq}(t) = \lim_{M,N\to\infty} \frac{1}{\sqrt{MN}} \sum_{m,n=1}^{M,N} e^{jk_0(d_{pm}+d_{mn}+d_{nq})+j2\pi(f_T^m+f_R^n)t+j\theta_{mn}}, \tag{2.25}$$

$$f_T^m = f_{T_{\max}} \cos(\phi_T^{(m)} - \alpha_T), \tag{2.26}$$

and

$$f_R^n = f_{R_{\max}} \cos(\phi_R^{(n)} - \alpha_R), \tag{2.27}$$

Finally, the symbols d_{pm}, d_{mn}, and d_{nq} denote distances $A_T^{(p)} - S_T^{(m)}$, $S_T^{(m)} - S_R^{(n)}$, and $S_R^{(n)} - A_R^{(q)}$, respectively, as shown in Fig. 2.3. It is assumed that $\phi_T^{(m)}$, $\phi_R^{(n)}$, and the phases ϕ_{mn} are mutually independent random variables, and that ϕ_{mn} are uniformly distributed on the interval $[-\pi, \pi)$.

Distances d_{pm},d_{mn}, and d_{nq} can be expressed as functions of random variables $\phi_T^{(m)}$ and $\phi_R^{(n)}$. From Fig. 2.3, assuming $\max \delta_T, \delta_R \ll \max R_T, R_R \ll D$ and invoking the law of cosines, these distances are

$$d_{pm} = R_T - 0.5\delta_T \cos(\phi_T^{(m)} - \beta_T), \tag{2.28}$$

$$d_{nq} = R_R - 0.5\delta_R \cos(\phi_R^{(n)} - \beta_R), \tag{2.29}$$

and

$$d_{mn} = D - R_T \cos\phi_T^{(m)} - R_R \sin(\pi - \phi_R^{(n)}) \approx D. \tag{2.30}$$

Equations (2.28) and (2.29) can be generalized for any number of transmit and receive antennas as follows:

$$d_{pm} = R_T - \delta_T(0.5n_T + 0.5 - p) \cos(\phi_T^{(m)} - \beta_T), \tag{2.31}$$

and

$$d_{nq} = R_R - \delta_R(0.5n_R + 0.5 - q) \cos(\phi_R^{(n)} - \beta_R), \tag{2.32}$$

where parameters p and q take values from the sets $p \in \{1, \ldots, n_T\}$ and $q \in \{1, \ldots, n_R\}$, respectively. Substituting (2.30), (2.31), (2.32) into (2.25), the com-

plex faded envelope of the link $A_T^{(p)} - A_R^{(q)}$ becomes

$$h_{pq}(t) = \lim_{M,N\to\infty} \frac{1}{\sqrt{MN}} \sum_{m,n=1}^{M,N} a_{p,m} b_{n,q} \exp\{j2\pi(f_T^m + f_R^n)t + j\theta_{mn} + j\theta_0\}, \quad (2.33)$$

where $\theta_0 = -(2\pi/\lambda)(R_T + D + R_R)$ and

$$a_{p,m} = \exp\{jk_0(0.5n_T + 0.5 - p)\delta_T \cos(\phi_T^{(m)} - \beta_T\}, \quad (2.34)$$

and

$$b_{n,q} = \exp\{jk_0(0.5n_R + 0.5 - q)\delta_R \cos(\phi_R^{(n)} - \beta_R)\}. \quad (2.35)$$

When we compare the Geometrical two-ring model [22] with the Geometrical Double-Ring Model [24], other than the assumption in (2.30), the rest are the same. Due to that assumption, [22] has an additional component in the transfer function, that is, $c_{mn} = e^{j\frac{2\pi}{\lambda}(R_T \cos\phi_T^{(m)} - R_R \cos\phi_R^{(n)})}$, needs R_T, R_R, which are unknown parameters in most simulation trials. Thus, [24] has better modeling aspects with regard to application.

The Geometrical Modified Two-Ring Model

In this model [25], we describe the modified geometrical two ring(MGTR) model for narrowband MIMO M2M channels. MGTR is based on the extension of single-bounce two ring (SBTR) model [26]. The geometry of modified two-ring model is shown in Fig. 2.4

General assumptions made on this model are:

1. A narrowband MIMO communication system radio propagation environment is characterized by 2D scattering with NLoS conditions between the transmitter and the receiver.

2. The MIMO channel is described by an $n_R \times n_T$ matrix and for simplicity use $n_T = n_R = 2$ antenna elements, where local scatterers of MS_T and MS_R are modeled to be distributed on two separate rings.

3. Only single-bounce rays are considered and multiple bounces are treated as secondary effects which avoids the problem of double-bounce two-ring model.

4. Radii R_T and R_R are small in comparison with D which is the distance between the transmitter and the receiver, i.e.,

$$\max\{R_T, R_R\} \ll D.$$

5. Finally,

$$\min\{R_T, R_R\} \gg \max\{\delta_T, \delta_R\}.$$

The positive random variables g_T^m and g_R^n represent the amplitudes of the wave scattered by S_T^m and S_R^n, which also include the antenna gains at φ_T^m and ϕ_R^n. Ψ_T^m and Ψ_R^n are the associated phase shifts.

The symbols ϕ_T and ϕ_R denote the main AoD and the main AoA, respectively and the symbols φ_T and φ_R denote the auxiliary AoD and the auxiliary AoA, respectively. Furthermore, 2Δ is the maximum angle spread at MS_T, determined by the scattering around MS_R. Similarly $2\Delta'$ is the maximum angle spread at MS_R, determined by the scattering around MS_T.

$$h_{lp}(t) = \sqrt{\frac{\eta_T \Omega_{lp}}{N_T}} \sum_{k=1}^{N_T} g_T^k \exp\{-j\frac{2\pi}{\lambda}(d_{A_T^p S_T^k} + d_{S_T^k A_R^l}) + j\Psi_T^k + j2\pi f_1^k t\}$$
$$+ \sqrt{\frac{\eta_R \Omega_{lp}}{N_R}} \sum_{k=1}^{N_R} g_R^i \exp\{-j\frac{2\pi}{\lambda}(d_{A_T^p S_R^i} + d_{S_R^i A_R^l}) + j\Psi_R^i + j2\pi f_2^i t\} \quad (2.36)$$

where the first and the second summations correspond to the MS_T and MS_R rings, respectively.

Frequencies f_1^k and f_2^i are given by

$$f_1^k = f_{T_{\max}} \cos(\alpha_T - \varphi_T^k) + f_{R_{\max}} \cos(\alpha_R - \phi_T^k), \quad (2.37)$$

and

$$f_2^i = f_{T_{\max}} \cos(\alpha_T - \varphi_R^i) + f_{R_{\max}} \cos(\alpha_R - \phi_R^i). \quad (2.38)$$

The Geometrical Two-Erose-Ring Model

In [27] the authors proposed a geometrical Two-Erose-Ring model for the narrowband MIMO M2M channel. In this model it is assumed that direct LoS is not

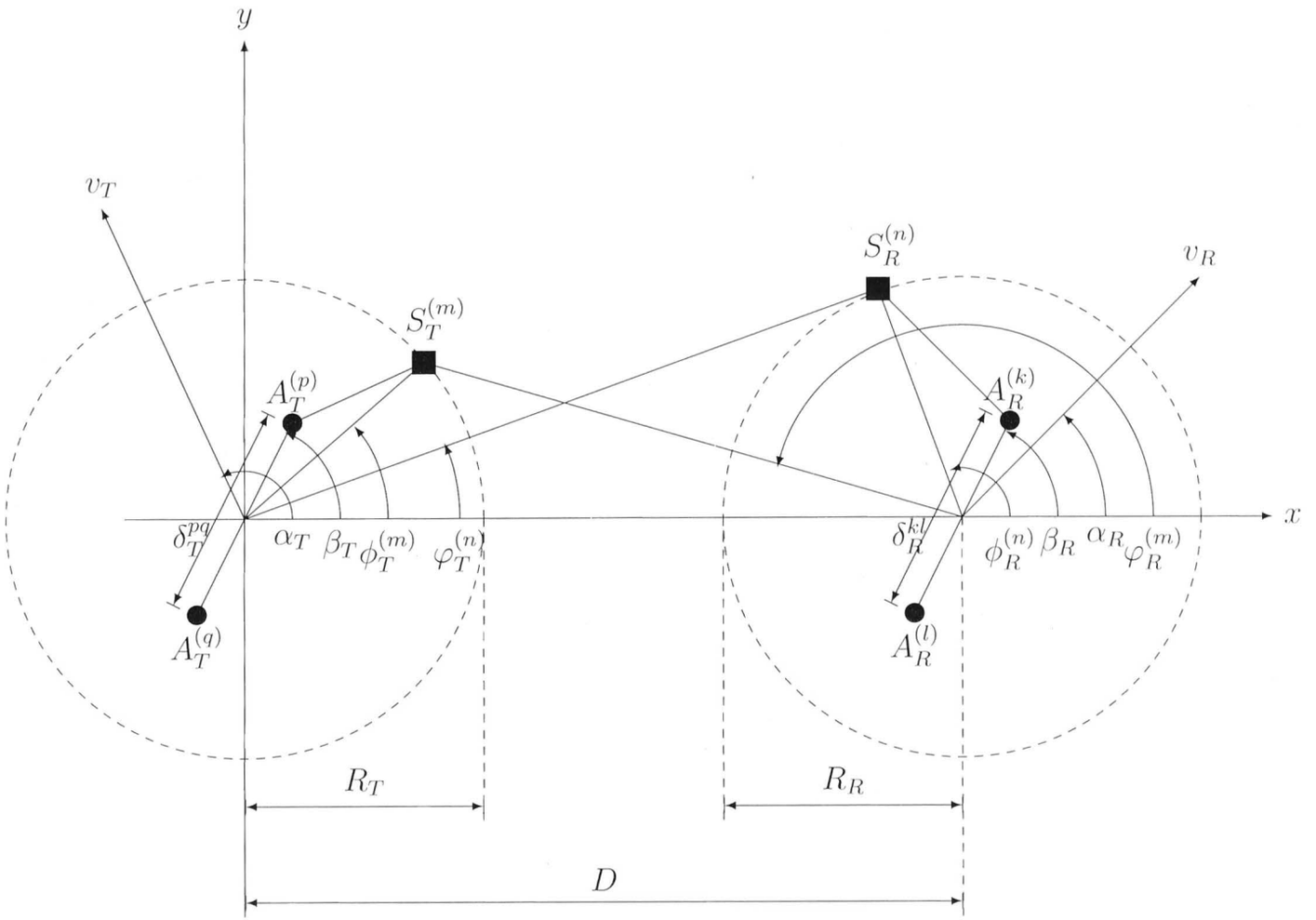

Figure 2.4: The modified geometrical two-ring model for a 2×2 MIMO channel with scatterers around mobile transmitter MS_T (left) and a mobile receiver MS_R (right).

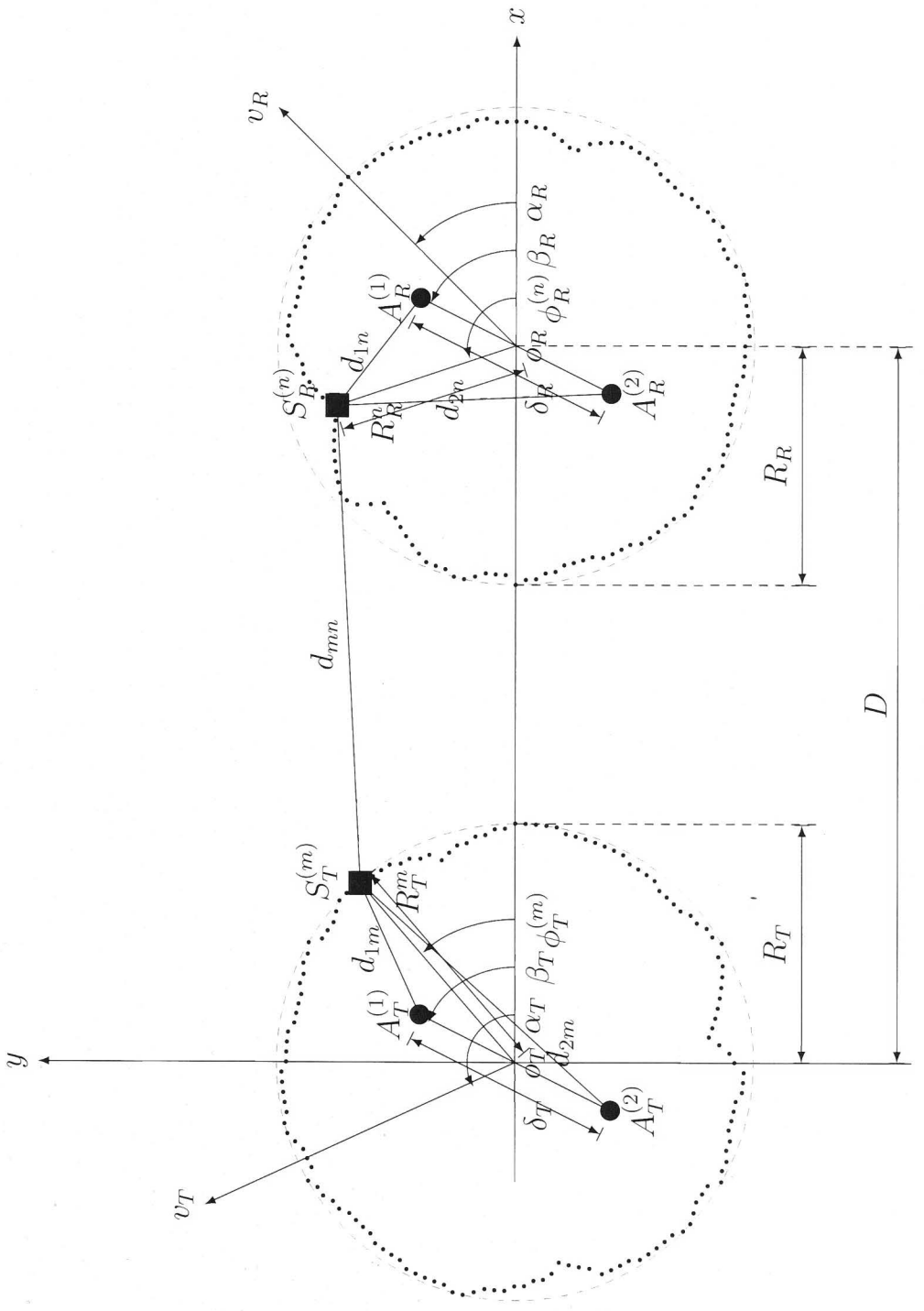

Figure 2.5: The geometrical two-erose-ring model

available. The Two-Erose-Ring model is shown in Fig. 2.5, where two transmit antennas and two receive antennas are surrounded by scatterers as two-erose-rings. The distance of local scatterers around the transmitter and, the receiver from origins are denoted as R_T^m and R_R^n respectively, and are defined by

$$R_T^m = R_T \cos \omega_T^m \tag{2.39}$$

and

$$R_R^n = R_R \cos \omega_R^n, \tag{2.40}$$

where $R_T = \max\{R_T^m\}$ and $R_R = \max\{R_R^n\}$ denote the ring radii of transmitter and receiver, respectively, while ω_T^m and ω_R^n are normal distributed random variables over interval $(-\pi/2, \pi/2)$. This geometrical two-erose-ring model is much closer to the reality than the two-ring model for distances between scatterers and transmitter (receiver) are not fixed but random variables depending on $\omega_T^m(\omega_R^n)$.

General assumptions made on this model are:

1. In this model, due to high path loss the contributions of remote scatterers to the total received power can be neglected. Hence only local scattering is considered.

2. The radii R_T and R_R are small in comparison with D, i.e.,

$$\max\{R_T, R_R\} \ll D.$$

3. As the antenna spacing δ_T and δ_R are generally small in comparison with R_T^m and R_R^n, i.e.,

$$\max\{\delta_T, \delta_R\} \ll \min\{R_T^m, R_R^n\}.$$

4. The number of local scatterers around the transmitter and the receiver are infinite. Such propagation conditions generally occur between outdoor mobile units in urban areas.

The time-space received faded envelope can be written as:

$$h_{11}(\overrightarrow{r_R}) = \lim_{M,N\to\infty} \sum_{m,n=1}^{M,N} E_{mn} e^{-j(KD_{mn} + \overrightarrow{k}_R^n \cdot \overrightarrow{r}_R - \overrightarrow{k}_T^m \cdot \overrightarrow{r}_T - \theta_{mn})}, \tag{2.41}$$

where E_{mn} and θ_{mn} denote the joint gain and joint phase shift caused by the interaction of the scatterers $S_T^{(m)}$ and $S_R^{(n)}$, respectively. It is shown in [22] that the joint gain, E_{mn} and joint phase shift, θ_{mn} can be expressed as:

$$E_{mn} = E_m \cdot E_n = 1/\sqrt{MN}, \tag{2.42}$$

and

$$\theta_{mn} = (\theta_m + \theta_n) \mod 2\pi, \tag{2.43}$$

where θ_{mn} is uniformly distributed over $[0, 2\pi)$. As D_{mn} is the length of the total distance which a plane wave travels from A_T^1 to A_R^1 via the scatterers $S_T^{(m)}$ and $S_R^{(n)}$, it can be written as:

$$D_{mn} = d_{1m} + d_{mn} + d_{1n}, \tag{2.44}$$

where d_{1m}, d_{mn} and d_{1n} are illustrated in Fig. 2.5 and can be expressed as functions of random variables ω_T^m, ω_R^n, ϕ_T^m and ϕ_R^n.

The signal received from a scatterer to two receive antennas under this model is shown in Fig. 2.6. Assuming

$$\max\{\delta_T, \delta_R\} \ll \min\{R_T^m, R_R^n\} \leq \max\{R_T, R_R\}$$

and invoking the law of cosines, these distances are

$$d_{1m}(t) \approx R_T \cos\omega_T^m - 0.5\delta_T \cos(\phi_T^m - \beta_T) \tag{2.45}$$

$$d_{mn}(t) \approx D + R_R \cos\omega_R^n \cos\phi_R^n - R_T \cos\omega_T^m \cos\phi_T^m \tag{2.46}$$

and

$$d_{1n}(t) \approx R_R \cos\omega_R^n - 0.5\delta_R \cos(\phi_R^n - \beta_R). \tag{2.47}$$

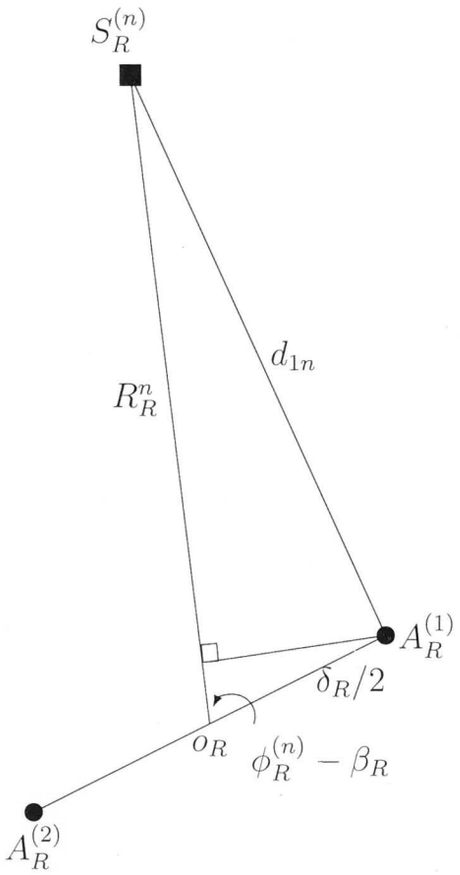

Figure 2.6: Signal received at two antennas from the scatter in geometrical two-erose-ring model

In (2.41) $\overrightarrow{k}_T^m$ is the wave vector pointing in the propagation direction of the m th transmitted plane wave, and $\overrightarrow{r}_T$ denotes the spatial translation vector of the transmitter. With a similar definition for $\overrightarrow{k}_R^n$ and $\overrightarrow{r}_R$, the phase changes $\overrightarrow{k}_T^m \cdot \overrightarrow{r}_T$ and $\overrightarrow{k}_R^n \cdot \overrightarrow{r}_R$ can be expressed as:

$$\overrightarrow{k}_T^m \cdot \overrightarrow{r}_T = 2\pi f_{T_{\max}} \cos(\phi_T^m - \alpha_T)t \tag{2.48}$$

and

$$\overrightarrow{k}_R^n \cdot \overrightarrow{r}_R = 2\pi f_{R_{\max}} \cos(\phi_R^n - \alpha_R)t. \tag{2.49}$$

Substituting (2.42)–(2.47) into (2.41) the complex faded envelope of the link A_T^1 to A_R^1 becomes

$$h_{11}(t) = \lim_{M,N\to\infty} \frac{1}{\sqrt{MN}} \sum_{m,n=1}^{M,N} a_m b_n c_{mn} e^{j2\pi(f_T^m + f_R^n)t + j\theta_{mn} - j\theta_0} \tag{2.50}$$

where

$$a_m = e^{jk_0(\delta_T/2)\cos(\phi_T^m - \beta_T)}, \tag{2.51}$$

$$b_n = e^{jk_0(\delta_R/2)\cos(\phi_R^n - \beta_R)}, \tag{2.52}$$

$$c_{mn} = e^{jk_0(R_T \cos\omega_T^m \cos\phi_T^m - R_R \cos\omega_R^n \cos\phi_R^n)}, \tag{2.53}$$

$$f_T^m = f_{T_{\max}} \cos(\phi_T^m - \alpha_T), \tag{2.54}$$

$$f_R^n = f_{R_{\max}} \cos(\phi_R^n - \alpha_R), \tag{2.55}$$

and

$$\theta_0 = k_0(R_T \cos\omega_T^m + D + R_R \cos\omega_R^n). \tag{2.56}$$

Extending the above 2×2 antennas M2M reference channel model based on geometrical two-erose-ring model to $n_T \times n_R$ MIMO M2M reference model where $n_T, n_R \geq 2$, the diffuse component of the link from the transmit antenna element A_T^i $(i = 1, 2, \ldots, n_T)$ to the receive antenna element A_R^j $(j = 1, 2, \ldots, n_R)$ can be

written as:

$$h_{pq}(t) = \lim_{M,N\to\infty} \frac{1}{\sqrt{MN}} \sum_{m,n=1}^{M,N} a_m b_n c_{mn} e^{j2\pi(f_T^m + f_R^n)t + j\theta_{mn} - j\theta_0}, \tag{2.57}$$

where

$$a_m = e^{j((n_T+1)/2-p)k_0\delta_T \cos(\phi_T^m - \beta_T)}, \tag{2.58}$$

$$b_n = e^{j((n_R+1)/2-q)k_0\delta_R \cos(\phi_R^n - \beta_R)}, \tag{2.59}$$

$$c_{mn} = e^{jk_0(R_T \cos\omega_T^m \cos\phi_T^m - R_R \cos\omega_R^n \cos\phi_R^n)}, \tag{2.60}$$

$$f_T^m = f_{T_{\max}} \cos(\phi_T^m - \alpha_T), \tag{2.61}$$

$$f_R^n = f_{R_{\max}} \cos(\phi_R^n - \alpha_R), \tag{2.62}$$

and

$$\theta_0 = k_0(R_T \cos\omega_T^m + D + R_R \cos\omega_R^n). \tag{2.63}$$

The Combination of a Two Ring and an Ellipse Model

This model is a combination of a single- and a double-bounce two-ring model, a single-bounce ellipse model, and the LoS component [13]. The geometry of this model is shown in Fig. 2.7 where both n_T and n_R are equipped with omnidirectional low elevation antennas. As an example, uniform linear antenna arrays with $n_T = n_R = 2$ are used here.

In Fig. 2.7, $S^{(n_1)}$ represents the n_1th ($n_1 = 1, \ldots, N_1$) effective scatterer lying on a ring of radius R_T. Similar notation applies to $S^{(n_2)}$ and $S^{(n_3)}$. In the case of $S^{(n_3)}$, N_3 effective scatterers lie on an ellipse with the Tx and Rx located at the foci. When f denotes the half length of the distance between the two focal points of the ellipse, the distance between the Tx and Rx is given by $D = 2f$.

General assumptions made on this model are:

1. In this model, it is normally assumed that R_T and R_R and the difference between the semi-major axis a and the parameter f, are all much greater

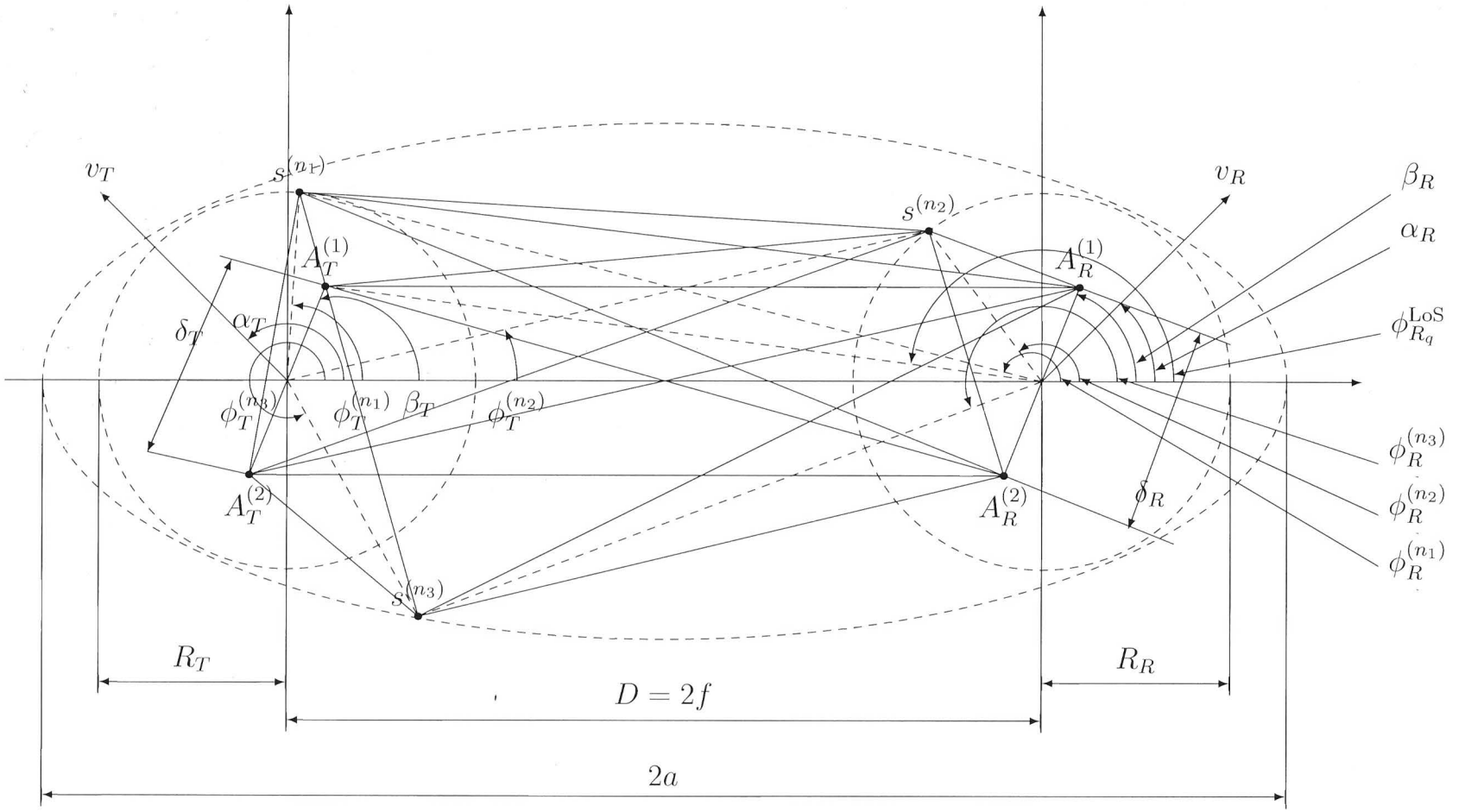

Figure 2.7: A generic channel model combining a two-ring model and an ellipse model with LoS components, single- and double-bounced rays for a MIMO M2M channel.

than the antenna element spacings δ_T and δ_R, i.e., $\min\{R_T, R_R, a-f\} \gg \max\{\delta_T, \delta_R\}$.

The AoA of the wave traveling from an effective scatterer $S^{(n_i)}$ $(i \in \{1,2,3\})$ toward the Rx is denoted by $\phi_R^{(n_i)}$. The AoD of the wave that impinges on the effective scatterer $S^{(n_i)}$ is designated by $\phi_T^{(n_i)}$. Note that $\phi_{R_q}^{\text{LoS}}$ denotes the AoA of a LoS path.

The MIMO fading channel can be described by a matrix $H(t) = [h_{pq}(t)]_{n_R \times n_T}$ of size $n_R \times n_T$. The received complex fading envelope between the pth $(p = 1, \ldots, n_T)$ Tx and the qth $(q = 1, \ldots, n_R)$ Rx at the carrier frequency f_c is a superposition of the LoS, single-, and double-bounced components, and can be expressed as:

$$h_{pq}(t) = h_{pq}^{\text{LoS}}(t) + h_{pq}^{\text{SB}}(t) + h_{pq}^{\text{DB}}(t), \tag{2.64}$$

where

$$\begin{aligned} h_{pq}^{\text{LoS}}(t) = & \sqrt{\frac{K_{pq}\Omega_{pq}}{K_{pq}+1}} e^{-j2\pi f_c \tau_{pq}} \\ & \times e^{j[2\pi f_{T\max} t \cos(\pi - \phi_{R_q}^{\text{LoS}} + \gamma_T) + 2\pi f_{R\max} t \cos(\phi_{R_q}^{\text{LoS}} - \gamma_R)]} \end{aligned} \tag{2.65}$$

$$\begin{aligned} h_{pq}^{\text{SB}}(t) = & \sum_{i=1}^{I} \sqrt{\frac{\eta_{SB_i}\Omega_{pq}}{K_{pq}+1}} \lim_{N_i \to \infty} \sum_{n_i=1}^{N_i} \frac{1}{\sqrt{N_i}} e^{j(\psi_{n_i} - 2\pi f_c \tau_{pq,n_i})} \\ & \times e^{j[2\pi f_{T\max} t \cos(\phi_T^{(n_i)} - \gamma_T) + 2\pi f_{R\max} t \cos(\phi_R^{(n_i)} - \gamma_R)]} \end{aligned} \tag{2.66}$$

and

$$\begin{aligned} h_{pq}^{\text{DB}}(t) = & \sqrt{\frac{\eta_{DB}\Omega_{pq}}{K_{pq}+1}} \lim_{N_1, N_2 \to \infty} \sum_{n_1, n_2 = 1}^{N_1, N_2} \frac{1}{\sqrt{N_1 N_2}} e^{j(\psi_{n_1,n_2} - 2\pi f_c \tau_{pq,n_1,n_2})} \\ & \times e^{j[2\pi f_{T\max} t \cos(\phi_T^{(n_1)} - \gamma_T) + 2\pi f_{R\max} t \cos(\phi_R^{(n_2)} - \gamma_R)]}. \end{aligned} \tag{2.67}$$

The Combination of a Two Ring and a Multiple Confocal Ellipses Model

While the combination of a two ring and an ellipse model given above shows a narrowband single user MIMO M2M multicarrier communication system, the combination of a two ring and a multiple confocal ellipses model given in this section considers a wideband MIMO M2M communication system [28]. Fig. 2.8

illustrates the geometry of the model considering both single- and double-bounced rays, as well as the LoS components.

Similar to the notation applied in the above section, $s^{(n_{1,1})}$ represents the $n_{1,1}^{th}$ ($n_{1,1} = 1, \ldots, N_{1,1}$) effective scatterer and this model has $N_{l,3}$ effective scatterers on the l^{th} ellipse, i.e., the l^{th} tap, where $l = 1, 2, \ldots, L$ with L being the total number of ellipses or taps.

In Fig. 2.8, $\phi_R^{(n1,1)}$, $\phi_R^{(n1,2)}$, and $\phi_R^{(n1,3)}$ represent the AoA of the wave traveling from an effective scatterer $s^{(n_{1,1})}$, $s^{(n_{1,2})}$, and $s^{(n_{l,3})}$ toward the Rx, respectively. Similarly, $\phi_T^{(n1,1)}$, $\phi_T^{(n1,2)}$, and $\phi_T^{(n1,3)}$ denote the AoD of the wave that arrives on the effective scatterers $s^{(n_{1,1})}$, $s^{(n_{1,2})}$, and $s^{(n_{l,3})}$, respectively, while ϕ^{LoS} denotes the AoA of a LoS path.

The MIMO fading channel for this model is given by $H(t) = [h_{pq}(t, \tau')]_{n_R \times n_T}$, where according to the tap delay line (TDL) concept, the complex impulse response between the p^{th} ($p = 1, \ldots, n_T$) Tx, T_p, and the q^{th} ($q = 1, \ldots, n_R$) Rx, R_q, can be expressed as:

$$h_{pq}(t, \tau') = \sum_{l=1}^{L} c_l h_{l,pq}(t) \delta(\tau' - \tau_l'). \tag{2.68}$$

The gain of the l^{th} tap is given by c_l while $h_{l,pq}(t)$ and τ_l' denote the complex time-variant tap coefficient and the discrete propagation delay of the l^{th} tap, respectively.

From the above GBSPM, the complex tap coefficient for the first tap of the $T_p - R_q$ link is a superposition of the LoS component, single and double-bounced components, and can be expressed as:

$$h_{l,pq}(t) = h_{l,pq}^{\mathrm{LoS}}(t) + \sum_{i=1}^{L} h_{l,pq}^{\mathrm{SB}_i}(t) + h_{l,pq}^{\mathrm{DB}}(t). \tag{2.69}$$

The Geometrical Single Bounce Two Sphere (SBTS) Model

When comparing with other M2M models, the main difference in this model is that only single-bounce rays are considered and multiple bounces are treated as secondary effects [29]. This avoids the problem of double-bounce two ring model.

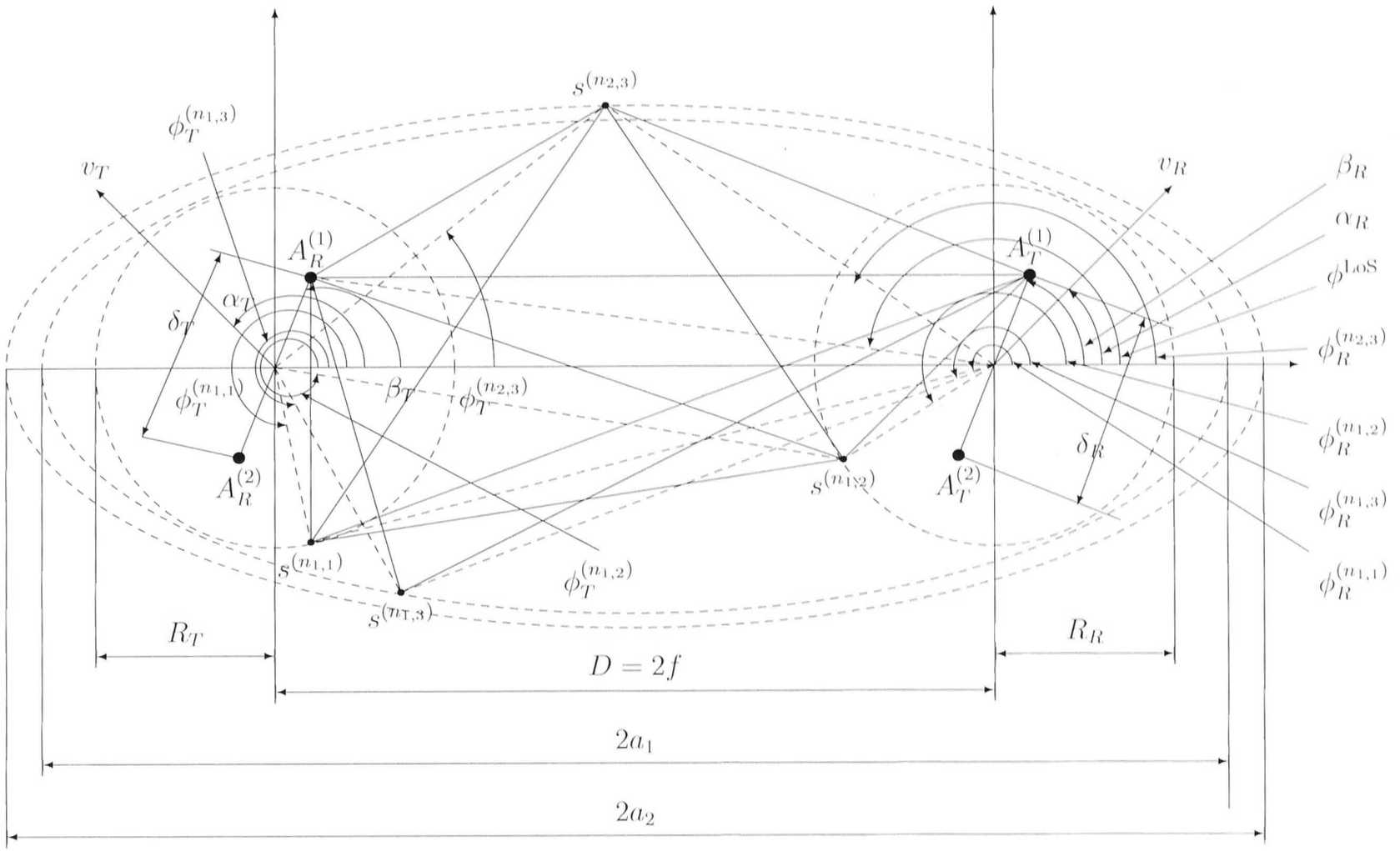

Figure 2.8: The combination of a two ring and a multiple confocal ellipses model.

The geometry of this model is given in Fig. 2.9 where the additional notations related to three dimensional(3D) GBSPM models represent in the Table 2.2.

The general assumptions made on this model are:

1. Radii R_T and R_R are small in comparison with D, i.e.,

$$\max\{R_T, R_R\} \ll D.$$

2. The antenna spacing are generally small in comparison with the radii R_T and R_R, i.e.,

$$\min\{R_T, R_R\} \gg \max\{\delta_T, \delta_R\}.$$

The channel gain $h_{lp}(t)$ between the antenna elements A_T^p and A_R^l is given by

$$h_{lp}(t) = \sqrt{\frac{\eta_T}{n_T}} \sum_{m=1}^{n_T} \exp\{-j\frac{2\pi}{\lambda}(d_{A_T^p S_T^m} + d_{S_T^m A_R^l}) + j\Psi_T^m + j2\pi f_1^m t\}$$
$$+ \sqrt{\frac{\eta_R}{n_R}} \sum_{n=1}^{n_R} \exp\{-j\frac{2\pi}{\lambda}(d_{A_T^p S_R^n} + d_{S_R^n A_R^l}) + j\Psi_R^n + j2\pi f_2^n t\}. \quad (2.70)$$

As the MS_R receives single-bounce rays from both the scatterer $S_R^{(n)}$ around the MS_R and the scatterer $S_T^{(m)}$ around the MS_T, (2.70) has two summations corresponding to MS_T and MS_R spheres. In (2.70) Ψ_T^m andΨ_R^n are the associated phase shifts while frequencies f_1^m and f_2^n are given by

$$f_1^m = f_{T_{\max}} \cos(\alpha_T - \varphi_T^m) \cos(\theta_T^m) + f_{R_{\max}} \cos(\alpha_R - \phi_T^m) \cos(\theta_R'^m), \quad (2.71)$$

and

$$f_2^n = f_{T_{\max}} \cos(\alpha_T - \varphi_R^n) \cos(\theta_T^n) + f_{R_{\max}} \cos(\alpha_R - \phi_R^n) \cos(\theta_R'^n), \quad (2.72)$$

where it is assumed that $\{\Psi_T^k\}_{k=1}^{N_T}$ and $\{\Psi_R^i\}_{i=1}^{N_R}$ are mutually independent and identically distributed (i.i.d.) random variables with uniform distributions over $[0, 2\pi)$.

Parameter description	Symbol
Main azimuth angle of departure (AAoD)	φ_T
Main elevation angle of departure (EAoD)	θ_T
Main azimuth angle of Arrival (AAoA)	φ_R
Main elevation angle of arrival (EAoA)	θ_R
Auxiliary AAoD	φ'_T
Auxiliary EAoD	θ'_T
Auxiliary AAoA	φ'_R
Auxiliary EAoD	θ'_R
The azimuth angle of the Txs antenna array relative to the x-y plane	β_T^A
The azimuth angle of the Rxs antenna array relative to the x-y plane	β_R^A
The elevation angle of the Txs antenna array relative to the x-y plane	β_T^E
The elevation angle of the Rxs antenna array relative to the x-y plane	β_R^E
Maximum angle spread at MS_T, determined by the 3D scattering around MS_R in both azimuth and elevation direction.	$2\Delta = \arcsin(R_T/D)$
Maximum angle spread at MS_R, determined by the 3D scattering around MS_T in both azimuth and elevation direction.	$2\Delta' = \arcsin(R_R/D)$

Table 2.2: Parameters used in 3D Geometry-Based Stochastic Physical Models

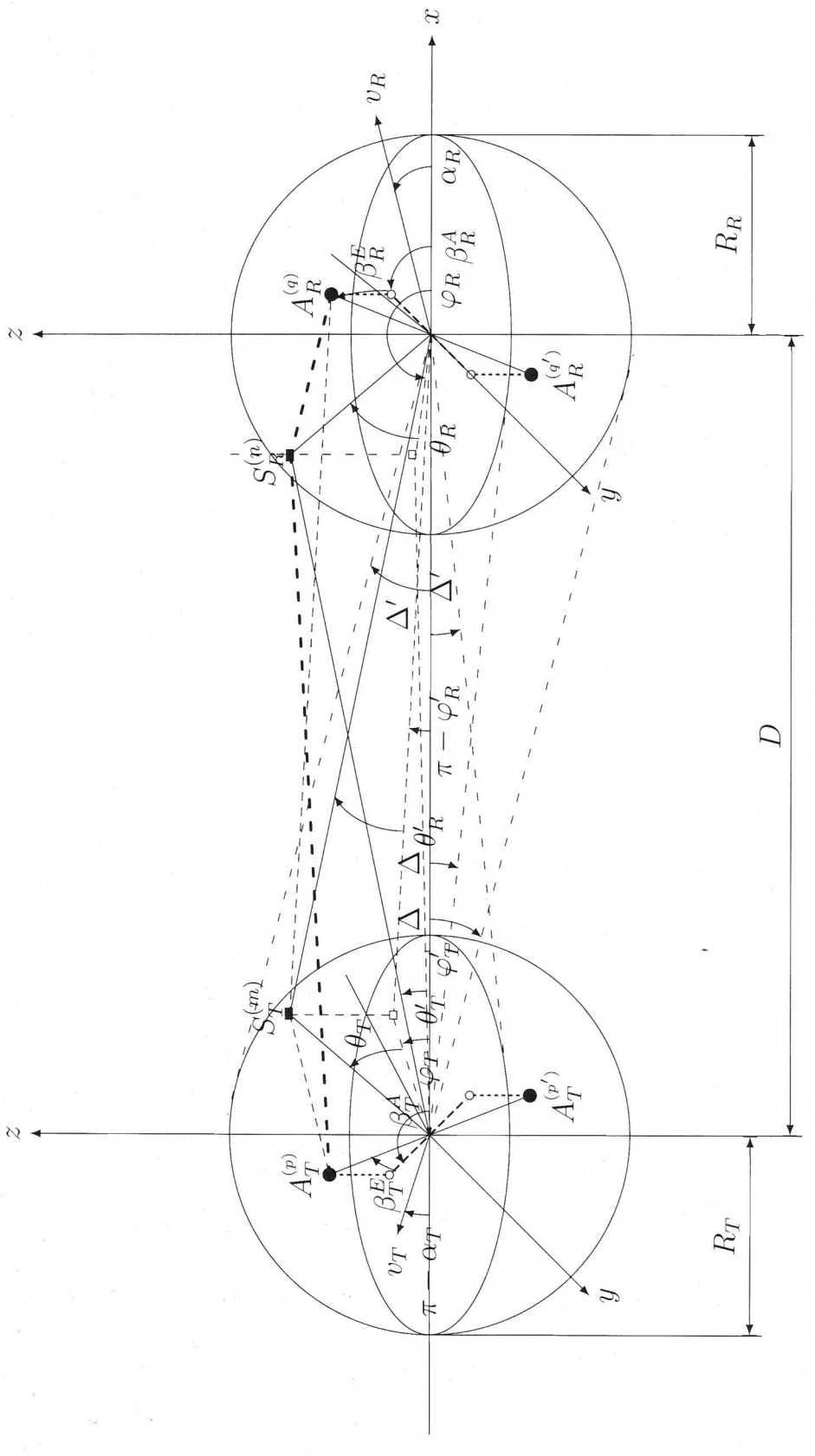

Figure 2.9: The SBTS model for a 2×2 MIMO channel with 3D distribution of scatterers around mobile transmitter MS_T (left) and mobile receiver MS_R (right).

The Geometric Street Scattering Model

The Geometric Street Scattering Model shown in Fig. 2.10 is based on the single-bounce street model [30].

The general assumptions made on this model are:

1. The transmitter antenna dimensions are small compared to the following quantity: $\min\{h_{T1}, h_{T2}\}$.

2. The receiver antenna dimensions are small compared to the following quantity: $\min\{h_{R1}, h_{R2}\}$.

3. As the number of scatterers is infinite, the diffuse component as seen from the receiver side is composed of an infinite number of homogeneous plane waves.

4. The phase shifts θ_n introduced by the scatterer $S^{(n)}$ are i.i.d. random variables, each having a uniform distribution over the interval $[0, 2\pi)$.

With the above assumptions, it can be shown that $(n_T - 1)\delta_T \ll \min\{h_{T1}, h_{T2}\}$ and $(n_R - 1)\delta_R \ll \min\{h_{R1}, h_{R2}\}$.

The channel gain for the link between the l^{th} transmit antenna element $A_T^{(l)}$ and the k^{th} receive antenna element $A_R^{(k)}$ is given by

$$g_{kl}(\overrightarrow{r_T}, \overrightarrow{r_R}) = \lim_{N\to\infty} \sum_{n=1}^{N} c_n e^{j(\theta_n + \overrightarrow{k}_T^{(n)} \cdot \overrightarrow{r}_T - \overrightarrow{k}_R^{(n)} \cdot \overrightarrow{r}_R - k_0 D_n)}, \tag{2.73}$$

where c_n denotes the gain introduced by the scatterer $S^{(n)}$. With the assumptions given above, the waves emerging from different transmit antenna elements arrive at a particular scatterer $S^{(n)}$ at approximately the same angle while the waves emerging from a particular scatterer $S^{(n)}$ arrive at different receive antenna elements at approximately the same angle. Then the gain c_n is assumed to be constant and given by

$$c_n = \sqrt{\frac{2\sigma_0^2}{N}}, \tag{2.74}$$

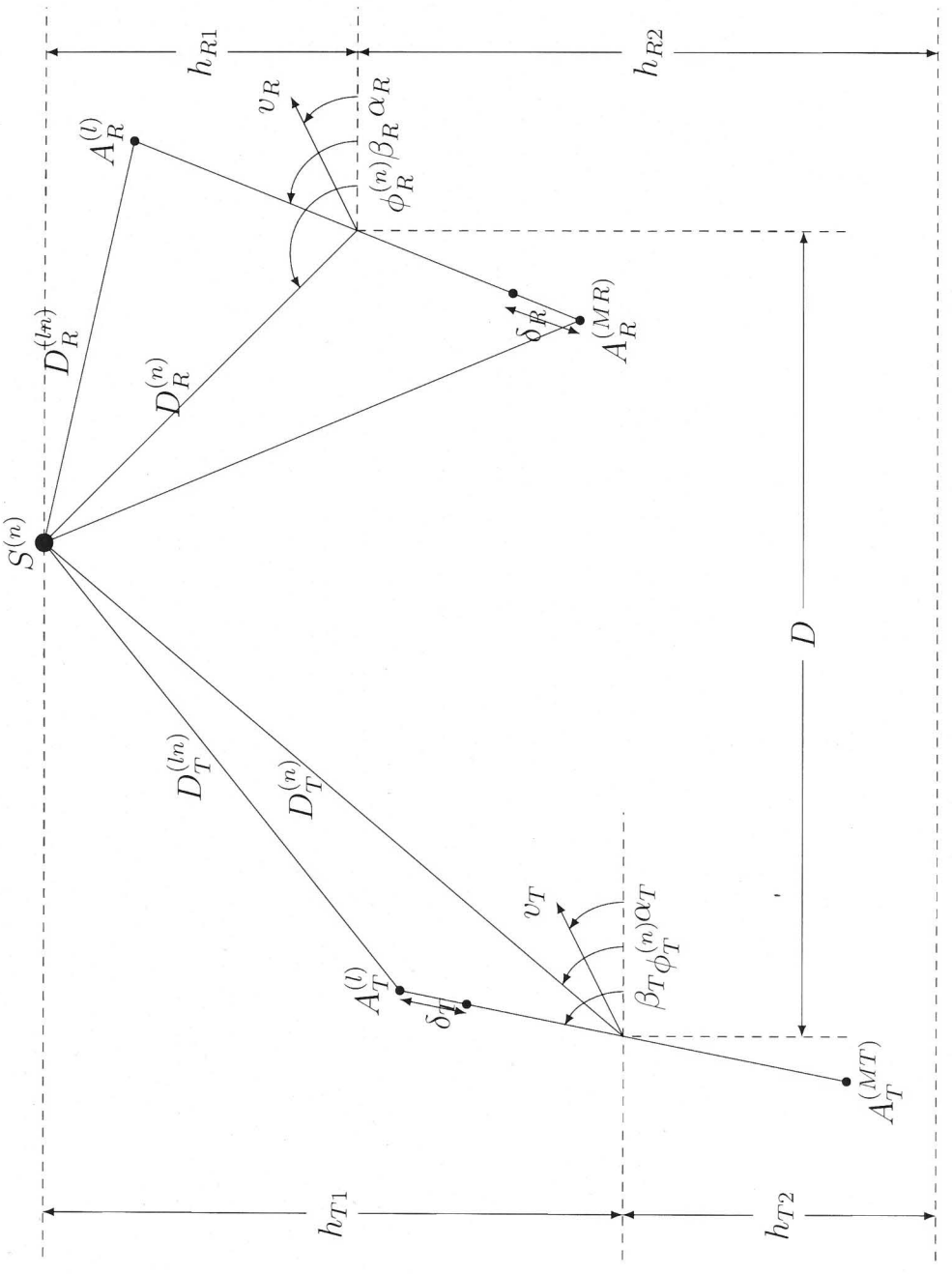

Figure 2.10: Geometric street scattering model for an $n_T \times n_R$ MIMO channel.

where σ_0 is the mean power of the received scattered components.

In (2.73), $\overrightarrow{k}_T^{(n)} \cdot \overrightarrow{r}_T$ expresses the influence of the transmitter movement on the channel gain and is given by

$$\overrightarrow{k}_T^{(n)} \cdot \overrightarrow{r}_T = 2\pi f_{T_{\max}} \cos(\phi_T^{(n)} - \alpha_T)t, \tag{2.75}$$

while $\overrightarrow{k}_R^{(n)} \cdot \overrightarrow{r}_R$ expresses the influence of the receiver movement on the channel gain and is given by

$$\overrightarrow{k}_R^{(n)} \cdot \overrightarrow{r}_R = 2\pi f_{R_{\max}} \cos(\phi_R^{(n)} - \alpha_R)t. \tag{2.76}$$

The term $k_0 D_n$ in (2.73) is due to the total traveled distance and is given by

$$k_0 D_n = \frac{2\pi}{\lambda}(D_T^{(l,n)} + D_R^{(n,k)}), \tag{2.77}$$

where $D_T^{(l,n)}$ and $D_R^{(n,k)}$ denote the distance from the l^{th} transmit antenna element A_T^l to the scatter $S^{(n)}$ and the distance between the scatterer $S^{(n)}$ to the k^{th} receive antenna element A_R^k, respectively.

Using the assumptions given above and $\sqrt{1+x} \approx 1 + x/2$ $(x \ll 1)$, $D_T^{(l,n)}$ can further be simplified as

$$D_T^{(l,n)} \approx D_T^{(n)} - (n_T - 2l + 1)\frac{\delta_T}{2}\cos(\phi_T^{(n)} - \beta_T). \tag{2.78}$$

Similarly,

$$D_R^{(n,k)} \approx D_R^{(n)} - (n_R - 2k + 1)\frac{\delta_R}{2}\cos(\phi_R^{(n)} - \beta_R), \tag{2.79}$$

where $D_T^{(n)} = h_{T1}/\sin(\phi_T^{(n)})$ and $D_R^{(n)} = h_{R1}/\sin(\phi_R^{(n)})$.

After substituting (2.74), (2.75), (2.76) in (2.73) and using the approximations in (2.77) and (2.78), the complex channel gain in (2.73) can be given as

$$g_{kl}(t) = \lim_{N\to\infty} \sqrt{\frac{2\sigma_0^2}{N}} \sum_{n=1}^{N} d_n a_{ln} b_{kn} e^{j(2\pi(f_T^{(n)} + f_R^{(n)})t + \theta_n)}, \tag{2.80}$$

where

$$d_n = e^{-j\frac{2\pi}{\lambda}\left(\frac{h_{T1}}{\sin(\phi_T^{(n)})}+\frac{h_{R1}}{\sin(\phi_R^{(n)})}\right)}, \tag{2.81}$$

$$a_{ln} = e^{j\pi\frac{\delta_T}{\lambda}(n_T-2l+1)\cos(\phi_T^{(n)}-\beta_T)}, \tag{2.82}$$

$$b_{kn} = e^{j\pi\frac{\delta_R}{\lambda}(n_R-2k+1)\cos(\phi_R^{(n)}-\beta_R)}, \tag{2.83}$$

$$f_T^{(n)} = f_{T_{\max}}\cos(\phi_T^{(n)} - \alpha_T), \tag{2.84}$$

and

$$f_R^{(n)} = f_{R_{\max}}\cos(\phi_R^{(n)} - \alpha_R). \tag{2.85}$$

By combining all the diffuse components $g_{kl}(t)$ $(k = 1, \ldots, n_R; l = 1, \ldots, n_T)$ of the $A_T^{(l)} - A_R^{(k)}$ link, we obtain the channel matrix $G(t) = [g_{kl}(t)]$, which describes completely the reference model of the proposed M2M MIMO frequency non selective rayleigh fading channel.

A Geometrical Two Cylinder Model

The Geometrical Two-Cylinder Model [31] is an extension of the one-cylinder model for F2M channels proposed in [32], [33]. The two-cylinder model for a MIMO M2M channel with $n_T = n_R = 2$ antenna elements is shown in Fig. 2.11. In this model, a cylinder of radius R_T is defined around the transmitter and M fixed omnidirectional scatterers lie on the surface of the cylinder where the m^{th} transmit scatterer is denoted by $S_T^{(m)}$. Similarly, N fixed omnidirectional scatterers lie on a surface of a cylinder of radius R_R around the receiver, and the n^{th} receive scatterer is denoted by $S_R^{(n)}$.

The general assumptions made on this model are:

1. The radii R_T and R_R are much smaller than the distance D, i.e.,

$$\max\{R_T, R_R\} \ll D.$$

2. When the spacing between antenna elements at the Tx and Rx is denoted by δ_T and δ_R, respectively, δ_T and δ_R are much smaller than the radii R_T

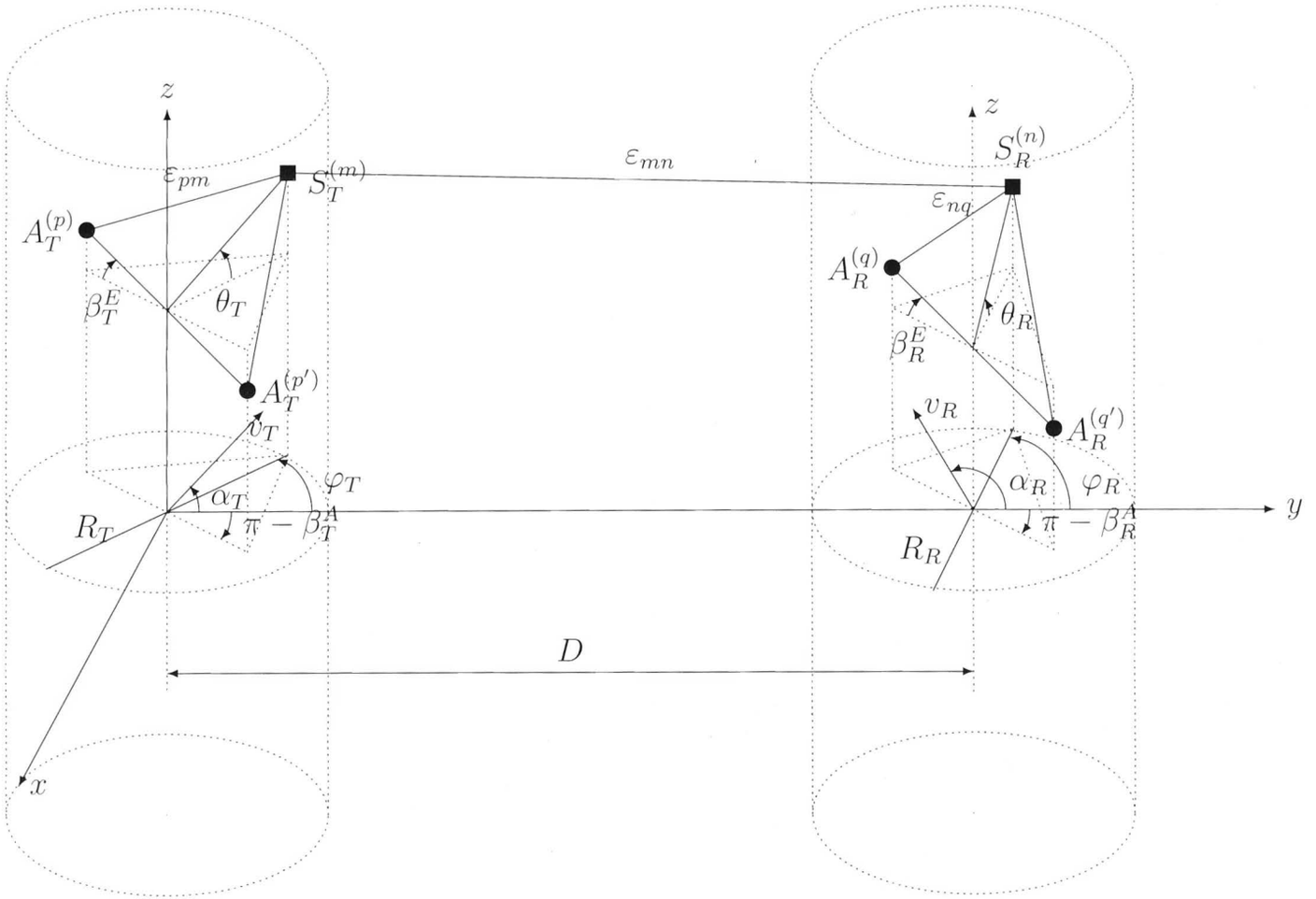

Figure 2.11: The two cylinder model for MIMO M2M channel with $n_T = n_R = 2$ antenna elements

and R_R, i.e.,

$$\max\{\delta_T, \delta_R\} \ll \min\{R_T, R_R\}.$$

3. The angles of departures (AAoDs and EAoDs) and the angles of arrivals (AAoAs and EAoAs) are random variables and that the angles of departure are independent from the angles of arrival.

4. The phases ϕ_{mn} are random variables uniformly distributed on the interval $[-\pi, \pi)$ and independent from the angles of departures and the angles of arrivals.

5. The number of local scatterers around the Tx and Rx is infinite.

The starting point is the two cylinder model shown in Fig. 2.11. From the two-cylinder model, we observe that the waves from the Tx antenna elements first arrive at the scatterers located on the Tx cylinder. Considering these fixed scatterers as virtual base-stations (VBS), the communication link from each VBS to the Rx is modeled as a 3D F2M link. The signals from each VBS arrive at the Rx antenna from all directions and with equal power due to 3D scattering around the Rx.

The MIMO channel is described by an $n_R \times n_T$ matrix $H(t) = [hij(t)]_{n_R \times n_T}$ of complex low-pass faded envelopes.

The received complex faded envelope of the link $A_T^{(p)} - A_R^{(q)}$ is

$$h_{pq}(t) = \lim_{M,N\to\infty} \frac{1}{\sqrt{MN}} \sum_{m=1}^{M} \sum_{n=1}^{N} e^{j\frac{2\pi}{\lambda}(\epsilon_{pm}+\epsilon_{mn}+\epsilon_{nq})+j\phi_{mn}} \times e^{j2\pi t[f_{T\max}\cos(\varphi_T^{(m)}-\alpha_T)\cos\theta_T^{(m)}+f_{R\max}\cos(\varphi_R^{(n)}-\alpha_R)\cos\theta_R^{(n)}]}, \quad (2.86)$$

where ϵ_{pm}, ϵ_{mn}, and ϵ_{nq} denote distances $A_T^{(p)} - S_T^{(m)}$, $S_T^{(m)} - S_R^{(n)}$, and $S_R^{(n)} - A_R^{(q)}$, respectively. The symbols $\varphi_T^{(m)}$ and $\varphi_R^{(n)}$ denote the AAoD and the AAoA, respectively, while the symbols $\theta_T^{(m)}$ and $\theta_R^{(n)}$ denote the EAoD and the EAoA, respectively.

The distances ϵ_{pm}, ϵ_{mn}, and ϵ_{nq} can be expressed as functions of the random

variables $\varphi_T^{(m)}$, $\varphi_R^{(n)}$, $\theta_T^{(m)}$, and $\theta_R^{(n)}$ as follows:

$$\epsilon_{pm} \approx R_T - \frac{\delta_T}{2}\sin\beta_T^E \sin\theta_T^{(m)} - \frac{\delta_T}{2}\cos\beta_T^E \cos\theta_T^{(m)} \times (\cos\beta_T^A \cos\varphi_T^{(m)} + \sin\beta_T^A \sin\varphi_T^{(m)}), \tag{2.87}$$

$$\epsilon_{nq} \approx R_R - \frac{\delta_R}{2}\sin\beta_R^E \sin\theta_R^{(n)} - \frac{\delta_R}{2}\cos\beta_R^E \cos\theta_R^{(n)} \times (\cos\beta_R^A \cos\varphi_R^{(n)} + \sin\beta_R^A \sin\varphi_R^{(n)}), \tag{2.88}$$

and

$$\epsilon_{mn} \approx D, \tag{2.89}$$

where β_T^A and β_R^A describe the orientation of the Txs antenna array and the Rxs antenna array in the x-y plane, respectively, relative to the y-axis while β_T^E and β_R^E describe the elevation of the Txs antenna array and the Rxs antenna array relative to the x-y plane, respectively.

Applying (2.87), (2.88) and (2.89) to (2.86)

$$h_{pq}(t) = \lim_{M,N\to\infty} \frac{1}{\sqrt{MN}} \sum_{m,n=1}^{M,N} a_{p,m} b_{n,q} e^{j\phi_{mn}+j\phi_0} \times e^{j2\pi t[f_{T\max}\cos(\varphi_T^{(m)}-\alpha_T)\cos\theta_T^{(m)} + f_{R\max}\cos(\varphi_R^{(n)}-\alpha_R)\cos\theta_R^{(n)}]} \tag{2.90}$$

where $\phi_0 = -2\pi(R_T + R_R + D)/\lambda$ and parameters $a_{p,m}$ and $b_{n,q}$ are defined as

$$a_{p,m} = e^{j\frac{\pi}{\lambda}\delta_T \sin\beta_T^E \sin\theta_T^{(m)} + j\frac{\pi}{\lambda}\delta_T \cos\beta_T^E \cos\theta_T^{(m)}(\cos\beta_T^A \cos\varphi_T^{(m)} + \sin\beta_T^A \sin\varphi_T^{(m)})}, \tag{2.91}$$

and

$$b_{n,q} = e^{j\frac{\pi}{\lambda}\delta_R \sin\beta_R^E \sin\theta_R^{(n)} + j\frac{\pi}{\lambda}\delta_R \cos\beta_R^E \cos\theta_R^{(n)}(\cos\beta_R^A \cos\varphi_R^{(n)} + \sin\beta_R^A \sin\varphi_R^{(n)})}. \tag{2.92}$$

Note that the constant phase ϕ_0 can be set to zero without loss of generality because it does not affect statistical properties of the model.

A "Concentric-Cylinders" Model.

The "concentric-cylinders" model [34] is an extension of the Geometrical Two-Cylinder model discussed above. As shown in Fig. 2.12, this model defines four cylinders, two around the Tx, and another two around the Rx.

The general assumptions made on this model are:

1. M scatterers lie on L cylindric surfaces of radii $R_{T1} \leq R_T^{(l)} \leq R_{T2}$, where $1 \leq l \leq L$. The l^{th} cylindric surface contains $M^{(l)}$ fixed omnidirectional scatterers, and the $(m,l)^{th}$ transmit scatterer is denoted by $S_T^{(m,l)}$

2. N scatterers lie on K cylindric surfaces of radii $R_{R1} \leq R_R^{(k)} \leq R_{R2}$, where $1 \leq k \leq K$. The k^{th} cylindric surface contains $N^{(k)}$ fixed omnidirectional scatterers, and the $(n,k)^{th}$ receive scatterer is denoted by $S_R^{(n,k)}$

3. Condition
$$\max\{R_{T2}, R_{R2}\} \ll D.$$

4. Condition
$$D \leq \frac{4R_{T1}R_{R1}L_R}{\lambda(n_T-1)(n_R-l)},$$
where λ denotes the carrier wavelength.

5. δ_T and δ_R are much smaller than the radii R_{T1} and R_{R1}, i.e.,
$$\max\{\delta_T, \delta_R\} \ll \min\{R_{T1}, R_{R1}\}.$$

6. The number of local scatterers around the T_X and R_X is infinite.

7. Angles of departures (AAoDs and EAoDs), the angles of arrivals (AAoAs and EAoAs), and the radii $R_T^{(l)}$ and $R_R^{(k)}$ are random variables.

8. Since all rays are double-bounced, the angles of departure and radii $R_T^{(l)}$ are independent from the angles of arrival and radii $R_R^{(k)}$

9. Phases ϕ_{mn} are random variables uniformly distributed on the interval $[-\pi, \pi)$ and independent from the angles of departure, the angles of arrival, and the radii of the cylinders

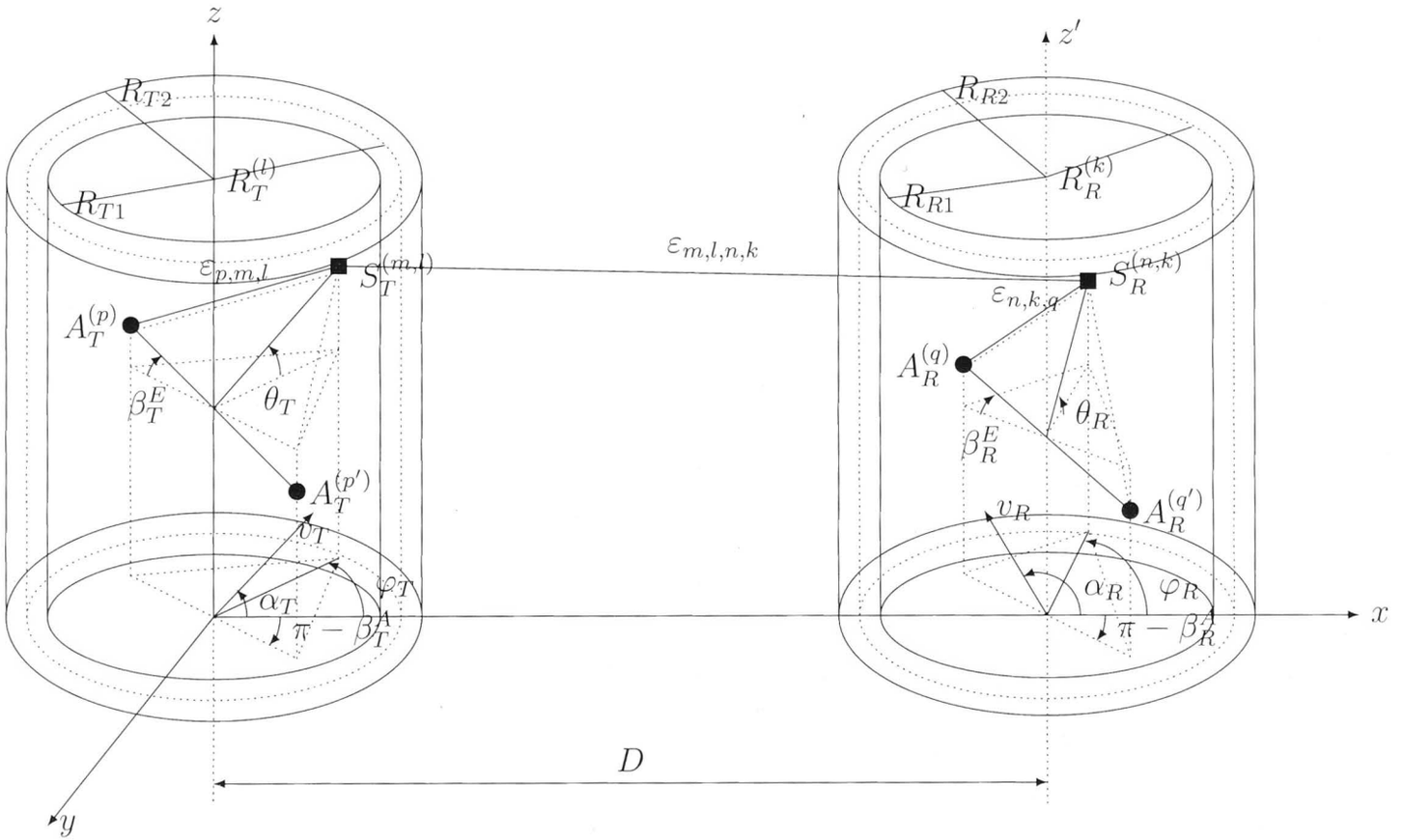

Figure 2.12: The "concentric-cylinders" model for MIMO M2M channel with $n_T = n_R = 2$ antenna elements

The input delay-spread function of the link $A_T^{(p)} - A_R^{(q)}$ is given by

$$h_{pq}(t,\tau) = \lim_{M,N\to\infty} \sum_{l,m=1}^{L,M^{(l)}} \sum_{k,n=1}^{K,N^{(k)}} \eta_{l,k} g_{m,l,n,k}(t)\delta(\tau - \tau_{m,l,n,k}), \tag{2.93}$$

where parameters $\eta_{l,k}$, $\tau_{m,l,n,k}$ denote amplitudes of the multipath components and time delays, respectively. Function $g_{m,l,n,k}(t)$ is defined as follows:

$$\begin{aligned} g_{m,l,n,k}(t) = {} & e^{-j\frac{2\pi}{\lambda}(\epsilon_{p,m,l}+\epsilon_{m,l,n,k}+\epsilon_{n,k,q})+j\phi_{m,l,n,k}} \\ & \times e^{j2\pi t[f_{Tmax}\cos(\varphi_T^{(m,l)}-\alpha_T)+f_{R\max}\cos(\varphi_R^{(n,k)}-\alpha_R)]}, \end{aligned} \tag{2.94}$$

where $\epsilon_{p,m,l}$, $\epsilon_{m,l,n,k}$, and $\epsilon_{n,k,q}$ denote distances $A_T^{(p)} - S_T^{(m,l)}$, $S_T^{(m,l)} - S_R^{(n,k)}$, and $S_R^{(n,k)} - A_R^{(q)}$, respectively, while $\varphi_T^{(m,l)}$ and $\varphi_R^{(n,k)}$ denote the AAoD and the AAoA, respectively.

The amplitude of the multipath component, $\eta_{l,k}$ is defined as

$$\begin{aligned} \eta_{l,k} &= \frac{\sqrt{P_{pq}}\lambda}{4\pi\sqrt{M^{(l)}N^{(k)}}}(R_T^{(l)} + D + R_R^{(k)})^{-\gamma/2} \\ &\approx \Omega_{pq}(1 - \frac{\gamma}{2}\frac{R_T^{(l)} + R_R^{(k)}}{2D}), \end{aligned} \tag{2.95}$$

where P_{pq} denotes the power transmitted through the sub channel $A_T^{(p)} - A_R^{(q)}$, γ is the propagation path loss exponent, and

$$\Omega_{pq} = \frac{D^{\gamma/2}\sqrt{P_{pq}}\lambda}{4\pi\sqrt{M^{(l)}N^{(k)}}}. \tag{2.96}$$

The time delay $\tau_{m,l,n,k}$ is defined as the travel time of the wave received on the scatterer $S_T^{(m,l)}$ and scattered from the scatterer $S_R^{(n,k)}$ i.e.,

$$\tau_{m,l,n,k} = \frac{D}{c_0} + \frac{R_T^{(l)}}{c_0}(1 - \cos\varphi_T^{(m,l)})\cos\theta_T^{(m,l)} + \frac{R_R^{(k)}}{c_0}(1 + \cos\varphi_R^{(n,k)})\cos\theta_R^{(n,k)},$$

where c_0 is the speed of light.

The distances $\epsilon_{p,m,l}$, $\epsilon_{n,k,q}$, and $\epsilon_{m,l,n,k}$ can be expressed as functions of the

random variables $\varphi_T^{(m,l)}$, $\varphi_R^{(n,k)}$, $\theta_T^{(m,l)}$, $\theta_R^{(n,k)}$, $R_T^{(l)}$, and $R_R^{(k)}$ as follows:

$$\begin{aligned}\epsilon_{p,m,l} \approx\ & R_T^{(l)} / \cos\theta_T^{(m,l)} - (0.5L_T + 0.5 - p)[d_{Tz}\sin\theta_T^{(m,l)} \\ & + d_{Tx}\cos\varphi_T^{(m,l)}\cos\theta_T^{(m,l)} + d_{Ty}\sin\varphi_T^{(m,l)}\cos\theta_T^{(m,l)}]\end{aligned} \tag{2.97}$$

$$\begin{aligned}\epsilon_{n,k,q} \approx\ & R_r^{(k)} / \cos\theta_R^{(n,k)} - (0.5L_r + 0.5 - q)[d_{Rz}\sin\theta_R^{(n,k)} \\ & + d_{Rx}\cos\varphi_R^{(n,k)}\cos\theta_R^{(n,k)} + d_{Ry}\sin\varphi_R^{(n,k)}\cos\theta_R^{(n,k)}]\end{aligned} \tag{2.98}$$

and

$$\epsilon_{m,l,n,k} \approx D, \tag{2.99}$$

where parameters p and q take values $p \in \{1,\ldots,n_T\}$ and $q \in \{1,\ldots,n_R\}$,

$$d_{Tx} = d_T \cos\beta_T^E \cos\beta_T^A, \tag{2.100}$$

$$d_{Ty} = d_T \cos\beta_T^E \sin\beta_T^A, \tag{2.101}$$

$$d_{Rx} = d_R \cos\beta_R^E \cos\beta_R^A, \tag{2.102}$$

$$d_{Ry} = d_R \cos\beta_R^E \sin\beta_R^A, \tag{2.103}$$

$$d_{Tz} = d_T \sin\beta_T^E, \tag{2.104}$$

and

$$d_{Rz} = d_R \sin\beta_R^E. \tag{2.105}$$

The time-variant transfer function is used instead of the input delay-spread function in the below derivations. The time-variant transfer function is defined as the Fourier transform of the input delay-spread function, and using (2.93)–(2.99) can be written as:

$$\begin{aligned}T_{pq}(t,f) = \mathcal{F}_\tau\{h_{pq}(t,\tau)\} = \lim_{M,N\to\infty} & \sum_{l,m,k,n=1}^{L,M^{(l)},K,N^{(k)}} e^{j\phi_{m,l,n,k} - j\frac{2\pi}{c_0}fD} \\ & \times \Omega_{pq}\Big(1 - \frac{\gamma}{2}\frac{R_T^{(l)} + R_R^{(k)}}{2D}\Big) a_{p,m,l} b_{n,k,q} e^{j2\pi t f_{Tmax}\cos(\varphi_T^{(m,l)} - \alpha_T)}\end{aligned}$$

$$\times e^{j2\pi t f_{Rmax}\cos(\varphi_R^{(n,k)}-\alpha_R)-j\frac{2\pi}{c_0}f[\frac{R_T^{(l)}(1-\cos\varphi_T^{(m,l)})}{\cos\theta_T^{(m,l)}}+\frac{R_R^{(k)}(1-\cos\varphi_R^{(n,k)})}{\cos\theta_R^{(n,k)}}]} \tag{2.106}$$

where parameters $a_{p,,m,l}$ and $b_{n,k,q}$ are defined as

$$\begin{aligned} a_{p,,m,l} &= e^{j\frac{2\pi}{\lambda}(0.5L_T+0.5-p)d_{Tx}\cos\varphi_T^{(m,l)}\cos\theta_T^{(m,l)}} \\ &\times e^{j\frac{2\pi}{\lambda}(0.5L_T+0.5-p)[d_{Tx}\sin\varphi_T^{(m,l)}\cos\theta_T^{(m,l)}+d_{Tz}\sin\theta_T^{(m,l)}]} \end{aligned} \tag{2.107}$$

and

$$\begin{aligned} b_{n,k,q} &= e^{j\frac{2\pi}{\lambda}(0.5L_R+0.5-q)d_{Rx}\cos\varphi_R^{(n,k)}\cos\theta_R^{(n,k)}} \\ &\times e^{j\frac{2\pi}{\lambda}(0.5L_R+0.5-q)[d_{Ry}\sin\varphi_R^{(n,k)}\cos\theta_R^{(n,k)}+d_{Rz}\sin\theta_R^{(n,k)}]} \end{aligned} \tag{2.108}$$

A "Concentric-Cylinders" Model with LoS, Single Bounced Transmit (SBT), Single Bounced Receive (SBR), and Double Bounced (DB) Rays Model.

The "Concentric-Cylinders" model with LoS, SBT, SBR, and DB rays model [35] as shown in Fig. 2.13, is derived based on the concentric-cylinders model discussed in the above section.

The general assumptions made on this model are:

1. M scatterers lie on L cylindric surfaces of radii

$$R_{T1} \leq R_T^{(l)} \leq R_{T2},$$

where $1 \leq l \leq L$. The l^{th} cylindric surface contains $M^{(l)}$ fixed omnidirectional scatterers, and the $(m,l)^{th}$ transmit scatterer is denoted by $S_T^{(m,l)}$, where $1 \leq m \leq M^{(l)}$.

2. N scatterers lie on P cylindric surfaces of radii

$$R_{R1} \leq R_R^{(k)} \leq R_{R2},$$

where $1 \leq k \leq P$. The k^{th} cylindric surface contains $N^{(k)}$ fixed omnidirectional scatterers, and the $(n,k)^{th}$ receive scatterer is denoted by $S_R^{(n,k)}$, where $1 \leq n \leq N^{(k)}$.

3. The radii R_{T2} and R_{R2} are sufficiently smaller than the distance D.

4. The condition
$$D \leq \frac{4R_{T1}R_{R1}L_R}{\lambda(L_T-1)(L_R-1)}$$
should be satisfied, so that the channel does not experience keyhole behavior [36]. Keyhole behavior exhibits low spatial fading correlation at both ends of the link but still has poor rank properties, and hence, low ergodic capacity.

5. δ_T and δ_R are much smaller than the radii R_{T1} and R_{R1}.

6. Angles of departure, i.e., $\varphi_T^{(m,l)}$ and $\theta_T^{(m,l)}$, and the angles of arrival, i.e., $\varphi_R^{(n,k)}$ and $\theta_R^{(n,k)}$, are independent random variables.

7. The radii $R_T^{(l)}$ and $R_R^{(k)}$ are independent random variables.

8. The phases $\phi_{m,l}$, $\phi_{n,k}$ and $\phi_{m,l,n,k}$ are random variables that were uniformly distributed on the interval $[-\pi,\pi)$ and independent of the angles of departure, the angles of arrival, and the radii of the cylinders.

The input delay-spread function of the link $A_T^{(p)} - A_R^{(q)}$ which can be written as a superposition of the LoS, SBT, SBR, and DB rays is given as

$$h_{pq}(t,\tau) = h_{pq}^{\mathrm{SBT}}(t,\tau) + h_{pq}^{\mathrm{SBR}}(t,\tau) + h_{pq}^{\mathrm{DB}}(t,\tau) + h_{pq}^{\mathrm{LoS}}(t,\tau). \tag{2.109}$$

The time variant transfer function [37] which is the Fourier transform of the input delay-spread function given in (2.109) can be written as:

$$\begin{aligned} T_{pq}(t,\tau) &= \mathcal{F}_\tau\{h_{pq}(t,\tau)\} \\ &= T_{pq}^{\mathrm{SBT}}(t,f) + T_{pq}^{\mathrm{SBR}}(t,f) + T_{pq}^{\mathrm{DB}}(t,f) + T_{pq}^{\mathrm{LoS}}(t,f) \end{aligned} \tag{2.110}$$

where the SBT, SBR, DB rays, and LoS components of the time-variant transfer

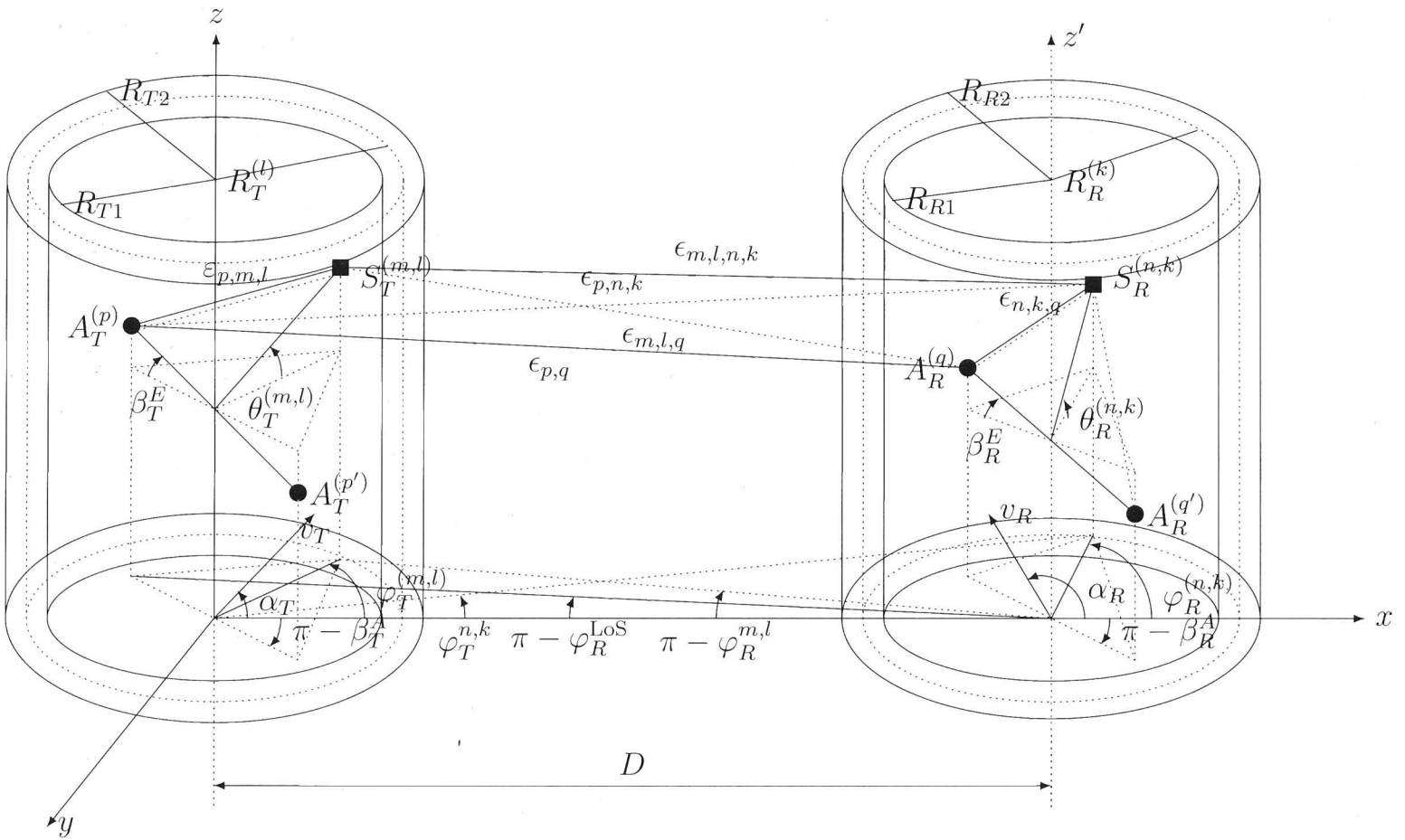

Figure 2.13: Concentric-cylinders model with LoS, SBT, SBR, and DB rays for a MIMO M2M channel with $n_T = n_R = 2$ antenna elements

function are, respectively,

$$T_{pq}^{\mathrm{SBT}}(t,f) = \sqrt{\frac{\eta_T \Omega_{pq}}{K+1}} \lim_{M\to\infty} \sum_{l=1}^{L} \sum_{m=1}^{M^{(l)}} \frac{(1-\frac{\gamma}{2}\frac{R_T^{(l)}}{D})}{\sqrt{M}} a_{p,m,l}^{\mathrm{SBT}} b_{q,m,l}^{\mathrm{SBT}}$$
$$\times e^{j2\pi t f_{Tmax}\cos(\varphi_T^{(m,l)}-\alpha_T)\cos\theta_T^{(m,l)}}$$
$$\times e^{j2\pi f_{Rmax}(\cos\alpha_R - \Delta_T^{(l)}\sin\alpha_R \sin\varphi_T^{(m,l)})\cos(\Delta_T^{(l)}\theta_T^{(m,l)}+\Delta_H/D)}$$
$$\times e^{-j\frac{2\pi}{c_0\cos\theta_T^{(m,l)}} f[D+R_T^{(l)}(1-\cos\varphi_T^{(m,l)})]+j\phi_{m,l}} \tag{2.111}$$

$$T_{pq}^{\mathrm{SBR}}(t,f) = \sqrt{\frac{\eta_R \Omega_{pq}}{K+1}} \lim_{N\to\infty} \sum_{k=1}^{P} \sum_{n=1}^{N^{(k)}} \frac{(1-\frac{\gamma}{2}\frac{R_R^{(k)}}{D})}{\sqrt{N}} a_{p,n,k}^{\mathrm{SBR}} b_{q,n,k}^{\mathrm{SBR}}$$
$$\times e^{j2\pi t f_{Rmax}\cos(\varphi_R^{(n,k)}-\alpha_R)\cos\theta_R^{(n,k)}}$$
$$\times e^{j2\pi f_{Tmax}(\cos\alpha_T - \Delta_R^{(k)}\sin\alpha_T \sin\varphi_R^{(n,k)})\cos(\Delta_R^{(k)}\theta_R^{(n,k)}+\Delta_H/D)}$$
$$\times e^{-j\frac{2\pi}{c_0\cos\theta_R^{(n,k)}} f[D+R_R^{(k)}(1-\cos\varphi_T^{(n,k)})]+j\phi_{n,k}} \tag{2.112}$$

$$T_{pq}^{\mathrm{DB}}(t,f) = \sqrt{\frac{\eta_{TR} \Omega_{pq}}{K+1}} \lim_{M,N\to\infty} \sum_{l,m=1}^{L,M^{(l)}} \sum_{k,n=1}^{P,N^{(k)}} \frac{(1-\frac{\gamma}{2}\frac{R_T^{(l)}+R_R^{(k)}}{2D})}{\sqrt{MN}} a_{p,m,l}^{\mathrm{DB}} b_{q,n,k}^{\mathrm{DB}}$$
$$\times e^{j2\pi t f_{Tmax}\cos(\varphi_T^{(m,l)}-\alpha_T)\cos\theta_T^{(m,l)}} \cdot e^{j2\pi t f_{Rmax}\cos(\varphi_R^{(n,k)}-\alpha_R)\cos\theta_R^{(n,k)}}$$
$$\times e^{-j\frac{2\pi}{c_0} f[D+\frac{R_T^{(l)}(1-\cos\varphi_T^{(m,l)})}{\cos\theta_T^{(m,l)}}+\frac{R_R^{(k)}(1+\cos\varphi_R^{(n,k)})}{\cos\theta_R^{(n,k)}}]+j\phi_{m,l,n,k}} \tag{2.113}$$

$$T_{pq}^{\mathrm{LoS}}(t,f) = \sqrt{\frac{\eta_T \Omega_{pq}}{K+1}} e^{j2\pi t[f_{Tmax}\cos\alpha_T + f_{Rmax}\cos(\pi-\alpha_R)]}$$
$$\times e^{-j\frac{2\pi}{c_0} f\sqrt{D^2+\Delta_H^2}} e^{-j\frac{2\pi}{\lambda}D + j\frac{2\pi}{\lambda}(0.5L_T+0.5-p)\cos\beta_T^A\cos\beta_T^E}$$
$$\times e^{j\frac{2\pi}{\lambda}(0.5L_R+0.5-q)d_R\cos\beta_R^E\cos(\pi-\beta_R^A)}, \tag{2.114}$$

where the symbols $\epsilon_{p,m,l}$, $\epsilon_{m,l,q}$, $\epsilon_{p,n,k}$, $\epsilon_{n,k,q}$, $\epsilon_{m,l,n,k}$ and $\epsilon_{p,q}$ denote distances $A_T^{(p)} - S_T^{(m,l)}$, $S_T^{(m,l)} - A_R^{(q)}$, $A_T^{(p)} - S_R^{(n,k)}$, $S_R^{(n,k)} - A_R^{(q)}$, $S_T^{(m,l)} - S_R^{(n,k)}$, and $A_T^{(p)} - A_R^{(q)}$, respectively, while angles β_T^A and β_R^A describe the orientation of the T_x and R_x

antenna array in the x-y plane, respectively, relative to the x-axis. Similarly, angles β_T^E and β_R^E describe the elevation of the T_xs antenna array and the R_xs antenna array relative to the x-y plane, respectively.

The symbols $\varphi_T^{(m,l)}$ and $\varphi_R^{(n,k)}$ denote AAoDs and AAoAs, respectively. Similarly, the symbols $\theta_T^{(m,l)}$ and $\theta_R^{(n,k)}$ denote EAoDs and EAoAs, respectively. Finally, the symbol $\varphi_{Rq}^{\text{LoS}}$ denotes the AAoAs of the LoS paths.

Observe from the 3D geometrical model that some waves from the T_x antenna may directly traverse to the R_x antenna, whereas other waves are single-bounced at the T_x, single-bounced at the R_x, and/or double-bounced (i.e., the waves from the T_x antenna elements impinge on the scatterers that are located around the T_x and scatter from the scatterers that are located around the R_x) before arriving at the R_x antenna. Hence, the input delay-spread function of the link is $A_T^{(p)} - A_R^{(q)}$.

In (2.111), (2.112), (2.113) and (2.114), K denotes the Rice factor (i.e., the ratio of LoS to scatter received power), γ is the path loss exponent, c_0 is the speed of light, $\Delta_T^{(l)} = R_T^{(l)}/D$, $\Delta_R^{(k)} = R_R^{(k)}/D$, $\Delta_H = h_T - h_R$ $\Omega_{pq} = D^{-\gamma} P_{pq} \lambda^2/(4\pi)^2$ and P_{pq} is the power transmitted through the sub channel $A_T^{(p)} - A_R^{(q)}$. The parameters η_T, η_R, and η_{TR} specify the contribution of the single- and double-bounced rays to the total averaged power, i.e., these parameters satisfy $\eta_T + \eta_R + \eta_{TR} = 1$. Furthermore, the parameters p and q take values from the sets $p \in \{1, \ldots, n_T\}$ and $q \in \{1, \ldots, n_R\}$. Finally, $a_{p,m,l}^{\text{SBT}}$, $b_{q,m,l}^{\text{SBT}}$, $a_{p,m,k}^{\text{SBR}}$, $b_{q,n,k}^{\text{SBR}}$, $b_{q,n,k}^{\text{SBR}}$ and $b_{q,n,k}^{\text{DB}}$ are, respectively,

$$a_{p,m,l}^{\text{SBT}} \approx e^{j\frac{2\pi}{\lambda}(0.5L_T+0.5-p)d_{Tx}\cos\varphi_T^{(m,l)}\cos\theta_T^{(m,l)}} \times e^{j\frac{2\pi}{\lambda}(0.5L_T+0.5-p)[d_{Tx}\sin\varphi_T^{(m,l)}\cos\theta_T^{(m,l)}+d_{Tz}\sin\theta_T^{(m,l)}]} \tag{2.115}$$

$$b_{q,m,l}^{\text{SBT}} \approx e^{j\frac{2\pi}{\lambda}(0.5L_R+0.5-q)d_R\cos\beta_R^E[\Delta_T^{(l)}\sin\beta_R^A\sin\varphi_T^{(m,l)}-\cos\beta_R^A]} \cdot e^{-j\frac{2\pi}{\lambda}(D+R_T^{(l)})} \tag{2.116}$$

$$a_{p,m,k}^{\text{SBR}} \approx e^{j\frac{2\pi}{\lambda}(0.5L_T+0.5-p)d_T\cos\beta_R^E[\Delta_R^{(k)}\sin\beta_T^A\sin\varphi_R^{(n,k)}+\cos\beta_T^A]} \cdot e^{-j\frac{2\pi}{\lambda}(D+R_R^{(k)})} \tag{2.117}$$

$$b_{q,n,k}^{\text{SBR}} \approx e^{j\frac{2\pi}{\lambda}(0.5L_R+0.5-q)d_{Rx}\cos\varphi_R^{(n,k)}\cos\theta_R^{(n,k)}} \times e^{j\frac{2\pi}{\lambda}(0.5L_R+0.5-q)[d_{Ry}\sin\varphi_R^{(n,k)}\cos\theta_R^{(n,k)}+d_{Rz}\sin\theta_R^{(n,k)}]} \tag{2.118}$$

$$a_{p,m,l}^{\text{DB}} \approx e^{j\frac{2\pi}{\lambda}(0.5L_T+0.5-p)d_{Tx}\cos\varphi_T^{(m,l)}\cos\theta_T^{(m,l)}}$$

$$\times e^{j\frac{2\pi}{\lambda}(0.5L_T+0.5-p)[d_{Ty}\sin\varphi_T^{(m,l)}\cos\theta_T^{(m,l)}+d_{Tz}\sin\theta_T^{(m,l)}]}$$
$$\times e^{-j\frac{2\pi}{\lambda}(D/2+R_T^{(l)})} \tag{2.119}$$

$$b_{q,n,k}^{\mathrm{DB}} \approx e^{j\frac{2\pi}{\lambda}(0.5L_R+0.5-q)d_{Rx}\cos\varphi_R^{(n,k)}\cos\theta_R^{(n,k)}}$$
$$\times e^{j\frac{2\pi}{\lambda}(0.5L_R+0.5-q)[d_{Ry}\sin\varphi_R^{(n,k)}\cos\theta_R^{(n,k)}+d_{Rz}\sin\theta_R^{(n,k)}]}$$
$$\times e^{-j\frac{2\pi}{\lambda}(D/2+R_R^{(k)})} \tag{2.120}$$

where $d_{Tz} = d_T \sin\beta_T^E$, $d_{Tx} = d_T \cos\beta_T^E \cos\beta_T^A$, $d_{Ty} = d_T \cos\beta_T^E \sin\beta_T^A$, $d_{Rz} = d_R \sin\beta_R^E$, $d_{Rx} = d_R \cos\beta_R^E \cos\beta_R^A$ and $d_{Ry} = d_R \cos\beta_R^E \sin\beta_R^A$.

2.3.3 Non Geometrical Stochastic Physical Models (NGSPM)

NGSPMs describe paths from Tx to Rx by statistical parameters only, without reference to the geometry of a physical environment.

A SISO NGSPM proposed in [12] is the origin of the channel model standardized by IEEE 802.11p. IEEE 802.11p is the dedicated IEEE standard for vehicular communications and is mainly based on the well-known wireless local area network (WLAN) standard IEEE 802.11a (IEEE, 2007). This model determines physical parameters of a M2M channel in a completely stochastic manner by prescribing underlying probability distribution functions (PDFs) without presuming any underlying geometry. But this is based on experimental results. Therefore, this model offers no conceptual framework to facilitate meaningful generalization into different scenarios. In addition, this pure parameter-based model needs to jointly consider many parameters for modeling MIMO channels, which leads to high complexity [21].

In this section, we discussed most of the available M2M channel models in the literature which are summarized in Table 2.3.

When considering the applicability of the above Channel Models, all the above models are suitable only for specific scattering environments. In contrast, our model introduced in chapter 3 is able to represent any scattering environment by selecting suitable effective random complex scattering gain functions. According

Table 2.3: Summary of available M2M channel models

Channel Model	Model Catrgory	Features
Ray tracing Model [20]	DPM	Each model represents one specific environment at a given time and multiple runs are needed to represent different environments
Akki and Harber Model [2]	GBSPM	2D SISO model
The Geometrical Two-Ring Model [22]	GBSPM	2D narrowband MIMO model, where the complex faded envelope depends on the distance between scatterers and antenna elements.
The Geometrical Double Ring Model [24]	GBSPM	2D narrowband MIMO model, where the complex faded envelope is not dependent on the distance between scatterers and antenna elements.
The Geometrical Modified Two-Ring Model [25]	GBSPM	2D narrowband MIMO model
The Geometrical Two-Erose-Ring Model [27]	GBSPM	2D narrowband MIMO model, where scattering around the transmitter and the receiver are defined in erose model
The Combination of a Two Ring and an Ellipse Model [13]	GBSPM	2D narrowband MIMO M2M Ricean model
The Combination of a Two Ring and a Multiple Confocal Ellipses Model [28]	GBSPM	2D narrowband MIMO M2M multicarrier model
The Geometrical Single Bounce Two Sphere (SBTS) Model [29]	GBSPM	3D narrowband MIMO model
The Geometric Street Scattering Model [30]	GBSPM	The single bounce street model
A Geometrical Two Cylinder Model [31]	GBSPM	3D narrowband MIMO model
A "Concentric-Cylinders" Model [34]	GBSPM	3D wideband MIMO model with non-line-of-sight condition
A "Concentric-Cylinders" Model with LoS, SBT, SBR, and DB Rays Model [35]	GBSPM	3D wideband MIMO model with LoS, SBT, SBR, and DB condition
A SISO Experimental Model [12]	NGSPM	This is based on experimental results

to the literature survey we have carried out, we claim that our model is the only mathematical M2M model which belongs to the NGSPM model.

2.4 M2M Channel Measurements

This section is devoted for the analysis of currently available M2M channel Measurements. The measurements available can be categorized based on six criterias, which are detailed below.

2.4.1 Carrier Frequencies

Most of the measurements were carried out in carrier frequencies of 2.4GHz, 5.2GHz and 5.9GHz. The carrier frequency 2.4GHz is defined in IEEE 802.11b/g band while 5.2GHz in IEEE 802.11a frequency band and 5.9GHz in IEEE 802.11p standard DSRC band.

2.4.2 Frequency Selectivity

Measurements can be based on the range of frequencies used. On this basis, channels can be categorized as narrowband or wideband. Channels are categorized as wideband when the signal bandwidth is larger than the coherence bandwidth, which is the minimum frequency separation between independent channel fades.

2.4.3 Antenna Systems

Most M2M measurement campaigns so far have focused on single-antenna applications, resulting in SISO systems. MIMO systems, with multiple antennas at both ends, are very promising candidates for future communication systems and are gaining more importance in IEEE 802.11 standards.

2.4.4 Environments

Measurements can be obtained from four different classes of environments, namely urban, suburban (village), motor-way and highway.

2.4.5 Transmitter and Receiver Direction of Motion

Directions of motion of the transmitter and receiver also affect channel statistics, e.g., Doppler effects. The direction can be either in the same direction or in opposite directions depending on the transmitter and receiver movements.

2.4.6 Channel Statistics

Channel statistics have been explored mainly under two categorizations, amplitude distribution and Doppler power spectral density (PSD), but we extend our analysis to include the statistics such as packet error rate, maximum range and latency, correlation functions and level crossing rate. The details of our classification under channel statistics are given in more details below. These statistics are compared with our new M2M channel model introduced in the next chapter.

Amplitude Distribution

M2M measurement campaigns in [38–41] have investigated on amplitude distribution. The paper [38] presents the results of 60GHz M2M radio channel measurements which were carried out on highways, rural roads and in urban surroundings for distances up to 500m, and the distribution function of the received power is presented.

In [39] the cumulative distribution function (CDF) of the received signal is analyzed on narrowband measurements at 5.2GHz. In that the measured results are compared with analytical functions such as Rice, Rayleigh, Gaussian or Nakagami distribution. The information from the CDF can be used to estimate the outage probability of the communication system [39]. The study in [40] presents narrowband measurements of the mobile vehicle-to-vehicle propagation channel at 5.9GHz, under realistic suburban driving conditions.

The results of a wideband channel measurement campaign using omnidirectional monopole antennas for the M2M channel in the 5GHz band are presented in [41]. Also, they have classified the measurement environments into the following types: Urban-Antenna Outside Car, Urban-Antenna Inside Car, Small City, Highway Low Traffic Density and Highway High Traffic Density. The measurements

for this campaign were taken in the 5GHz band, at a center frequency of 5.12GHz. This frequency is in an aeronautical radio navigation (ARN) band, i.e., specifically the microwave landing system (MLS) extension band, which is designated for use in large airports. Since the wavelengths in this MLS band and the unlicensed band at 5.2 GHz are very close, the characteristics measured in the ARN band should essentially be the same as those in the unlicensed band directly above the ARN band in frequency.

Power Delay Profile

Since different paths are of different lengths, a single impulse sent from the transmitter will result in multiple copies being received at different times at receiver called power delay profile. M2M measurement campaigns in [41–43] have investigated power delay profile.

In [42] the measurements were taken using the direct sequence spread spectrum technique at 2.45GHz while in [41], the measurements were for M2M communication channels in the 5GHz band. The paper [43] presents results on power-delay profiles from a high speed measurement campaign on a highway. Measurements were performed at a carrier frequency of 5.2GHz with the communicating vehicles traveling on the highway in opposite directions.

Power Spectral Densities (PSD)

The spectral definitions for time Doppler channels are equally valid for use with other channel dependencies. Thus, the Doppler PSD is used for time varying channels, the delay PSD is used for frequency varying channels, and the wave number PSD is used for space varying channels. Engineers often refer to these PSDs as simply the Doppler spectrum, the delay spectrum, and the wavenumber.

M2M measurement campaigns in [12, 35, 39–43], have investigated channel characteristics of power spectral density.

The short time variations of the M2M transmission channel are characterized by the normalized Doppler PSD of the complex fast fading component of the received signal [39]. The space Doppler PSD of the time variant transfer function is the Fourier transform of the space-time correlation function and the power space

delay spectral density of the time variant transfer function is the inverse Fourier transform of the space-frequency correlation function [35].

Short and long time Doppler spectrum are discussed in [42] where the measurements were taken at 2.45GHz. The environments chosen for their exceptionally long delay spreads include an expressway, an urban T-intersection, and an exit ramp. The joint Doppler delay characteristics of a different environment based on measurements at 5.9GHz is given in [12].

Packet Error Rate

Packet error rates are taken as channel statistics in [38] and [12]. In [38] Results from the packet error rates in the 60 GHz mobile radio channel, In [12] the packet error rate (PER), measured using testing approach was based on the ping application of the Internet protocol version 6.

Maximum Range and Latency

Metrics such as maximum range and latency are found to be examined in detail only in [44] where they describe field trials of 802.11p technology using the 5.9GHz frequency band with test vehicles. The range is the maximum distance at which a frame is successfully received by the receptor vehicle from the emitter. They have investigated the average ranges for the main scenario, at all tested speeds. In [44] they define latency as the temporal delay between the generation of a frame at the emitting device, and its reception at the receptor device. In other words it is the time when the message is generated and sent to the transport layer through the socket. Similarly, the reception time is set at the instant the frame is read by the application in the receptor vehicle.

Correlation Functions

According to our literature review, [41] and [35] are the only publications found available for correlation related measurements. In [35] space-time frequency (STF) correlation function is discussed where each van was equipped with a linear antenna array, which consists of four vertically polarized magnetic-mount 2.435GHz

antenna elements. In [41], they have described measurements and results for frequency correlations coefficients for multiple M2M environments in the 5GHz band. Channel measurements were made with the transmitter and receiver in two vans and data were collected in various cities and on highways.

Level Crossing Rate

Another important statistical parameter is the level crossing rate (LCR). The LCR indicates how often the received signal level drops below a predefined threshold per second. This information is used to estimate the number of outages per second of the communication system [39]. The LCR is determined by the CDF and the Doppler spectrum of the fast fading component [39]. We found [39] and [35] to be the only papers that include experiment results on LCR statistics. LCR in an urban surface street area and an interstate highway is discussed in [35] at 2.435GHz while, [39] discusses LCR in M2M narrowband at 5.2GHz for four different classes of environments: urban, suburban, motor-way and highway. We use these results in Chapter 6 as corroborating evidence in validating LCR results of our novel M2M model.

2.5 Simulation Methods for M2M

As explained in the above sections, modeling M2M communication systems plays a major role in the design of M2M communication systems. Simulation of M2M radio fading channels also plays an equally important role in the design of M2M communication systems as it helps to test and verify the performance under various channel impairments [45–47]. The necessity of the simulation methods is emphasized by the reference models which assume an infinite number of scatterers preventing practical implementation. Simulation methods having a finite number of scatterers are desirable in matching the statistical properties of the reference models [24].

Simulation methods found in the literature can be mainly categorized under Line Spectrum (LS) method, The Sum-of-Sinusoids (SoS) method and Inverse Fast Fourier Transform (IFFT) filtering based method. These methods are described

in detail in the sections to follow.

2.5.1 Line Spectrum Method

Wang and Cox in [48] proposed a method based on approximating the continuous Doppler spectrum by a discrete line spectrum to simulate M2M channels. This simulation method is called line spectrum (LS) method and it is a modification to the spectrum sampling (SS) method introduced in [49]. The SS method involves sampling Doppler spectrum over in equal intervals while in the LS method the set of frequencies is not equally spaced. The LS methods was used in [45] to assess the model performance in terms of auto-correlation. However, LS is not always suitable for realtime hardware or software simulation as it requires numerical integration of the Doppler spectrum.

2.5.2 The Sum-of-Sinusoids (SoS) Method

The SoS method for F2M was first proposed in [50] where the Rayleigh faded envelopes are simulated using the SoS method by summing several sinusoids which have carefully selected frequencies. An improved version of this method was presented in [51] to simulate waveforms with better accuracy and was extended to simulate M2M channels in [45].

The random processes underlying the M2M reference models are approximated by the superposition of a finite number of properly selected functions in the SoS method [34]. Further, when SoS models have sinusoids with fixed phases, amplitudes, and Doppler frequencies for all simulation trials they are called as deterministic SoS models while when there is at least one of the parameter sets (amplitudes, phases, or Doppler frequencies) as random variables that vary with each simulation trial, they are called as statistical SoS models. Based on these properties, an ergodic statistical (deterministic) model is one that converges to the desired properties in a single simulation trial while the statistical properties of the statistical SoS models vary for each simulation trial, but converge to the desired properties when averaged over a large number of simulation trials [24].

Deterministic SoS Simulation Model

Deterministic SoS models have sinusoids with fixed phases, amplitudes, and Doppler frequencies for all simulation trials [34]. This model is also called an ergodic statistical SoS simulation model.

The deterministic SoS was first proposed in [47] which was called the Modified Method of Exact Doppler Spreads (MMEDS). By choosing only the phases to be random variables, the statistical properties of this model converge to those of the reference model in a single simulation trial. The main disadvantages in MMEDS model is that the statistical properties match those of the reference model only for a small range of normalized time delays. In addition, this model requires a large number of scatterers to match statistical properties of the reference model.

The initial model was further extended for narrowband 2D MIMO isotropic scattering environment in [24] and for 2D non-isotropic scattering environment in [11].

A deterministic SoS simulation model for 3D MIMO is proposed in [1, 34, 52] where [1] is for narrowband channel while the latter two are for wideband channels.

Statistical SoS Simulation Model.

In contrast to the deterministic SoS model, statistical SoS models have at least one of the parameter sets out of amplitudes, phases, or Doppler frequencies as random variables that vary with each simulation trial. Though the statistical properties of these models vary for each simulation trial, they converge to the desired properties when averaged over a large number of simulation trials [34].

Statistical SoS simulation model for narrowband 2D MIMO isotropic scattering environment is discussed in [24] while 2D non-isotropic scattering environment is discussed in [11].

The 3D models under statistical SoS simulation are discussed in [1, 34, 52], where the narrowband channel is discussed in the first model while the wideband channels are discussed in other two models.

2.5.3 Modified IFFT Filtering Based Method

Conventionally, the spectrum sampling method is used in conjunction with IFFT filtering to obtain Rayleigh faded waveforms. This method was originally presented by Smith [53] and modified by Young and Beaulieu [54]. This method is shown to have several advantages such as speed of execution and generated random variables having a closer match to the ideal distribution [54]. Hence, In [45] proposes a modification to F2M IFFT filtering based simulation method for simulating M2M channels.

Wang and Cox do not use equi-spaced frequencies and hence, their method precludes the use of IFFT filtering [45].

In [55] proposes a method to simulate the Rician faded M2M local in three-dimensional scattering scenario, which uses IFFT of the inphase and quadrature components for their simulation process.

The paper [56] presents a Rayleigh fading M2M channel simulator based on a modified Karhunen-Loève orthogonal expansion of a complex Gaussian fading process. The method is similar to the well-known IFFT method but with a different frequency mask.

We infer that the proposed sum-of-sinusoids method is better than the existing approach because it does not involve any numerical integrations and it can generate longer duration waveforms without any periodicity. Comparing the sum-of-sinusoids method with the IFFT method, the IFFT method is more efficient, but requires evaluation of elliptic integrals [45].

2.6 Summary

Though not exhaustive, we have detailed in this chapter most of the available M2M channel models starting with our classification of M2M channel models. Under this categorization the majority of the available channel models come under geometry-based stochastic models and they are valid only in specific channel environments. In contrast, we shall see that our novel channel model can be used in any environment by choosing suitable parameters.

The available M2M channel measurements are discussed under six categories,

which are used throughout this thesis. Finally, we analyze available simulation methods.

When analyzing the channel models discussed above, we could see few common issues in them such as the channel models being relevant only for a given environment, channel model transfer functions consisting of a number of physical parameters where these parameters are difficult to find in practical scenarios. Due to these limitations, it is not easy to create a generalized channel model out of the channel models in the literature. We address these limitations in our novel channel model discussed in the chapters to follow.

Chapter 3

Novel Mobile to Mobile Channel Model

3.1 Introduction

As discussed in Chapter 2, mobile to mobile (M2M) channel models can be divided into physical and analytical models. When analyzing the available models in the literature, evidently all of them fall under physical models, which can be further divided into deterministic models, geometry-based stochastic models and non geometrical stochastic models. There appears to be only one model [12] under the non geometrical stochastic model category in the literature. This model is an experimental model and cannot be utilized to carry out further mathematical analysis. In order to fill this gap, we propose a novel mathematical wireless channel model under non geometrical stochastic model category based on the underlying physics of free space wave propagation. This model extends the fixed-to-mobile (F2M) channel model proposed in [57].

The main goal of this chapter is to introduce novel M2M channel models based on channel types, number of antennas and scattering environments. Under channel types we discuss narrowband (flat fading) and wideband (frequency selective) models while multiple input multiple output (MIMO) and special cases of MIMO such as single input single output (SISO), single input multiple output (SIMO), multiple input single output (MISO) are considered when varying the number of

antennas at transmitter and receiver. These selections are further applied to two dimensional (2D) and three dimensional (3D) scattering environments.

To reach the high demand of video related applications for M2M high speed communications, multicarrier MIMO M2M systems have been suggested where information is transmitted on more than one carrier frequencies. These lead to the increasing need for effective multicarrier MIMO M2M channel models. Catering for this need, we extend our proposed single carrier M2M model to a multicarrier M2M model in the latter part of this chapter.

All the available M2M channel models discussed in the literature are based on specific geometrical situations and one shortcoming of them is that they cannot be utilized to represent general scattering scenarios. As the models we propose are generalized models, they can be applied to any scattering environment forming an ideal framework to inform the design M2M communication systems.

The rest of this chapter is organized as follows. We introduce a narrowband MIMO M2M channel model and discuss SISO, SIMO, MISO as special cases in Section 3.2. The SISO model we introduce here is used in other chapters for further analysis as it is simpler. In Section 3.3 and Section 3.4 the narrowband models are applied to 2D and 3D scattering environments, which can be used for further analysis. We extend these models for multicarrier MIMO M2M channel model in Section 3.5. Finally, Section 3.6 concludes the chapter.

3.2 Novel MIMO M2M Channel Model

In modeling the M2M propagation channel, it is convenient to think of the channel as a filter with a time-varying characteristic. The objective here is to determine this time-varying filter.

We consider a MIMO M2M channel model depicted in Fig. 3.1, where the mobile transmitter is located inside a scatterer-free sphere of radius r_T (region (a)) and the mobile receiver is located inside a scatterer-free sphere of radius r_R (region (b)). It is assumed that scatterers are located outside the two scatterer-free transmit and receive regions (region (c)) and are in the far-field of the receiver and transmitter regions. We assume the transmitter is moving at a constant velocity magnitude u in the direction of unit vector $\widehat{\boldsymbol{u}}$ and the receiver is moving at a

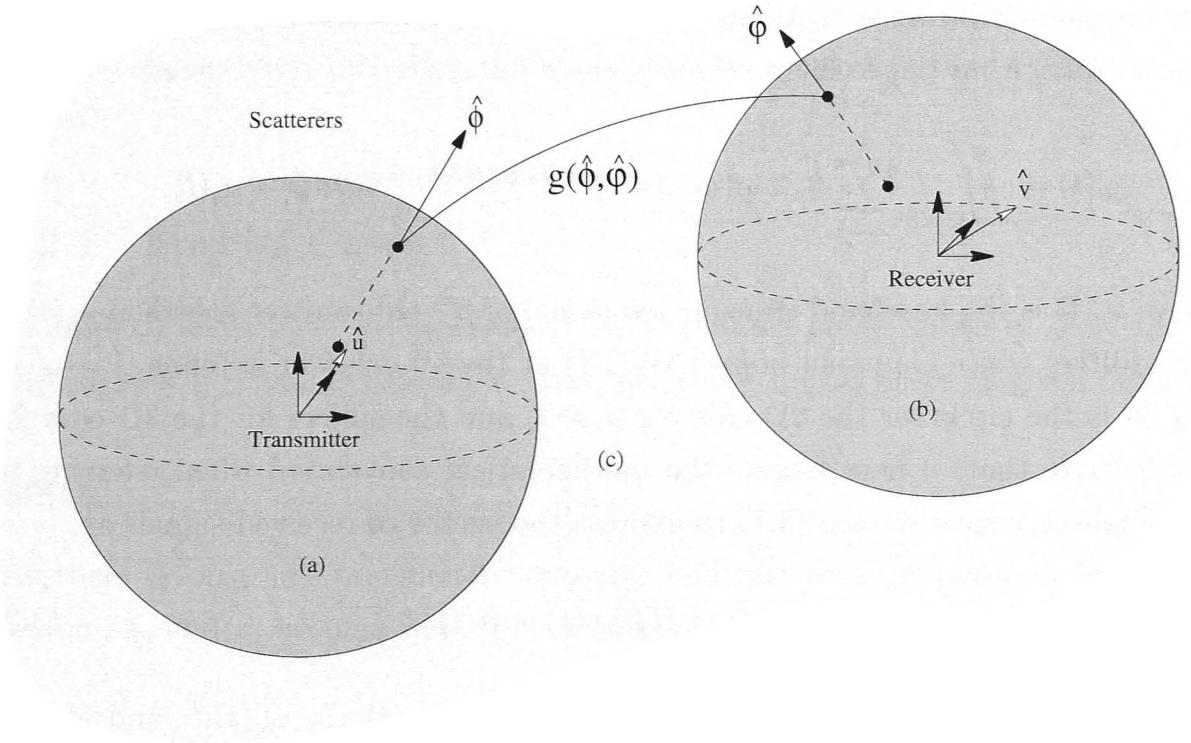

Figure 3.1: A general scattering model for a M2M wireless communication system.

constant velocity magnitude v in the direction of unit vector $\widehat{\boldsymbol{v}}$. When comparing Fig. 3.1 with Fig. 2.9, it is clear that in representing the model in Fig. 2.9, more geometrical properties have to be considered while it is not needed in our model. The same figure and assumptions will be used in Section 3.5 for multicarrier MIMO M2M channel model as well.

In this MIMO M2M channel model $g(\widehat{\phi}, \widehat{\varphi})$ represents the effective random complex scattering gain function for a signal leaving the transmitter scatterer-free region at a direction $\widehat{\phi}$ (relative to the transmitter region origin) and entering the receiver scatterer-free region from a direction $\widehat{\varphi}$ (relative to the receiver region origin).

Consider a MIMO system with $n_{_T}$ transmit antennas located at positions s_p, $p = 1, 2, \ldots, n_T$ from a transmitter origin and n_R receiver antennas located at positions z_q, $q = 1, 2, \ldots, n_R$ from a receiver origin, within balls of radius r_T and r_R, respectively; see Fig. 3.1.

Let $\boldsymbol{x}(t) = [x_1(t), x_2(t), \ldots, x_{n_T}(t)]^T$ be the vector of baseband transmitted

signals from the n_T transmitters during a signaling interval. Then the baseband received signal during a signaling interval at time t by the q^{th} receiver antenna located at z_q from the receiver origin is given by

$$y_q(t) = \iint_{\mathbb{S}^n \times \mathbb{S}^n} \sum_{p=1}^{n_T} x_p(t) g(\widehat{\boldsymbol{\phi}}, \widehat{\boldsymbol{\varphi}}) e^{-ika_p \widehat{\boldsymbol{a}}_p \cdot \widehat{\boldsymbol{\phi}}} e^{ikb_q \widehat{\boldsymbol{b}}_q \cdot \widehat{\boldsymbol{\varphi}}} \, d\widehat{\boldsymbol{\phi}} \, d\widehat{\boldsymbol{\varphi}} + n_q(t), \tag{3.1}$$

where $x_p(t)$ is the baseband transmitted signal of p^{th} transmitter antenna, $n_q(t)$ is the additive white Gaussian noise (AWGN) at the q^{th} receiver antenna, $i = \sqrt{-1}$ and $\mathbb{S}^n$ is the circle for the 2D case for $n = 1$, and the sphere for the 3D case for $n = 2$ (note that, n here follows the mathematical convention when referring to the n-sphere.) Now we use (3.1) to express the vector of received signals as

$$\boldsymbol{y}(t) = H(t)\boldsymbol{x}(t) + \boldsymbol{n}(t), \tag{3.2}$$

where $\boldsymbol{y}(t) = [y_1(t), y_2(t), \ldots, y_q(t)]^T$, $\boldsymbol{n}(t) = [n_1(t), n_2(t), \ldots, n_q(t)]^T$, and $H(t)$ is a $P \times Q$ time-varying channel matrix with (p, q) elements given by

$$h_{pq}(t) = \iint_{\mathbb{S}^n \times \mathbb{S}^n} g(\widehat{\boldsymbol{\phi}}, \widehat{\boldsymbol{\varphi}}) e^{-ika_p(t) \widehat{\boldsymbol{a}}_p \cdot \widehat{\boldsymbol{\phi}}} e^{ikb_q(t) \widehat{\boldsymbol{b}}_q \cdot \widehat{\boldsymbol{\varphi}}} \, d\widehat{\boldsymbol{\phi}} \, d\widehat{\boldsymbol{\varphi}}, \tag{3.3}$$

where

$$a_p(t)\widehat{\boldsymbol{a}}_p = s_p - tu\widehat{\boldsymbol{u}}$$

is the position of the p^{th} transmitter antenna at time t and

$$b_q(t)\widehat{\boldsymbol{b}}_q = z_q - tv\widehat{\boldsymbol{v}}$$

is the position of the q^{th} receiver antenna at time t.

Thus, with the above formulation we take the following to be an element of the time-varying MIMO matrix channel model:

$$h_{pq}^{\text{MIMO}}(t) = \iint_{\mathbb{S}^n \times \mathbb{S}^n} g(\widehat{\boldsymbol{\phi}}, \widehat{\boldsymbol{\varphi}}) e^{-ika_p(t) \widehat{\boldsymbol{a}}_p \cdot \widehat{\boldsymbol{\phi}}} e^{ikb_q(t) \widehat{\boldsymbol{b}}_q \cdot \widehat{\boldsymbol{\varphi}}} \, d\widehat{\boldsymbol{\phi}} \, d\widehat{\boldsymbol{\varphi}}. \tag{3.4}$$

Equation (3.4) represents a general model of a spatial channel where $g(\widehat{\boldsymbol{\phi}}, \widehat{\boldsymbol{\varphi}})$ cap-

tures complex gains due to scatterers and the factors $e^{-ika_p(t)\widehat{\boldsymbol{a}}_p}$ and $e^{ikb_q(t)\widehat{\boldsymbol{b}}_q}$ represent the free-space wave propagation inside the scatterer-free transmit and receiver regions, respectively, including the effects due to transmitter and receiver movements.

3.2.1 Special Cases

In order to show how the generalized M2M channel model given in (3.4) can be used in specific channel models, we consider three special cases as given below.

SISO

As there is only one transmitter antenna and one receiver antenna in a SISO system, s_p and z_q become zero. This results in:

$$a_p(t)\widehat{\boldsymbol{a}}_p = -tu\widehat{\boldsymbol{u}}$$

and

$$b_q(t)\widehat{\boldsymbol{b}}_q = -tv\widehat{\boldsymbol{v}}.$$

Applying these values to (3.4), we derive the following to be the time-varying scalar SISO channel model:

$$h^{\mathrm{SISO}}(t) = \iint_{\mathbb{S}^n \times \mathbb{S}^n} g(\widehat{\boldsymbol{\phi}}, \widehat{\boldsymbol{\varphi}}) e^{iktu\widehat{\boldsymbol{u}}\cdot\widehat{\boldsymbol{\phi}}} e^{-iktv\widehat{\boldsymbol{v}}\cdot\widehat{\boldsymbol{\varphi}}} d\widehat{\boldsymbol{\phi}}\, d\widehat{\boldsymbol{\varphi}}. \tag{3.5}$$

SIMO

For SIMO systems, s_p becomes zero as there is only one transmitter antenna. Then applying

$$a_p(t)\widehat{\boldsymbol{a}}_p = -tu\widehat{\boldsymbol{u}}$$

to (3.4), an element of the time-varying SIMO vector channel model is expressed as:

$$h_q^{\mathrm{SIMO}}(t) = \iint_{\mathbb{S}^n \times \mathbb{S}^n} g(\widehat{\boldsymbol{\phi}}, \widehat{\boldsymbol{\varphi}}) e^{iktu\widehat{\boldsymbol{u}}\cdot\widehat{\boldsymbol{\phi}}} e^{ikb_q(t)\widehat{\boldsymbol{b}}_q\cdot\widehat{\boldsymbol{\varphi}}}\, d\widehat{\boldsymbol{\phi}}\, d\widehat{\boldsymbol{\varphi}}. \tag{3.6}$$

MISO

As there is only one receiver antenna in a MISO system, z_q becomes zero. Then applying

$$b_q(t)\widehat{\boldsymbol{b}}_q = -tv\widehat{\boldsymbol{v}}$$

to (3.4), an element of the time-varying MISO vector channel model is revealed as:

$$h_p^{\text{MISO}}(t) = \iint_{\mathbb{S}^n \times \mathbb{S}^n} g(\widehat{\boldsymbol{\phi}}, \widehat{\boldsymbol{\varphi}}) e^{-ika_p(t)\widehat{\boldsymbol{a}}_p \cdot \widehat{\boldsymbol{\phi}}} e^{-iktv\widehat{\boldsymbol{v}} \cdot \widehat{\boldsymbol{\varphi}}} \, d\widehat{\boldsymbol{\phi}} \, d\widehat{\boldsymbol{\varphi}}. \tag{3.7}$$

Taking the MIMO M2M channel model in (3.4) as the base, we analyze the 2D scattering environment and 3D scattering environment in the sections to follow.

3.3 2D Scattering Environment

The objective here is to simplify the channel model (3.4) expressed above for a 2D scattering environment.

Consider an environment where the multipath is restricted to the azimuth plane only (2D scattering environment), having no field components arriving at significant elevations. The modal expansion (also known as the Jacobi-Anger expansion) of a plane wave $e^{ik\boldsymbol{x}.\widehat{\boldsymbol{\phi}}}$ is given by [58, page 67]

$$e^{ik\boldsymbol{x}.\widehat{\boldsymbol{\phi}}} = \sum_{n=-\infty}^{\infty} J_n(k\|\boldsymbol{x}\|) e^{in(\phi_x + \pi/2 - \phi)}, \tag{3.8}$$

where $\boldsymbol{x} \equiv (\|\boldsymbol{x}\|, \phi_x)$, $\widehat{\boldsymbol{\phi}} \equiv (1, \phi)$ in the polar coordinates system and $J_n(\cdot)$ are the Bessel functions of the first kind of integer order n.

Application of (3.8) in (3.4) yields

$$h_{pq}(t) = \sum_{m=-\infty}^{\infty} \sum_{n=-\infty}^{\infty} \alpha_m^n J_m(ka_p(t)) J_n(kb_q(t)) e^{-im(\phi_a + \pi/2)} e^{in(\phi_b + \pi/2)}, \tag{3.9}$$

where $\widehat{\boldsymbol{a}}_p \equiv (1, \phi_a)$, $\widehat{\boldsymbol{b}}_q \equiv (1, \phi_b)$, $\widehat{\boldsymbol{\phi}} \equiv (1, \phi)$, $\widehat{\boldsymbol{\varphi}} \equiv (1, \varphi)$ in the polar coordinates system and coefficients α_m^n which characterize the 2D scattering environment sur-

rounding the transmitter and receiver regions are given by

$$\alpha_m^n = \iint_{\mathbb{S}^1 \times \mathbb{S}^1} g(\widehat{\boldsymbol{\phi}}, \widehat{\boldsymbol{\varphi}}) e^{-in\varphi} e^{im\phi} \, d\varphi \, d\phi. \tag{3.10}$$

Also note that scattering coefficients α_m^n are independent of the transmitter and receiver velocities. Hence the α_m^n are invariant to Doppler effects and are fixed for a given scattering distribution type.

Note that Bessel function $J_m(\cdot)$ for $|m| > 0$ exhibits a spatially high-pass characteristic. Therefore, as shown in [59], $J_m(kr) \approx 0$ for $|m| > ker/2$, where $e = 2.71828....$ Using this characteristic of Bessel functions we can truncate the infinite series in (3.9) to obtain:

$$h_{pq}^{\mathrm{MIMO_{2D}}}(t) \cong \sum_{m=-M_T}^{M_T} \sum_{n=-M_R}^{M_R} \alpha_m^n J_m(ka_p(t)) J_n(kb_q(t)) e^{-im(\phi_a + \pi/2)} e^{in(\phi_b + \pi/2)}, \tag{3.11}$$

where $M_T = kea_p(t)/2$, $M_R = keb_q(t)/2$ and $a_p(t)\widehat{\boldsymbol{a}}_p = s_p - tu\widehat{\boldsymbol{u}}$ is the position of the p^{th} transmitter antenna at time t while $b_q(t)\widehat{\boldsymbol{b}}_q = z_q - tv\widehat{\boldsymbol{v}}$ is the position of the q^{th} receiver antenna at time t.

Applying the fact that there is only one transmitter antenna and one receiver antenna in a SISO system to (3.11), the SISO channel for a 2D scattering environment can be derived as

$$h^{\mathrm{SISO_{2D}}}(t) \cong \sum_{m=-M_T}^{M_T} \sum_{n=-M_R}^{M_R} \alpha_m^n J_m(kut) J_n(kvt) e^{-im(\phi_u + \pi/2)} e^{in(\phi_v + \pi/2)}, \tag{3.12}$$

where $a_p(t)\widehat{\boldsymbol{a}}_p = -tu\widehat{\boldsymbol{u}}$, $b_q(t)\widehat{\boldsymbol{b}}_q = -tv\widehat{\boldsymbol{v}}$, $M_T = ketu/2$ and $M_R = ketv/2$.

3.4 3D Scattering Environment

The objective here is to simplify the channel matrix expression given in Section 3.2 for a 3D scattering environment.

Using the spherical harmonic expansion of plane waves, the plane wave $e^{ik\boldsymbol{x}\cdot\widehat{\boldsymbol{y}}}$

can be expanded in 3D as [58, page 32]

$$e^{ik\boldsymbol{x}\cdot\widehat{\boldsymbol{y}}} = \sum_{n=0}^{\infty}\sum_{m=-n}^{n} i^n 4\pi j_n(k\|\boldsymbol{x}\|)Y_{nm}(\widehat{\boldsymbol{x}})Y_{nm}^*(\widehat{\boldsymbol{y}}), \tag{3.13}$$

where $j_n(r)$ is the spherical function, which is related to the Bessel function by

$$j_n(r) = \sqrt{\frac{\pi}{2r}}J_{n+\frac{1}{2}}(r) \tag{3.14}$$

and $Y_{nm}(\cdot)$ are the spherical harmonics, which are defined as:

$$Y_{nm}(\theta,\psi) \triangleq \sqrt{\frac{2n+1}{4\pi}\frac{(n-|m|)!}{(n+|m|)!}}P_n^{|m|}(\cos\theta)e^{im\psi}, \tag{3.15}$$

where $0 \leq \theta \leq \pi$ and $0 \leq \psi < 2\pi$ are the elevation and azimuth angles, respectively, $P_n^m(\cdot)$ are the associated Legendre functions of the first kind, n is the degree and m is the order.

By applying the spherical harmonic expansion (3.13) in (3.4), we obtain the MIMO channel matrix in a 3D scattering environment as:

$$\begin{aligned} h_{pq}(t) =& (4\pi)^2 \sum_{n=0}^{\infty}\sum_{m=-n}^{n} e^{-in\pi/2} j_n(ka_p(t))Y_{nm}(\widehat{\boldsymbol{a}}_p) \\ &\times \sum_{p'=0}^{\infty}\sum_{q'=-p'}^{p'} e^{ip'\pi/2} j_{p'}(kb_q(t))Y_{p'q'}^*(\widehat{\boldsymbol{b}}_q)\alpha_{n,m}^{p',q'}, \end{aligned} \tag{3.16}$$

where

$$\alpha_{n,m}^{p',q'} = \iint_{\mathbb{S}^2\times\mathbb{S}^2} g(\widehat{\boldsymbol{\phi}},\widehat{\boldsymbol{\varphi}})Y_{n,m}(\widehat{\boldsymbol{\phi}})Y_{p',q'}^*(\widehat{\boldsymbol{\varphi}})\, d\widehat{\boldsymbol{\phi}}\, d\widehat{\boldsymbol{\varphi}}$$

are the scattering environment coefficients, which characterize the 3D scattering environment surrounding the receiver and transmitter regions and are independent of the physical configuration of antennas and mobile velocities.

As spherical Bessel functions exhibit a high-pass nature, the infinite summa-

tions in (3.16) can be approximated as

$$h_{pq}^{\mathrm{MIMO_{3D}}}(t) \cong (4\pi)^2 \sum_{n=0}^{M_T} \sum_{m=-n}^{n} e^{-in\pi/2} j_n(ka_p(t)) Y_{nm}(\widehat{\boldsymbol{a}}_p) \times \sum_{p'=0}^{M_R} \sum_{q'=-p'}^{p'} e^{ip'\pi/2} j_{p'}(kb_q(t)) Y_{p'q'}^*(\widehat{\boldsymbol{b}}_q) \alpha_{n,m}^{p',q'}, \tag{3.17}$$

where $M_T \triangleq \lceil kea_p(t)/2 \rceil$ and $M_R \triangleq \lceil keb_q(t)/2 \rceil$.

As a special case in 3D scattering environment, we apply the fact that there is only one transmitter antenna and one receiver antenna in a SISO system to (3.17). Then the SISO channel for a 3D scattering environment can be derived as:

$$h^{\mathrm{SISO_{3D}}}(t) \cong (4\pi)^2 \sum_{n=0}^{M_T} \sum_{m=-n}^{n} e^{-in\pi/2} j_n(kut) Y_{nm}(\widehat{\boldsymbol{u}}) \times \sum_{p'=0}^{M_R} \sum_{q'=-p'}^{p'} e^{ip'\pi/2} j_{p'}(kvt) Y_{p'q'}^*(\widehat{\boldsymbol{v}}) \alpha_{n,m}^{p',q'}, \tag{3.18}$$

where $M_T \triangleq \lceil keut/2 \rceil$ and $M_R \triangleq \lceil kevt/2 \rceil$.

3.5 Multicarrier M2M Channel Model

In this section we are going to extend our single carrier M2M models presented in previous sections to a multicarrier M2M model. In single carrier, we formulated time varying channel model but in multicarrier, nth subcarrier channel frequency response is modeled.

As before, transmitter consists of n_T transmitting antennas located at positions $x_p, p = 1, 2, \ldots, n_T$ with respect to transmitter origin and also receiver consists of n_R receiving antennas located at positions $x_q, q = 1, 2, \ldots, n_R$ with respect to receiver origin.

When a broadband signal $s(t)$ is transmitted from transmitter origin O_t in direction $\widehat{\phi}$ and received signal at time t at the receiver origin O_r from direction

$\widehat{\varphi}$ can be written as:

$$y_{0_t,0_r}(t,\widehat{\phi},\widehat{\varphi}) = \int_{\tau} g(\widehat{\phi},\widehat{\varphi},\tau)s(t-\tau)\,d\tau, \tag{3.19}$$

where $g(\widehat{\phi},\widehat{\varphi},\tau)$ represents the effective random complex scattering gain function for a signal leaving the transmitter scatterer-free region at a direction $\widehat{\phi}$ (relative to the transmitter region origin) and entering the receiver scatterer-free region from a direction $\widehat{\varphi}$ (relative to the receiver region origin) with a channel delay of τ.

The transmit signal from the p^{th} transmit antenna located at $\boldsymbol{x}_p$ from the direction $\widehat{\phi}$ and received at the q^{th} receive antenna located at $\boldsymbol{x}_q$ in the the direction $\widehat{\varphi}$ can be written as:

$$y_{p,q}(t,\widehat{\phi},\widehat{\varphi},\boldsymbol{x}_p,\boldsymbol{x}_q) = \int_{\tau} g(\widehat{\phi},\widehat{\varphi},\tau)s(t-t_p-t_q-\tau)\,d\tau, \tag{3.20}$$

where $t_p = (\boldsymbol{u}\tau+\boldsymbol{x}_p)\cdot\widehat{\phi}/c$ and $t_q = (\boldsymbol{v}\tau+\boldsymbol{x}_q)\cdot\widehat{\varphi}/c$. The terms t_p and t_q are factors that take into account the position of p^{th} transmit antenna and the velocity of the transmitter and position of q^{th} receive antenna and the velocity of the receiver respectively and c represents the speed of wave propagation.

To further simplify (3.20), let $\boldsymbol{u}_p = \boldsymbol{u}\tau+\boldsymbol{x}_p$ and $\boldsymbol{u}_q = \boldsymbol{v}\tau+\boldsymbol{x}_q$, then $t_p = \boldsymbol{u}_p\cdot\widehat{\phi}/c$ and $t_q = \boldsymbol{u}_q\cdot\widehat{\varphi}/c$. Then the received signal at the q^{th} receive antenna from the p^{th} transmit antenna can be written as:

$$y_{p,q}(t,\boldsymbol{x}_p,\boldsymbol{x}_q) = \int_{\Omega_T}\int_{\Omega_R}\int_{\tau} g(\widehat{\phi},\widehat{\varphi},\tau)s(t-t_p-t_q-\tau)\,d\tau\,d\widehat{\varphi}\,d\widehat{\phi}. \tag{3.21}$$

By taking Fourier transform of (3.21) with respect to t yields

$$Y_{p,q}(\omega,\boldsymbol{x}_p,\boldsymbol{x}_q) = \int_{\Omega_T}\int_{\Omega_R}\int_{\tau} g(\widehat{\phi},\widehat{\varphi},\tau)S(\omega)e^{-i(t_p+t_q+\tau)\omega}\,d\tau\,d\widehat{\varphi}\,d\widehat{\phi}, \tag{3.22}$$

where $Y_{p,q}(\omega,\boldsymbol{x}_p,\boldsymbol{x}_q) = \mathcal{F}\{y_{p,q}(t,\boldsymbol{x}_p,\boldsymbol{x}_q)\}$ and $S(\omega) = \mathcal{F}\{s(t)\}$ are the Fourier transform of the received signal $y_{p,q}(t,\boldsymbol{x}_p,\boldsymbol{x}_q)$ and the transmitted signal $s(t)$, re-

spectively. We can write (3.22) as

$$Y_{p,q}(\omega, \boldsymbol{x}_p, \boldsymbol{x}_q) = H_{p,q}(\omega)S(\omega), \tag{3.23}$$

where the channel frequency response between the p^{th} transmit antenna and the q^{th} receive antenna can be obtained as

$$H_{p,q}(\omega) = \int_{\Omega_T}\int_{\Omega_R}\int_{\tau} g(\widehat{\boldsymbol{\phi}}, \widehat{\boldsymbol{\varphi}}, \tau)e^{-i\omega\tau}e^{-i(\omega/c)\boldsymbol{u}_p\cdot\widehat{\boldsymbol{\phi}}}e^{-i(\omega/c)\boldsymbol{u}_q\cdot\widehat{\boldsymbol{\varphi}}}\, d\tau\, d\widehat{\boldsymbol{\varphi}}\, d\widehat{\boldsymbol{\phi}}. \tag{3.24}$$

Assume f_c is the carrier frequency and there are N_s subcarriers with spacing Δf. The channel frequency response at the n^{th} subcarrier between the p^{th} transmit antenna located at $\boldsymbol{x}_p$ and the q^{th} receive antenna located at $\boldsymbol{x}_q$ can then be written as:

$$\begin{aligned} H_{p,q}(n) = &\int_{\Omega_T}\int_{\Omega_R}\int_{\tau} g(\widehat{\boldsymbol{\phi}}, \widehat{\boldsymbol{\varphi}}, \tau)e^{-i2\pi(f_c-(n+0.5)\Delta f)\tau} \\ &\times e^{-i(2\pi/c)(f_c-(n+0.5)\Delta f)\boldsymbol{u}_p\cdot\widehat{\boldsymbol{\phi}}}e^{-i(2\pi/c)(f_c-(n+0.5)\Delta f)\boldsymbol{u}_q\cdot\widehat{\boldsymbol{\varphi}}}\, d\tau\, d\widehat{\boldsymbol{\varphi}}\, d\widehat{\boldsymbol{\phi}}, \end{aligned} \tag{3.25}$$

The channel frequency response $H_{p,q}(n)$ captures the statistical properties of the frequency selective channel via the random complex scattering gain $g(\widehat{\boldsymbol{\phi}}, \widehat{\boldsymbol{\varphi}}, \tau)$ and physical configuration of the transmitter and receiver antenna array. The deterministic properties of the physical configuration is captured via the location of the p^{th} transmit antenna located at $\boldsymbol{x}_p$ and the q^{th} receive antenna located at $\boldsymbol{x}_q$. Through proper selection of $\boldsymbol{x}_p$ and $\boldsymbol{x}_q$, this channel model can be applied to any transmitter and receiver antenna configuration, that is, without constraining to a particular antenna configuration such as uniform linear array or uniform circular array.

Applying this multicarrier channel model to 2D and 3D scattering environments will be discussed in Chapter 5 with further analysis of multicarrier channel models.

3.6 Conclusions

In this chapter, we have extended the F2M channels proposed in [57] based on the underlying physics of free space wave propagation to M2M narrowband channel

models and simplified the expressions for 2D and 3D scattering environments. In addition, this model is further extended to derive a multicarrier M2M channel model.

When we compare our model with the other available models discussed in Chapter 2, we distill the principal advantages of our model:

Able to represent any scattering environment – In our model selecting suitable $g(\widehat{\phi}, \widehat{\varphi})$ represents the effective random complex scattering gain function. Therefore, it is suitable for any scattering environment even though other models only cater for a selected scattering environment such as one-ring, two-ring, etc.

Distance independent – Our model is independent with the distance parameters relevant to transmitter, receiver and scattering environment whereas the other models are distance dependent.

The correlation properties and second order statistics of the proposed channel models are discussed in the chapters to follow.

Chapter 4

Space-Time Correlation

4.1 Introduction

In this chapter we analyze the space-time correlation of received signals and channel temporal correlation related to the novel mobile to mobile (M2M) channel model which was introduced in Chapter 3 as a generalized M2M channel model.

Space-time correlation of received signals is the correlation between the two received signals at two different times while channel temporal correlation is the correlation between the same channel but at two different times. When comparing these correlations, space-time correlation of the received signals has an additional dependency on the distance of the two receivers and the input signals.

Many of the statistical properties of the complex envelope can be determined from its time correlation, for example, power spectrum can be obtained by Fourier transforming the time correlation of the complex envelope and also second order statistical properties like level crossing rate and average fade duration, which will be discussed in Chapter 6, can also be derived.

In the literature, [2] is the first paper to discuss M2M space-time correlation and time correlation. Its analysis was based on the ratio between v and u where v denotes the magnitude of receiver velocity and u is magnitude of the transmitter velocity. But in this chapter, we claim that the correlation depends on values of u and v not the ratio v/u.

Most of the M2M papers available in the literature [13, 22, 24, 25, 27–31, 35] dis-

cuss the relationship of space-time correlation and time correlation with time delay and distance between receiving points or related. As the relationship between the correlation and the properties such as velocity of transmitter, velocity of receiver, mean angle of arrival (AoA) and mean angle of departure (AoD) are not analyzed in detail in the literature, we address this gap in our analysis in this chapter.

Multiple antenna systems have been studied extensively in the recent past. Though multiple antenna systems have helped to achieve high bandwidth efficiencies in wireless communication systems, fourth generation mobile communications standards LTE (Long Term Evolution) and latest M2M communication systems discussed in Chapter 2 still largely depend on the further improvement of multiple antenna systems to deliver their future data rates. To further improve multiple antenna systems especially in M2M systems, one key challenge is to understand the characteristics of the underlying channel between transmitter and receiver antenna arrays, in particular, the effects of time correlation on the performance of multiple antenna communication systems. In this chapter we extend the space-time channel correlation model proposed in [57] to two dimensional (2D) M2M and three dimensional (3D) M2M scattering environments. Using our M2M channel model we also analyze the time correlation in 2D and 3D environments for different angular power distributions, representing the scatterer effect, when the transmitter and receiver are moving.

The remainder of this chapter is outlined as follows. The generalized space-time cross correlation function between two received signals is discussed in Section 4.2 while Section 4.3 describes basic channel temporal correlation function and applies to our new channel model discussed in Chapter 3. The space-time cross correlation and temporal correlation functions relevant to our M2M channel model are applied to 2D and 3D scattering environments in Section 4.4 and in Section 4.5 respectively. Finally, concluding remarks are drawn in Section 4.6.

4.2 Space-Time Cross Correlation

Consider a multiple input multiple output(MIMO) system with $n_{_T}$ transmit antennas located at positions s_p, $p = 1, 2, \ldots, p_1, \ldots, p_2, \ldots, n_T$ from a transmitter origin and n_R receiver antennas located at positions z_q, $q = 1, 2, \ldots, q_1, \ldots, q_2, \ldots, n_R$

from a receiver origin, within spheres of radius r_T and r_R, respectively.

Let $y_{p_1,q_1}(t)$ and $y_{p_2,q_2}(t)$ denote the received signals at two antennas located on the receiver at points $\boldsymbol{z}_{q_1}$ and $\boldsymbol{z}_{q_2}$ from the transmitter with antennas located at points $\boldsymbol{s}_{p_1}$ and $\boldsymbol{s}_{p_2}$, respectively. Then the space-time cross correlation function between the complex envelopes of $y_{p_1,q_1}(t)$ and $y_{p_2,q_2}(t)$ is defined by [57]

$$\Phi_{st}(\tau) = E\left\{y_{p_1,q_1}(t)y^*_{p_2,q_2}(t-\tau)\right\}. \tag{4.1}$$

The transmitted signal is a narrowband monochromatic plane wave e^{iw_ct}, where w_c is the angular carrier frequency of the signal. The narrowband received signal on the q^{th} receiver at point $\boldsymbol{z}_q$ from p^{th} transmitter at point $\boldsymbol{s}_p$ can be written as

$$\begin{aligned} y_{p,q}(t) &= \iint_{\mathbb{S}^n\times\mathbb{S}^n} g(\widehat{\boldsymbol{\phi}},\widehat{\boldsymbol{\varphi}})e^{i(w_c+w_{d_t}(\widehat{\boldsymbol{\phi}})+w_{d_r}(\widehat{\boldsymbol{\varphi}}))t}e^{-ik\boldsymbol{s}_p\cdot\widehat{\boldsymbol{\phi}}}e^{-ik\boldsymbol{z}_q\cdot\widehat{\boldsymbol{\varphi}}}\,d\widehat{\boldsymbol{\phi}}\,d\widehat{\boldsymbol{\varphi}} \\ &= e^{iw_ct}\iint_{\mathbb{S}^n\times\mathbb{S}^n} g(\widehat{\boldsymbol{\phi}},\widehat{\boldsymbol{\varphi}})e^{-ik\boldsymbol{u}_p(t)\cdot\widehat{\boldsymbol{\phi}}}e^{-ik\boldsymbol{v}_q(t)\cdot\widehat{\boldsymbol{\phi}}}\,d\widehat{\boldsymbol{\phi}}\,d\widehat{\boldsymbol{\varphi}}, \end{aligned} \tag{4.2}$$

where $\mathbb{S}^n$ is the n-sphere, $k = 2\pi/\lambda$ is the wave number with λ being the wavelength, $w_{d_t}(\widehat{\boldsymbol{\phi}}) = \frac{2\pi}{\lambda}u\widehat{\boldsymbol{u}}\cdot\widehat{\boldsymbol{\phi}}$ and $w_{d_r}(\widehat{\boldsymbol{\varphi}}) = \frac{2\pi}{\lambda}v\widehat{\boldsymbol{v}}\cdot\widehat{\boldsymbol{\varphi}}$ are angular Doppler spread due to transmitter and receiver motion, respectively. Suppose the transmitter is moving at a constant velocity magnitude u in the direction of unit vector $\widehat{\boldsymbol{u}}$ and the receiver is moving at a constant velocity magnitude v in the direction of unit vector $\widehat{\boldsymbol{v}}$. Thereby

$$\boldsymbol{u}_p(t) = \boldsymbol{s}_p - tu\widehat{\boldsymbol{u}}, \tag{4.3}$$

is the position of the p^{th} transmitter antenna at time t and

$$\boldsymbol{v}_q(t) = \boldsymbol{z}_q - tv\widehat{\boldsymbol{v}}, \tag{4.4}$$

is the position of the q^{th} receiver antenna at time t.

The integration in (4.2) above is over the cartesian product of the unit circle with itself for a 2D multipath (or scattering) environment ($n = 1$) or over the cartesian product of the unit sphere with itself for a 3D scattering environment

$(n = 2)$.

Assuming a wide sense stationary zero mean uncorrelated scattering environment, the second order statistics of the scattering gain function $g(\widehat{\boldsymbol{\phi}}, \widehat{\boldsymbol{\varphi}})$ can be defined as [60]

$$E\left\{g(\widehat{\boldsymbol{\phi}}, \widehat{\boldsymbol{\varphi}})g^*(\widehat{\boldsymbol{\phi}}', \widehat{\boldsymbol{\varphi}}')\right\} \triangleq G(\widehat{\boldsymbol{\phi}}, \widehat{\boldsymbol{\varphi}})\delta(\widehat{\boldsymbol{\phi}} - \widehat{\boldsymbol{\phi}}')\delta(\widehat{\boldsymbol{\varphi}} - \widehat{\boldsymbol{\varphi}}'), \tag{4.5}$$

where $G(\widehat{\boldsymbol{\phi}}, \widehat{\boldsymbol{\varphi}}) = E\left\{|g(\widehat{\boldsymbol{\phi}}, \widehat{\boldsymbol{\varphi}})|^2\right\}$ characterizes the joint power spectral density (PSD) or the joint angular power distribution surrounding the transmitter and receiver regions.

Using (4.1), (4.2) and (4.5), we simplify space-time cross correlation function between two received signals,

$$\Phi_{st}(\tau) = e^{iw_c\tau} \iint_{\mathbb{S}^n \times \mathbb{S}^n} G(\widehat{\boldsymbol{\phi}}, \widehat{\boldsymbol{\varphi}}) e^{-ik\boldsymbol{u}_{st}(\tau)\cdot\widehat{\boldsymbol{\phi}}} e^{ik\boldsymbol{v}_{st}(\tau)\cdot\widehat{\boldsymbol{\varphi}}} d\widehat{\boldsymbol{\phi}} d\widehat{\boldsymbol{\varphi}}. \tag{4.6}$$

where

$$\boldsymbol{u}_{st}(\tau) = \boldsymbol{u}_{p_2}(t-\tau) - \boldsymbol{u}_{p_1}(t) = \boldsymbol{s}_{p_2} - \boldsymbol{s}_{p_1} + \tau\boldsymbol{u}, \tag{4.7}$$

and

$$\boldsymbol{v}_{st}(\tau) = \boldsymbol{v}_{q_2}(t-\tau) - \boldsymbol{v}_{q_1}(t) = \boldsymbol{z}_{q_2} - \boldsymbol{z}_{q_1} + \tau\boldsymbol{v}. \tag{4.8}$$

The generalized space-time cross correlation function between two received signals in (4.6) will be applied to the 2D isotropic scattering environment in Section 4.4, and 3D isotropic scattering environment in Section 4.5.

4.3 Channel Temporal Correlation

The channel temporal correlation, which is the correlation between the channel gain at time t and time $t - \tau$ can be found from

$$\Phi(\tau) \triangleq E\left\{h(t)h^*(t-\tau)\right\}. \tag{4.9}$$

Using (3.5) and (4.9), the temporal correlation for M2M channel model can be written as:

$$\Phi(\tau) = \int_4 E\left\{g(\widehat{\boldsymbol{\phi}}, \widehat{\boldsymbol{\varphi}}) g^*(\widehat{\boldsymbol{\phi}}', \widehat{\boldsymbol{\varphi}}')\right\} e^{iku(-t\widehat{\boldsymbol{u}}\cdot\widehat{\boldsymbol{\phi}}+(t-\tau)\widehat{\boldsymbol{u}}\cdot\widehat{\boldsymbol{\phi}}')} \times e^{-ikv(-t\widehat{\boldsymbol{v}}\cdot\widehat{\boldsymbol{\varphi}}+(t-\tau)\widehat{\boldsymbol{v}}\cdot\widehat{\boldsymbol{\varphi}}')}\, d\widehat{\boldsymbol{\phi}}\, d\widehat{\boldsymbol{\varphi}}\, d\widehat{\boldsymbol{\phi}}'\, d\widehat{\boldsymbol{\varphi}}', \tag{4.10}$$

where we have introduced the shorthand $\int_4 \triangleq \iint_{\mathbb{S}^n\times\mathbb{S}^n} \iint_{\mathbb{S}^n\times\mathbb{S}^n}$.

Using (4.5), the temporal correlation function in (4.10) can be further simplified to

$$\Phi(\tau) = \iint_{\mathbb{S}^n\times\mathbb{S}^n} G(\widehat{\boldsymbol{\phi}}, \widehat{\boldsymbol{\varphi}}) e^{-iku\tau\widehat{\boldsymbol{u}}\cdot\widehat{\boldsymbol{\phi}}} e^{ikv\tau\widehat{\boldsymbol{v}}\cdot\widehat{\boldsymbol{\varphi}}}\, d\widehat{\boldsymbol{\phi}}\, d\widehat{\boldsymbol{\varphi}}. \tag{4.11}$$

From the equation above it can be seen that the temporal correlation of a M2M fading channel is described largely by the joint angular power distribution $G(\widehat{\boldsymbol{\phi}}, \widehat{\boldsymbol{\varphi}})$ and the velocities of transmitter and receiver. The generalized space-time cross correlation function in (4.6) and the temporal correlation function in (4.11) will be applied to the 2D scattering environment in the next section.

4.4 2D Scattering Environment

Consider when the multipath is restricted to the azimuth plane only (2D scattering environment), having no field components arriving at significant elevations. The modal expansion (also known as the Jacobi-Anger expansion) of plane wave $e^{ik\boldsymbol{x}.\widehat{\boldsymbol{\phi}}}$ is given by [58, page 67]

$$e^{ik\boldsymbol{x}.\widehat{\boldsymbol{\phi}}} = \sum_{n=-\infty}^{\infty} J_n(k\|\boldsymbol{x}\|) e^{in(\phi_x+\pi/2-\phi)}, \tag{4.12}$$

where $\boldsymbol{x} \equiv (\|\boldsymbol{x}\|, \phi_x)$, $\widehat{\boldsymbol{\phi}} \equiv (1, \phi)$ are in the polar coordinates system and $J_n(\cdot)$ are the Bessel functions of the first kind.

Application of (4.12) in (4.11) yields

$$\Phi(\tau) = \sum_{m=-\infty}^{\infty} \sum_{n=-\infty}^{\infty} \beta_m^n J_m(ku\tau) J_n(kv\tau) e^{-im(\phi_u+\pi/2)} e^{in(\phi_v+\pi/2)}, \tag{4.13}$$

where $\widehat{\boldsymbol{u}} \equiv (1, \phi_u)$, $\widehat{\boldsymbol{v}} \equiv (1, \phi_v)$, $\widehat{\boldsymbol{\phi}} \equiv (1, \phi)$, $\widehat{\boldsymbol{\varphi}} \equiv (1, \varphi)$ are in the polar coordinates system and coefficients β_m^n characterize the 2D scattering environment surrounding the transmitter and receiver regions and are given by

$$\beta_m^n = \iint_{\mathbb{S}^1 \times \mathbb{S}^1} G(\widehat{\boldsymbol{\phi}}, \widehat{\boldsymbol{\varphi}}) e^{-in\varphi} e^{im\phi} \, d\widehat{\boldsymbol{\varphi}} \, d\widehat{\boldsymbol{\phi}}. \tag{4.14}$$

Since the scattering gain function $g(\widehat{\boldsymbol{\phi}}, \widehat{\boldsymbol{\varphi}})$ is periodic in both $\widehat{\boldsymbol{\phi}}$ and $\widehat{\boldsymbol{\varphi}}$, the joint PSD $G(\widehat{\boldsymbol{\phi}}, \widehat{\boldsymbol{\varphi}})$ is also periodic in both $\widehat{\boldsymbol{\phi}}$ and $\widehat{\boldsymbol{\varphi}}$. Therefore, using the orthogonal circular harmonics as the basis set, $G(\widehat{\boldsymbol{\phi}}, \widehat{\boldsymbol{\varphi}})$ can be expanded in a 2D Fourier series as:

$$G(\widehat{\boldsymbol{\phi}}, \widehat{\boldsymbol{\varphi}}) = \frac{1}{4\pi^2} \sum_{m=-\infty}^{\infty} \sum_{n=-\infty}^{\infty} \beta_m^n e^{-im\phi} e^{in\varphi}. \tag{4.15}$$

Note that (4.14) and (4.15) form a Fourier transform pair. Also note that scattering coefficients β_m^n are independent of the transmitter and receiver velocities. Hence the β_m^n are invariant to Doppler effects and are fixed for a given scattering distribution type.

Note that Bessel function $J_m(\cdot)$ for $|m| > 0$ exhibits a spatially high-pass character. Therefore, as shown in [59], $J_m(kr) \approx 0$ for $|m| > ker/2$, where $e = 2.71828\ldots$. Using this characteristic of Bessel functions we can truncate the infinite series in (4.13) to obtain

$$\Phi(\tau) \cong \sum_{m=-M_T}^{M_T} \sum_{n=-M_R}^{M_R} \beta_m^n J_m(ku\tau) J_n(kv\tau) e^{-im(\phi_u+\pi/2)} e^{in(\phi_v+\pi/2)}, \tag{4.16}$$

where $M_T = keu/2$ and $M_R = kev/2$.

We apply temporal correlation and space-time correlation to three classes of scattering models, namely

1. isotropic scattering,

2. non-isotropic scattering: separable and

3. non-isotropic scattering: nonseparable.

4.4.1 Isotropic Scattering Environment

Using (4.13) we now recover the classical time correlation result given in [2] for isotropic scattering environments, i.e., $G(\widehat{\boldsymbol{\phi}}, \widehat{\boldsymbol{\varphi}}) = 1/4\pi^2$. In this case

$$\beta_m^n = \begin{cases} 1, & m = n = 0 \\ 0, & \text{otherwise} \end{cases}$$

and the temporal correlation function of the M2M channel becomes

$$\Phi(\tau) = J_0(ku\tau)J_0(kv\tau). \tag{4.17}$$

Similarly, the space-time cross correlation function between two received signals is

$$\Phi_{st}(\tau) = e^{iw_c\tau} J_0(k\boldsymbol{u}_{st}(\tau))J_0(k\boldsymbol{v}_{st}(\tau)). \tag{4.18}$$

4.4.2 Non-Isotropic Scattering: Separable Channels

When the effects of the AoD, $\widehat{\boldsymbol{\phi}}$ are independent of the effects of the AoA, $\widehat{\boldsymbol{\varphi}}$, the joint angular power distribution $G(\widehat{\boldsymbol{\phi}}, \widehat{\boldsymbol{\varphi}})$ can be written as

$$G(\widehat{\boldsymbol{\phi}}, \widehat{\boldsymbol{\varphi}}) = G_{Tx}(\widehat{\boldsymbol{\phi}})G_{Rx}(\widehat{\boldsymbol{\varphi}}), \tag{4.19}$$

where $G_{Tx}(\widehat{\boldsymbol{\phi}}) = \int G(\widehat{\boldsymbol{\phi}}, \widehat{\boldsymbol{\varphi}})d\widehat{\boldsymbol{\varphi}}$ is the angular power distribution at the transmitter and $G_{Rx}(\widehat{\boldsymbol{\varphi}}) = \int G(\widehat{\boldsymbol{\phi}}, \widehat{\boldsymbol{\varphi}})d\widehat{\boldsymbol{\phi}}$ is the angular power distribution at the receiver. Fading channels that satisfy (4.19) are known as separable channels or Kronecker channels. As shown in [60], the separability condition (4.19) can be assumed when there is a single scattering cluster in the scattering environment.

In this case the scattering environment coefficients are given by

$$\beta_m^n = \beta_m^0 \beta_0^n, \tag{4.20}$$

where

$$\beta_m^0 = \int_{\mathbb{S}^1} G_{Tx}(\phi) e^{im\phi} d\phi \quad \text{and} \quad \beta_0^n = \int_{\mathbb{S}^1} G_{Rx}(\varphi) e^{-in\varphi} d\varphi.$$

A number of univariate azimuthal power distributions have been proposed in the literature for modeling the non-isotropic scattering distributions $G_{Tx}(\phi)$ and $G_{Rx}(\varphi)$ at the transmitter and the receiver, respectively. Few examples of them are uniform limited [61], truncated Gaussian [62], truncated Laplacian [63], cosine [61] and von-Mises [64]. These azimuthal power distributions are mainly characterized by the mean angle of arrival φ_0 (or departure ϕ_0) and the angular spread σ at the receiver (or transmitter). In the work on receiver correlation modelling for stationary multiple antennas, [65] has derived β_0^n in closed form for these common azimuthal power distributions. To illustrate the strength of the M2M channel model, we consider truncated Gaussian and von-Mises azimuthal power distributions as examples.

Truncated Gaussian Distribution – In this case the distribution is given by

$$G(\theta) = \frac{1}{\sqrt{2\pi}\sigma \operatorname{erf}(\pi/\sqrt{2}\sigma)} e^{-\frac{(\theta-\theta_0)^2}{2\sigma^2}}, \quad |\theta - \theta_0| \leq \pi \tag{4.21}$$

where θ_0 is the mean AoA at the receiver (or the mean AoD at the transmitter), σ is the angular spread of the distribution and $\operatorname{erf}(x) = \frac{2}{\sqrt{\pi}} \int_0^x e^{-z^2} dz$. In this case the scattering coefficients at the receiver and the transmitter are well approximated by

$$\beta_0^n \approx e^{-(n^2\sigma_R^2/2 + in\varphi_0)} \quad \text{and} \quad \beta_m^0 \approx e^{-(m^2\sigma_T^2/2 - im\phi_0)},$$

where σ_R^2 and σ_T^2 are the angular spread at the receiver and the transmitter, respectively and φ_0 and ϕ_0 are the mean AoA and the mean AoD at the receiver and the transmitter, respectively.

von-Mises distribution – In this case the distribution is given by

$$G(\theta) = \frac{1}{2\pi I_0(\kappa)} e^{\kappa \cos(\theta - \theta_0)}, \quad |\theta - \theta_0| \leq \pi, \tag{4.22}$$

where $\kappa \geq 0$ represents the non isotropy factor of the distribution and $I_m(\cdot)$ is the modified Bessel function of the first kind. Note that, $\kappa = 0$ represents isotropic scattering. The scattering coefficients β_m^0 and β_0^n are given by

$$\beta_0^n = e^{-in\varphi_0} \frac{I_{-n}(\kappa_R)}{I_0(\kappa_R)} \quad \text{and} \quad \beta_m^0 = e^{im\phi_0} \frac{I_m(\kappa_T)}{I_0(\kappa_T)},$$

where κ_R and κ_T are the non isotropy factors at the receiver and transmitter regions, respectively.

4.4.3 Non-Isotropic Scattering: Nonseparable Channels

Statistical dependence between the effects as a function of transmit and receive angles leads to nonseparable channels. In [60] authors used covariance $\gamma = \text{cov}(\varphi, \phi)$ between transmit and receive angles to capture this statistical interdependency and introduced several bivariate angular power distributions to model the scattering channel. We will consider two examples of bivariate angular distributions and provide their scattering coefficients β_m^n.

Truncated Gaussian Bivariate Distribution – The power distribution in this case is given by

$$G(\phi, \varphi) = \Omega_G \exp\left[\frac{-Q(\phi, \varphi)}{2(1-\gamma^2)}\right], \quad \phi, \varphi \in [-\pi, \pi), \tag{4.23}$$

where Ω_G is a normalization constant such that $\int\int_{\mathbf{S}^1 \times \mathbf{S}^1} G(\varphi, \phi) d\varphi d\phi = 1$ and

$$Q(\phi, \varphi) = \frac{(\phi - \phi_0)^2}{\sigma_T^2} - \frac{2\gamma(\phi - \phi_0)(\varphi - \varphi_0)}{\sigma_T \sigma_R} + \frac{(\varphi - \varphi_0)^2}{\sigma_R^2},$$

where ϕ_0 is the mean AoD at the transmitter, σ_T is the standard deviation of the non truncated marginalized PSD at the transmitter, φ_0 is the mean AoA at the receiver and σ_R is the standard deviation of the non truncated

marginalized PSD at the receiver. The approximated β_m^n can be written as [60]

$$\beta_m^n \approx \exp(i(m\phi_0 - n\varphi_0) - \frac{1}{2}(\sigma_T^2 m^2 - 2\gamma\sigma_T\sigma_R mn + \sigma_R^2 n^2)).$$

Truncated Laplacian Bivariate Distribution – The power distribution in this case is given by

$$G(\phi,\varphi) = \Omega_L K_0\left(\sqrt{\frac{2Q(\phi,\varphi)}{1-\gamma^2}}\right), \quad \phi,\varphi \in [-\pi,\pi) \tag{4.24}$$

where Ω_L is a normalization constant such that $\int\int_{\mathbf{S}^1\times\mathbf{S}^1} G(\varphi,\phi)d\varphi d\phi = 1$, $Q(\phi,\varphi)$ is equivalent to the above Gaussian case and $K_0(\cdot)$ is the modified zero order Bessel function of the second kind. The approximated scattering coefficients β_m^n are given by [60],

$$\beta_m^n \approx \frac{\exp(im\phi_0 - in\varphi_0)}{\sigma_T^2 m^2 - 2\gamma\sigma_T\sigma_R mn + \sigma_R^2 n^2 + 1}.$$

4.4.4 Simulation Examples

In this subsection first we study the behavior of the space-time cross correlation of received signals only in the 2D isotropic M2M environment, and, secondly, the channel temporal correlation function under different 2D scattering environments. For all the simulations we select the carrier frequency as 5.9 GHz, which is reserved for M2M in IEEE 802.11p standards, for channel temporal correlation for a ten symbol period delay and 0.0001s as a symbol duration.

2D Isotropic Scattering Environment

We discuss space-time cross correlation under the 2D isotropic scattering environment while channel temporal correlation is discussed under different 2D scattering environments.

Fig. 4.1 and Fig. 4.2 show magnitude of space-time correlation vs normalized receiver distance and time delay for two different velocities of transmitter and

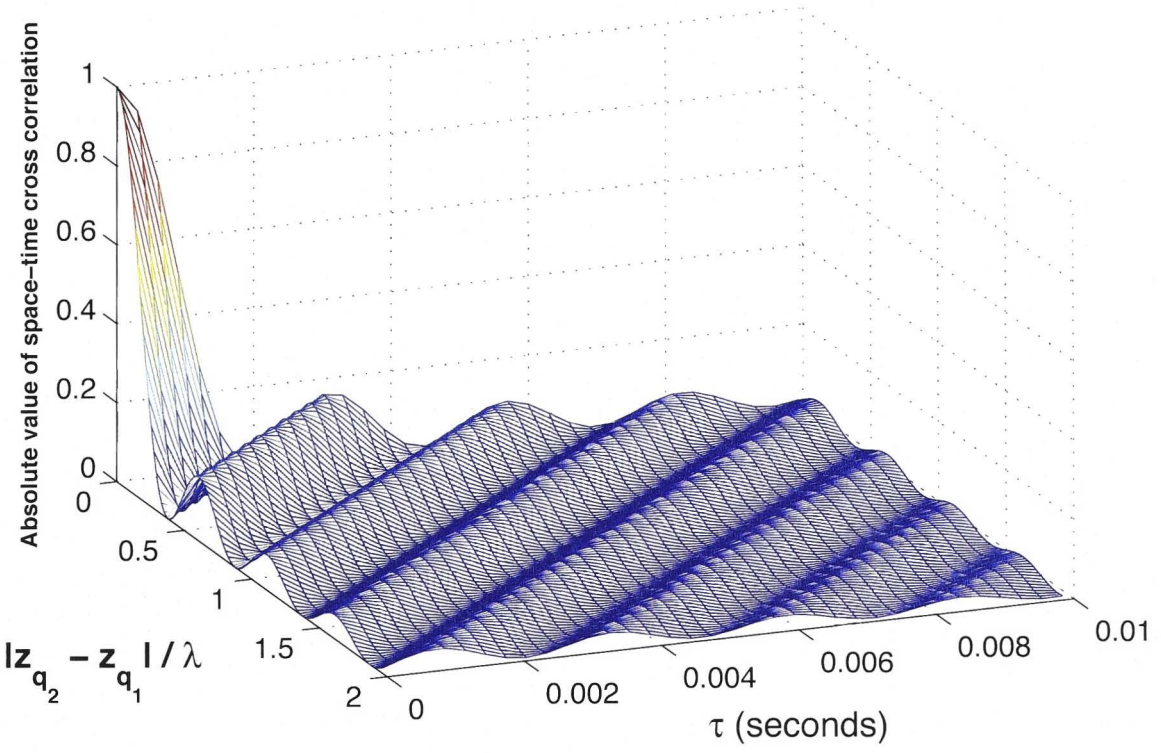

Figure 4.1: Space-time correlation between two received signals in 2D isotropic M2M environment when both transmitter and receiver are moving at 36 km/h.

receiver in 2D isotropic M2M environments. In both cases receiver and transmitter velocities are same. In [2], the ratio of velocities, defined as a ($a = v/u$) is equal to 1 in both simulations. But the above simulation results show that when the velocity is higher then change rate is higher, related to time delay axis. Note also that when time delay is zero, the correlation is equal for both simulations.

von-Mises Univariate Distributions

The contour plots of magnitude of the channel temporal correlation after 10 symbol period versus magnitude of transmitter velocity (u km/h) and magnitude of receiver velocity (v km/h) are shown in Fig. 4.3. In this simulation we use transmitter moving direction, $\phi_u = 0$ and receiver moving direction, $\phi_v = 0$. We plot three different graphs namely:

(a) Isotropic scattering distributions at both sides,

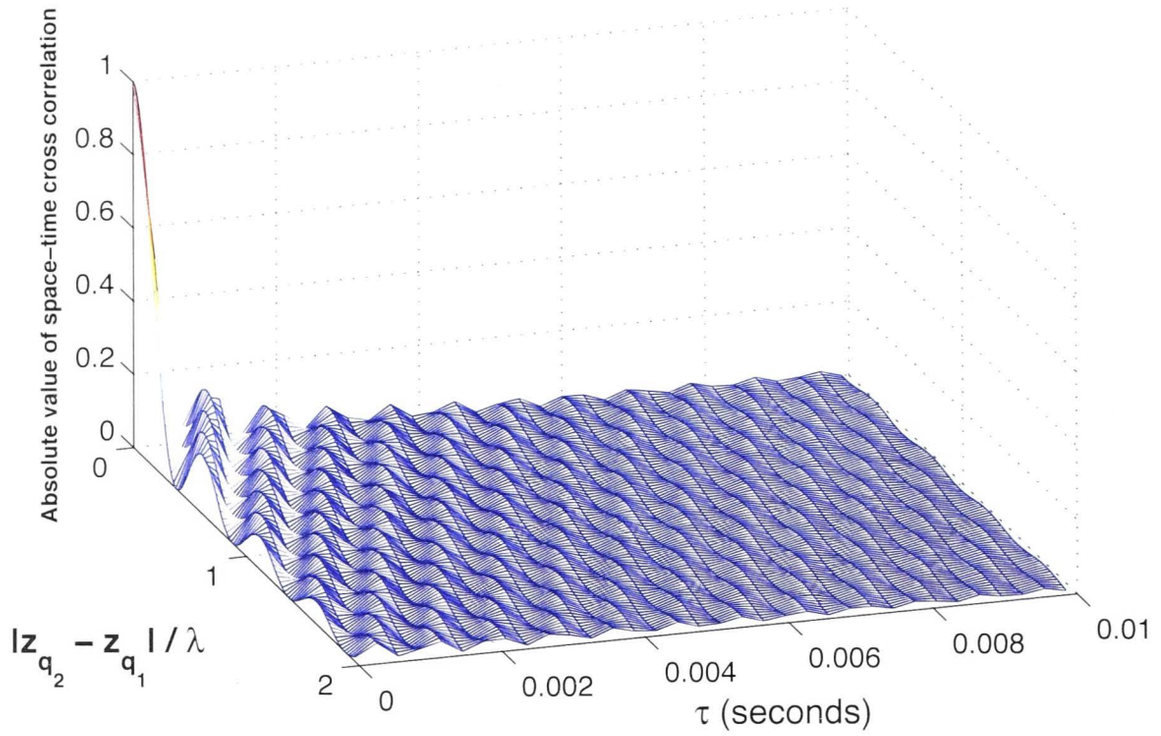

Figure 4.2: Space-time correlation between two received signals in 2D isotropic M2M environment when both transmitter and receiver are moving at 108 km/h.

(b) Receiver side – isotropic and transmitter side – von-Mises scattering with mean AoD $\phi_0 = 30^0$ and $\kappa_T = 10$, and

(c) Receiver side – isotropic and transmitter side – von-Mises scattering with mean AoD $\phi_0 = 0^0$ and $\kappa_T = 10$.

Simulation results of case (a) shows that when the scattering is isotropic in both receiver and transmitter sides, the time correlation is high (correlation > 0.3) until both transmitter and receiver reach velocities of 45 km/h. In addition, different moving directions of transmitter or receiver has no impact on correlation. According to the results shown in Fig. 4.3 (b) and (c) when the receiver side is isotropic and the transmitter side scattering is von-Mises distributed, the receiver can move much faster than the transmitter to achieve same correlation figure.

Next we analyze the relationship between κ_T and mean AoD in Fig. 4.4. The figure shows the contour plot of magnitude of the channel temporal correlation after 10 symbol period in: (a) both sides isotropic scattering distributions, (b)

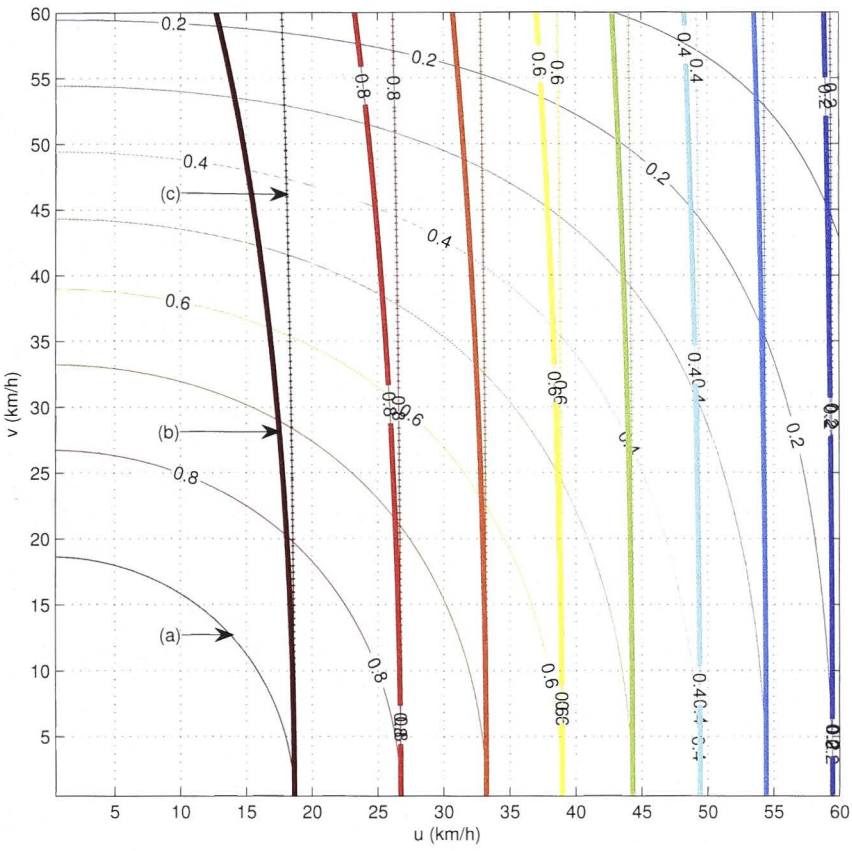

Figure 4.3: The channel temporal correlation after $\tau = 10$ symbol time period in 2D M2M environment. (a) Both transmitter and receiver sides isotropic scattering. (b) Receiver side – isotropic and transmitter side – von-Mises scattering with mean AoD $\phi_0 = 30^0$ and $\kappa_T = 10$ (c) Receiver side – isotropic and transmitter side – von-Mises scattering with mean AoD $\phi_0 = 0^0$ and $\kappa_T = 10$.

receiver side – isotropic and transmitter side – von-Mises scattering distributions with mean AoD $\phi_0 = 30^0$ and $\kappa_T = 100$ and (c) receiver side – isotropic and transmitter side – von-Mises scattering distributions with mean AoD $\phi_0 = 0^0$ and $\kappa_T = 100$ versus transmitter velocity (u km/h) and receiver velocity (v km/h). The angle of direction is zero for both transmitter and receiver movements. Simulation results show that when the receiver side is isotropic and the transmitter side has von-Mises scattering distribution, the time correlation is independent of mean AoD ϕ_0 for higher value of κ_T.

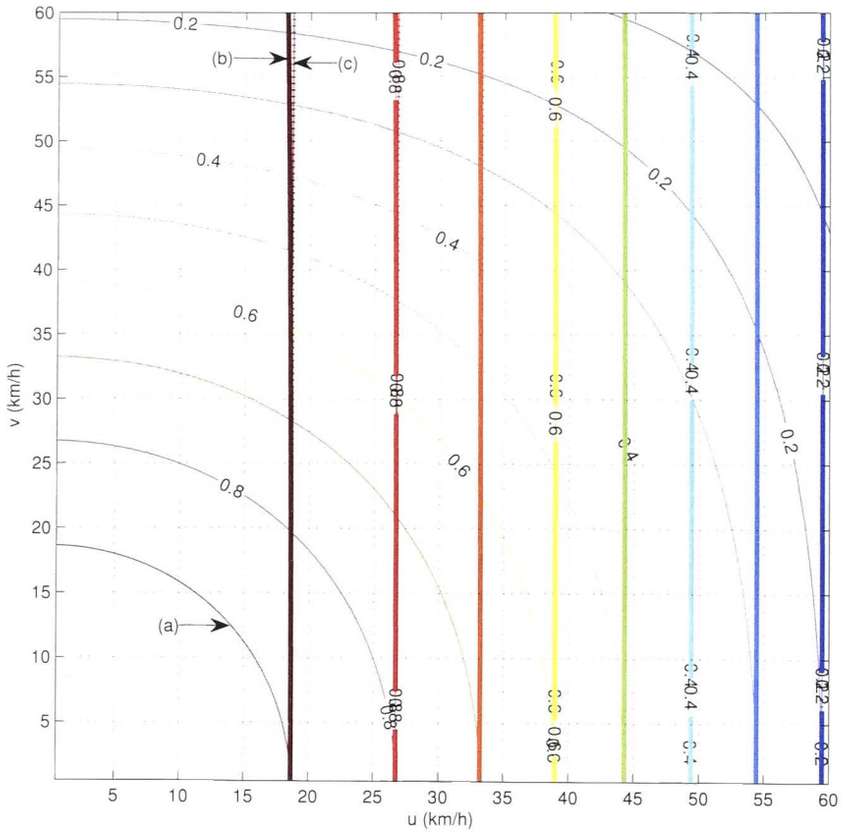

Figure 4.4: The channel temporal correlation after $\tau = 10$ symbol time period in 2D M2M environment. (a) Both transmitter and receiver sides isotropic scattering. (b) Receiver side – isotropic and transmitter side – von-Mises scattering with mean AoD $\phi_0 = 30^0$ and $\kappa_T = 100$. (c) Receiver side – isotropic and transmitter side – von-Mises scattering with mean AoD $\phi_0 = 0^0$ and $\kappa_T = 100$.

When analysing the impact of different transmitter and receiver directions and mean angle of arrival and departure, both showed similar behavioral relationships with temporal correlation. Because of this similar behavior, here we present only the impact of mean angle of arrival and departure in Fig. 4.5. The figure shows the contour plots of magnitude of the channel temporal correlation signals after 10 symbol period versus mean AoA and mean AoD in: (a) transmitter and receiver velocities equal to 20 km/h and (b) transmitter and receiver velocities equal to 50 km/h. Simulation results show that highest correlation occurs when mean AoA and mean AoD are multiples of 180^0 including 0^0 and 180^0 (e.g., $(0^0,0^0)$, $(0^0,180^0)$,

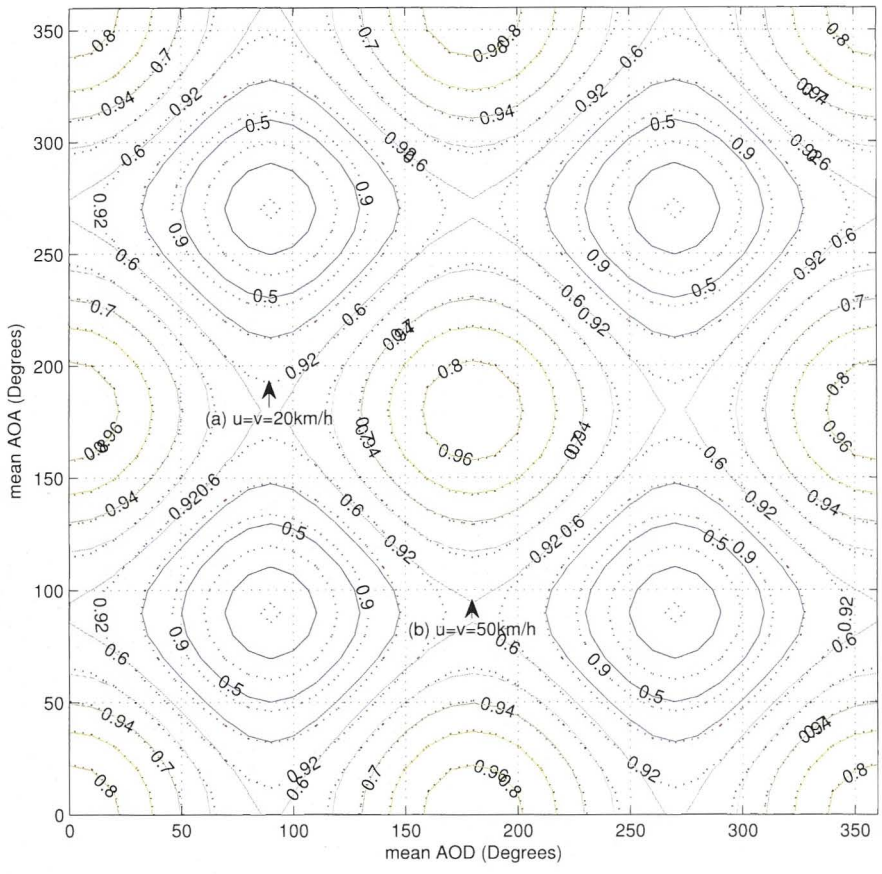

Figure 4.5: The channel temporal correlation after $\tau = 10$ symbol time period in 2D M2M environment and both sides von-Mises scattering distributions with $\kappa_R = \kappa_T = 3$. (a) Transmitter and receiver velocities equal to 20 km/h. (b) Transmitter and receiver velocities equal to 50 km/h

etc., are highest correlation points). In addition, the lowest correlation point occurs when mean AoA and mean AoD are equivalent to 90^0, 270^0, 450^0, ..., (e.g., (90^0, 90^0)). Also the figure shows that the correlation is higher when both transmitter and receiver are traveling at lower velocities keeping other factors unchanged.

The analysis of the impact of correlation when transmitter and receiver are moving at different velocities is shown in Fig. 4.6. The figure shows the contour plots of magnitude of the channel temporal correlation after 10 symbol period versus mean AoA and mean AoD in: (a) transmitter and receiver velocities equal to 20 km/h and 50 km/h; and (b) transmitter and receiver velocities equal to 50 km/h and 20 km/h. These results also confirm that the highest correlation

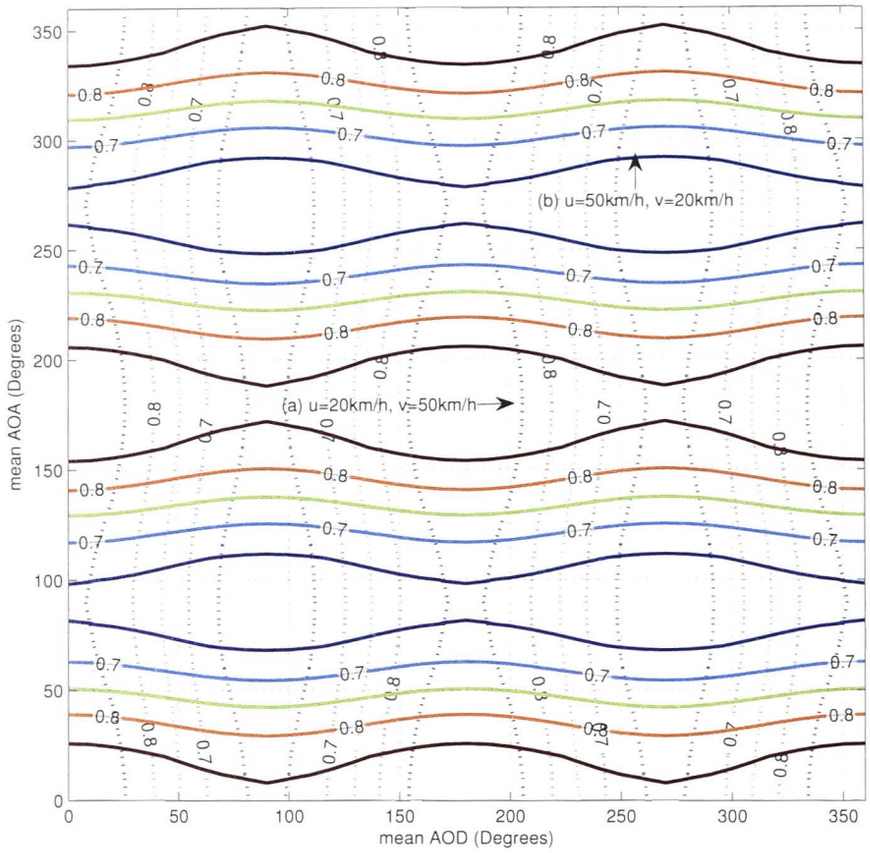

Figure 4.6: The channel temporal correlation after $\tau = 10$ symbol time period in 2D M2M environment and both sides von-Mises scattering with $\kappa_R = \kappa_T = 3$. (a) Transmitter and receiver velocities equal to 20 km/h and 50 km/h (b) Transmitter and receiver velocities equal to 50 km/h and 20 km/h

occurs when mean AoA and mean AoD are multiples of 180^0 including 0^0 and 180^0 (e.g., $(0^0,0^0)$, $(0^0,180^0)$, etc., are the highest correlation points), and the lowest correlation points occur when mean AoA and mean AoD are equivalent to 90^0, 270^0, 450^0, ..., (e.g., $(90^0, 90^0)$).

Truncated Gaussian Bivariate Distribution

We have selected truncated Gaussian bivariate distribution to analyze the relationship between bivariate distribution and channel temporal correlation. Example graphs used for the analysis are shown in Fig. 4.7 and Fig. 4.8. For the bivariate

distribution, $\gamma = cov(u, v)$ represents the statistical interdependency as a function of transmit and receive angles. Theoretically in separable situation, when $\gamma = 0$, it should be equivalent to two truncated Gaussian univariate distributions, which is confirmed by our results.

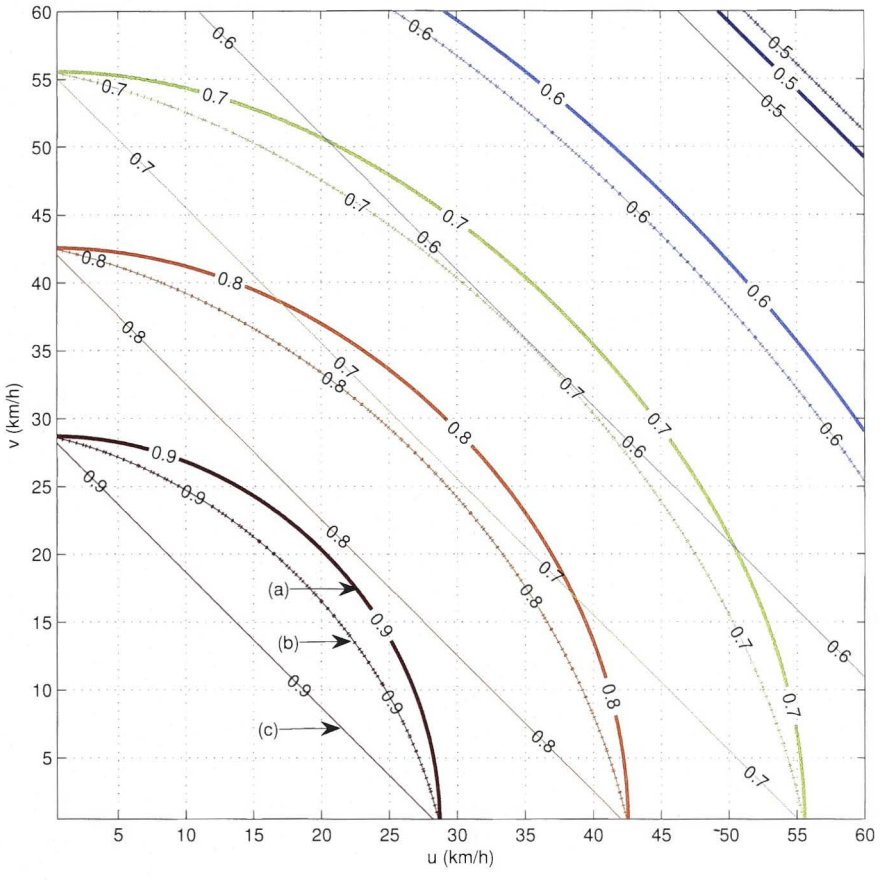

Figure 4.7: The channel temporal correlation after $\tau = 10$ symbol time period in 2D M2M environment with mean $AoD = 0^0$, mean $AoA = 180^0$ and $\sigma_t = \sigma_r = 60^0$. (a) Truncated Gaussian bivariate distribution with $\gamma = 0$. (b) Truncated Gaussian bivariate distribution with $\gamma = 0.5$. (c) Truncated Gaussian bivariate distribution with $\gamma = 1$.

4.5 3D Scattering Environment

In this section, based on our M2M channel model we derive the temporal correlation function for a general 3D scattering environment. The temporal correlation

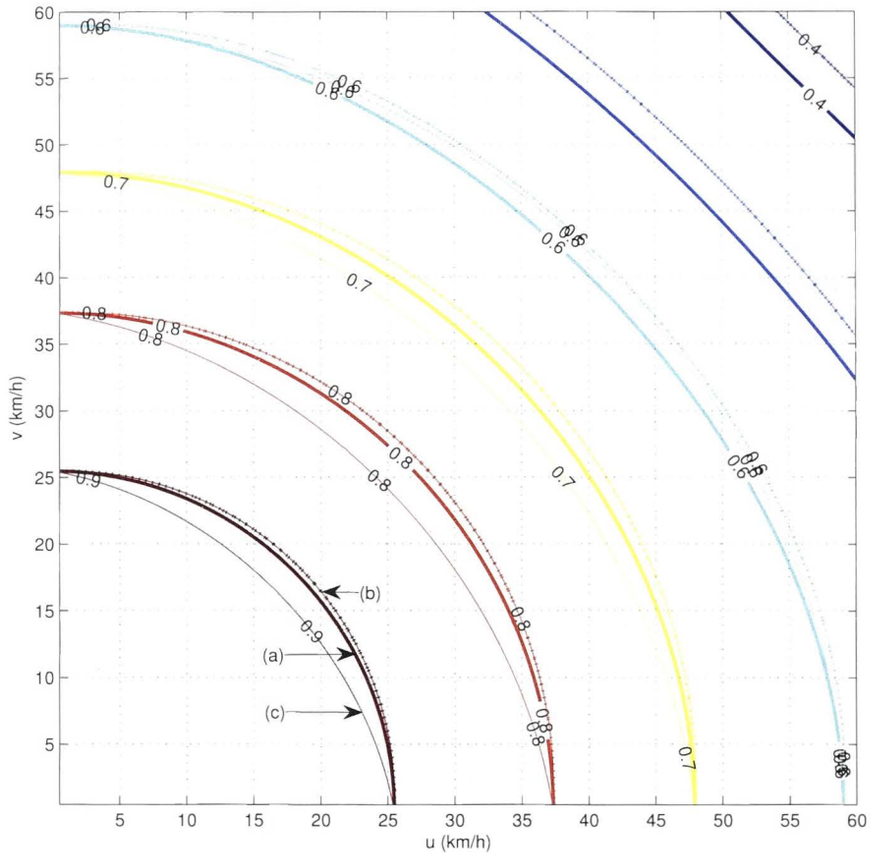

Figure 4.8: The channel temporal correlation after $\tau = 10$ symbol time period in 2D M2M environment with mean $AoD = 30^0$, mean $AoA = 150^0$ and $\sigma_t = \sigma_r = 60^0$ (a)Truncated Gaussian bivariate distribution with $\gamma = 0$ (b) Truncated Gaussian bivariate distribution with $\gamma = 0.5$ (c) Truncated Gaussian bivariate distribution with $\gamma = 1$

function is characterized by the joint angular power distribution at the transmitter and receiver antennas and the velocities of transmitter and receiver antennas. As a special case, in this section we consider separable scattering environments, i.e., the angular power distribution at the receiver is independent of that at the transmitter. In this case, using the von Mises-Fisher distribution as an example for the angular power distribution at each end of the channel, we calculate the temporal correlation function for several fading scenarios and discuss the usefulness of it.

Using the spherical harmonic expansion of plane waves, the plane wave $e^{ik\boldsymbol{x}\cdot\widehat{\boldsymbol{y}}}$

can be expanded in 3D as [58, page 32]

$$e^{ik\boldsymbol{x}\cdot\widehat{\boldsymbol{y}}} = \sum_{n=0}^{\infty}\sum_{m=-n}^{n} i^n 4\pi j_n(k\|\boldsymbol{x}\|)Y_{nm}(\widehat{\boldsymbol{x}})Y_{nm}^*(\widehat{\boldsymbol{y}}), \tag{4.25}$$

where $j_n(r)$ is the spherical function defined in (3.14) and $Y_{nm}(\cdot)$ are the spherical harmonics defined in (3.15). By applying the spherical harmonic expansion (4.25) in (4.11), we obtain

$$\begin{aligned}\Phi(\tau) = (4\pi)^2 &\sum_{n=0}^{\infty}\sum_{m=-n}^{n} e^{-in\pi/2} j_n(ku\tau)Y_{nm}(\widehat{\boldsymbol{u}}) \\ &\times \sum_{p=0}^{\infty}\sum_{q=-p}^{p} e^{ip\pi/2} j_p(kv\tau)Y_{pq}^*(\widehat{\boldsymbol{v}})\beta_{n,m}^{p,q},\end{aligned} \tag{4.26}$$

where

$$\beta_{n,m}^{p,q} = \iint_{\mathbb{S}^2\times\mathbb{S}^2} G(\widehat{\boldsymbol{\phi}},\widehat{\boldsymbol{\varphi}})Y_{n,m}(\widehat{\boldsymbol{\phi}})Y_{p,q}^*(\widehat{\boldsymbol{\varphi}})\, d\widehat{\boldsymbol{\phi}}\, d\widehat{\boldsymbol{\varphi}} \tag{4.27}$$

are the scattering environment coefficients which characterize the 3D scattering environment surrounding the receiver and transmitter regions.

According to (4.26), in addition to scattering coefficients, temporal correlation depends on transmitter and receiver velocities (u and v) and time between two received signals (τ). Simulation results in section 4.5.1 further explain these relationships.

As shown in [66], spherical Bessel functions will exhibit a high-pass nature. Therefore, using this property the infinite summations in (4.26) can be approximated as:

$$\begin{aligned}\Phi(\tau) =(4\pi)^2 &\sum_{n=0}^{M_T}\sum_{m=-n}^{n} e^{-in\pi/2} j_n(ku\tau)Y_{nm}(\widehat{\boldsymbol{u}}) \\ &\times \sum_{p=0}^{M_R}\sum_{q=-p}^{p} e^{ip\pi/2} j_p(kv\tau)Y_{pq}^*(\widehat{\boldsymbol{v}})\beta_{n,m}^{p,q},\end{aligned} \tag{4.28}$$

where $N_T \triangleq \lceil \pi e r_T/\lambda \rceil$ and $N_R \triangleq \lceil \pi e r_R/\lambda \rceil$.

Special Case: Separable Channels

In this section we consider a special case of the joint angular power distribution $G(\widehat{\boldsymbol{\phi}}, \widehat{\boldsymbol{\varphi}})$ and derive the scattering environments coefficients $\beta_{n,m}^{p,q}$ corresponding to this special case.

When the AoD $\widehat{\boldsymbol{\phi}}$ is independent of the AoA $\widehat{\boldsymbol{\varphi}}$, the joint angular power distribution $G(\widehat{\boldsymbol{\phi}}, \widehat{\boldsymbol{\varphi}})$ can be written as:

$$G(\widehat{\boldsymbol{\phi}}, \widehat{\boldsymbol{\varphi}}) = G_{Tx}(\widehat{\boldsymbol{\phi}}) G_{Rx}(\widehat{\boldsymbol{\varphi}}), \tag{4.29}$$

where

$$G_{Tx}(\widehat{\boldsymbol{\phi}}) = \int_{\mathbb{S}^2} G(\widehat{\boldsymbol{\phi}}, \widehat{\boldsymbol{\varphi}}) d\widehat{\boldsymbol{\varphi}},$$

is the angular power distribution at the transmitter, and

$$G_{Rx}(\widehat{\boldsymbol{\varphi}}) = \int_{\mathbb{S}^2} G(\widehat{\boldsymbol{\phi}}, \widehat{\boldsymbol{\varphi}}) d\widehat{\boldsymbol{\phi}}$$

is the angular power distribution at the receiver. Fading channels that satisfy (4.29) are known as separable channels or Kronecker channels. As shown in [60], the separability condition (4.29) can be assumed when there is a single scattering cluster in the scattering environment.

In this case, the scattering environment coefficients are given by

$$\beta_{n,m}^{p,q} = \beta_{n,m}^{0,0} \beta_{0,0}^{p,q}, \tag{4.30}$$

where

$$\beta_{n,m}^{0,0} = \int_{\mathbb{S}^2} G_{Tx}(\widehat{\boldsymbol{\phi}}) Y_{n,m}(\widehat{\boldsymbol{\phi}})\, d\widehat{\boldsymbol{\phi}} \tag{4.31}$$

are the scattering environment coefficients at the transmitter and

$$\beta_{0,0}^{p,q} = \int_{\mathbb{S}^2} G_{Rx}(\widehat{\boldsymbol{\varphi}}) Y_{p,q}^{*}(\widehat{\boldsymbol{\varphi}})\, d\widehat{\boldsymbol{\varphi}}.$$

are the scattering environment coefficients at the receiver.

Power distributions are mainly characterized by the mean angle of arrival φ_0 (or departure ϕ_0) and the angular spread σ at the receiver (or transmitter). A number of univariate power distributions in 3D scattering environments have been proposed in the literature for modeling the scattering distributions $G_{Tx}(\widehat{\boldsymbol{\phi}})$ and $G_{Rx}(\widehat{\boldsymbol{\varphi}})$ at the transmitter and the receiver, respectively. Few examples are, isotropic model [61], uniform limited azimuth/elevation model [65] and spherical harmonic model [65].

In this section we use the 3D von Mises-Fisher model to characterize the scattering power distribution at each end of the channel. In addition, using our temporal correlation function (4.26), we derive the temporal correlation function for the M2M channel in a 3D isotropic scattering environment.

4.5.1 Examples

In this subsection first we study the behavior of space-time cross correlation of received signals only in 3D isotropic M2M environment and secondly channel temporal correlation function under two example scattering distributions and their simulation results. For all the simulations we selected carrier frequency as 5.9 GHz. We use symbol duration, $T_s = 0.0001$ seconds and delay, $\tau = 10T_s$ for channel temporal correlation examples, .

3D Isotropic Scattering Distribution

If the waves are transmitted uniformly to all directions in 3D space, i.e., $G_{Tx}(\widehat{\boldsymbol{\phi}}) = 1/2\pi^2$, the scattering environment coefficients at the transmitter is given by:

$$\beta_{n,m}^{0,0} = \begin{cases} \dfrac{1}{\sqrt{4\pi}}, & n = m = 0 \\ 0, & \text{otherwise.} \end{cases}$$

Similarly, if the waves are impinging on the receiver uniformly from all direction in 3D space, i.e., $G_{Rx}(\widehat{\boldsymbol{\varphi}}) = 1/2\pi^2$, the corresponding scattering environment

coefficients at the receiver are given by:

$$\beta_{0,0}^{p,q} = \begin{cases} \frac{1}{\sqrt{4\pi}}, & p = q = 0 \\ 0, & \text{otherwise.} \end{cases}$$

Using (4.28), the temporal correlation function of the 3D M2M channel for 3D isotropic scattering distribution becomes

$$\Phi(\tau) = j_0(ku\tau)j_0(kv\tau). \tag{4.32}$$

Similarly, space-time cross correlation function between two received signals is

$$\Phi_{st}(\tau) = e^{iw_c\tau} j_0(k\boldsymbol{u}_{st}(\tau))j_0(k\boldsymbol{v}_{st}(\tau)). \tag{4.33}$$

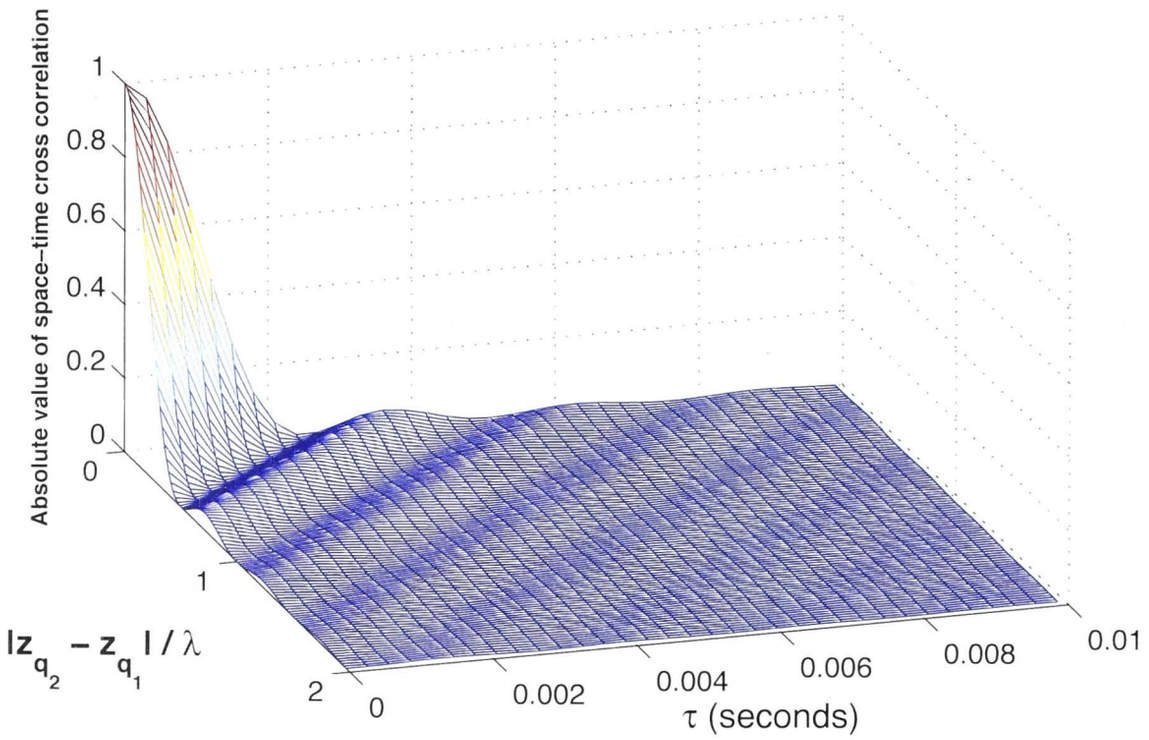

Figure 4.9: Space-time correlation between two received signals in 3D isotropic M2M environment when both transmitter and receiver are moving at 36 km/h.

The space-time correlation between received signals in the 3D isotropic envi-

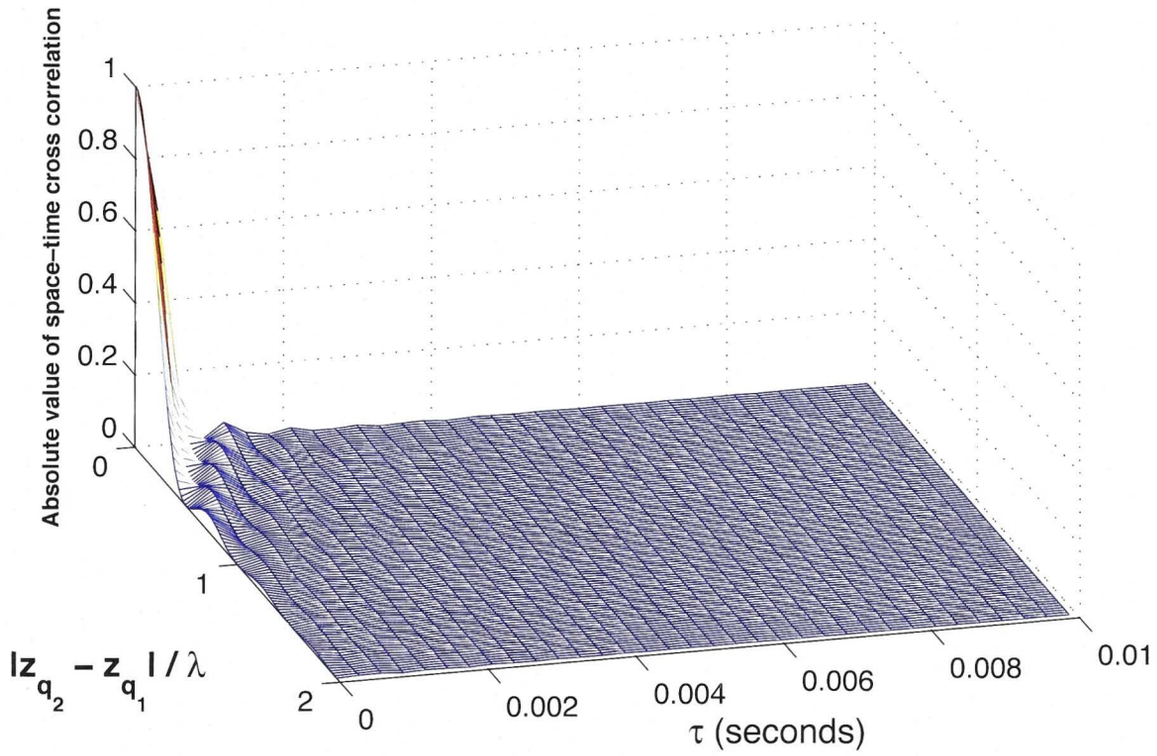

Figure 4.10: Space-time correlation between two received signals in 3D isotropic M2M environment when both transmitter and receiver are moving at 108 km/h.

ronment are shown in Fig. 4.9 and Fig. 4.10. In comparing these results with the results of 2D isotropic cases discussed in Fig. 4.1 and Fig. 4.2, it is observed that the first decorrelation happens at half wavelength distance between two receivers when time delay is zero for 3D isotropic while the decorrelation happened before half a wavelength for 2D. The observation of 3D isotropic related correlation being lower than 2D isotropic after the first decorrelation point when other conditions remain same can be justified by the fact that 3D isotropic has more potential to receive more independent signals than 2D after direct signals. In addition, Fig. 4.9 and Fig. 4.10 also confirm that correlation depends on v and u not on the ratio v/u.

The magnitude of the channel temporal correlation after 10 symbol period versus magnitude of transmitter velocity and magnitude of receiver velocity are shown in Fig. 4.11 and contour plot of the same is shown in Fig. 4.12, where both transmitter and receiver scattering distributions are isotropic. In this simulation,

transmitter and receiver are moving with zero elevation and zero azimuth angles with respect to reference points. The simulation result shows a high degree of correlation (> 0.3) until both transmitter and receiver reach 20 m/s and reduces to zero temporal correlation when transmitter and or receiver are at 25 m/s. Even though the isotropic environment is hard to find in real-world, the above derivations and simulations were performed to give a complete mathematical and theoretical analysis.

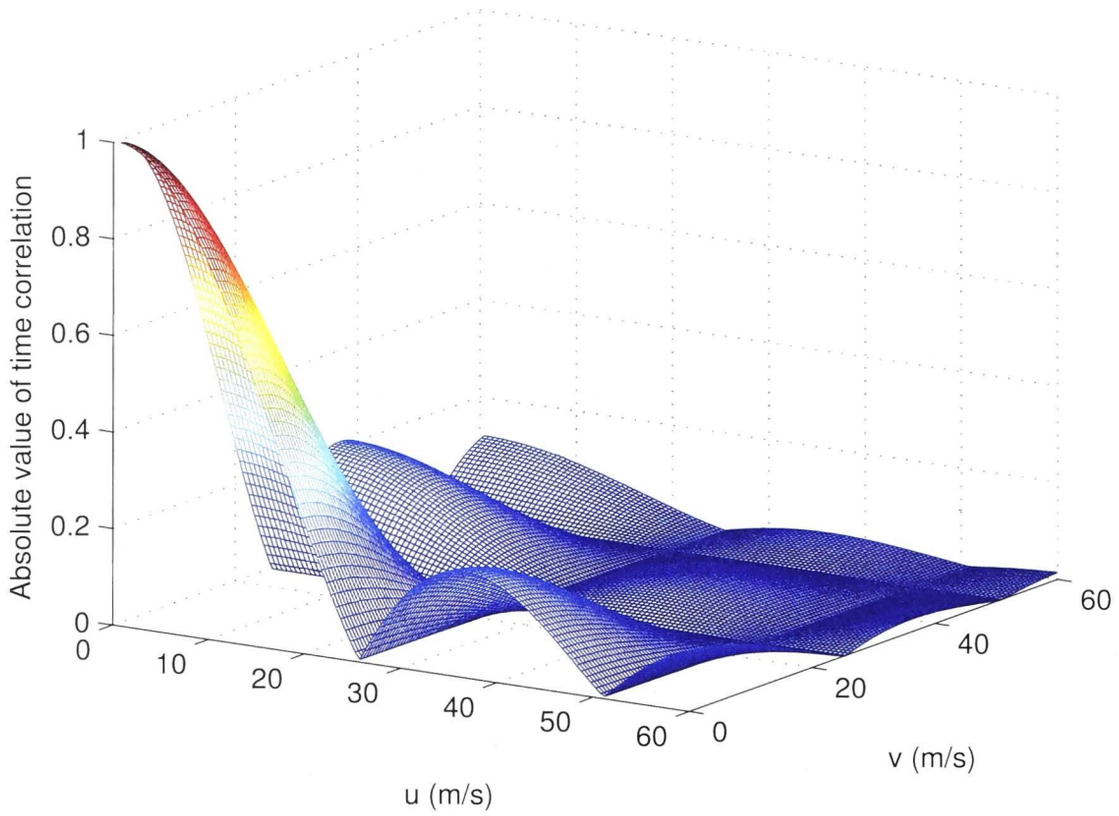

Figure 4.11: The channel temporal correlation after $\tau = 10$ symbol time periods in 3D M2M environment where both transmitter and receiver scattering distributions are isotropic.

von Mises-Fisher Distribution

The von Mises-Fisher distribution in a 3D scattering environment is defined as [67],

$$G(\theta) = \frac{\kappa}{4\pi \sinh \kappa} e^{\kappa \cos(\theta - \theta_0)}, \quad |\theta - \theta_0| \leq \pi, \tag{4.34}$$

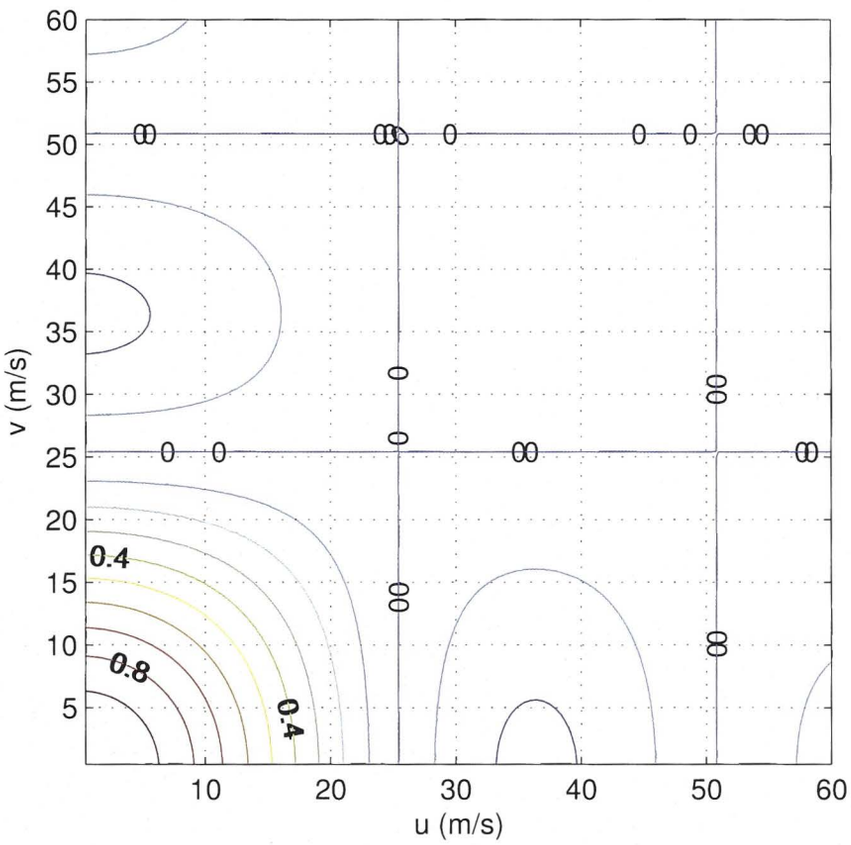

Figure 4.12: Contour plot of the channel temporal correlation after $\tau = 10$ symbol time periods in 3D M2M environment where both transmitter and receiver scattering distributions are isotropic.

where $\kappa \geq 0$ represents the non isotropy factor of the distribution. Note that $\kappa = 0$ represents isotropic scattering. As shown in [68], the scattering environment coefficients $\beta_{n,m}^{0,0}$ and $\beta_{0,0}^{p,q}$ corresponding to the von Mises-Fisher distribution are given by

$$\beta_{n,m}^{0,0} = \sqrt{\frac{\pi\kappa_T}{2}} \frac{1}{\sinh \kappa_T} I_{n+\frac{1}{2}}(\kappa_T) \frac{4}{2n+1} Y_{n,m}^*(\phi_0),$$

and

$$\beta_{0,0}^{p,q} = \sqrt{\frac{\pi\kappa_R}{2}} \frac{1}{\sinh \kappa_R} I_{p+\frac{1}{2}}(\kappa_R) \frac{4}{2p+1} Y_{p,q}^*(\varphi_0),$$

where κ_T and κ_R are the non isotropy factors at the transmitter and receiver regions, respectively and $I_m(\cdot)$ is the modified Bessel function of the first kind.

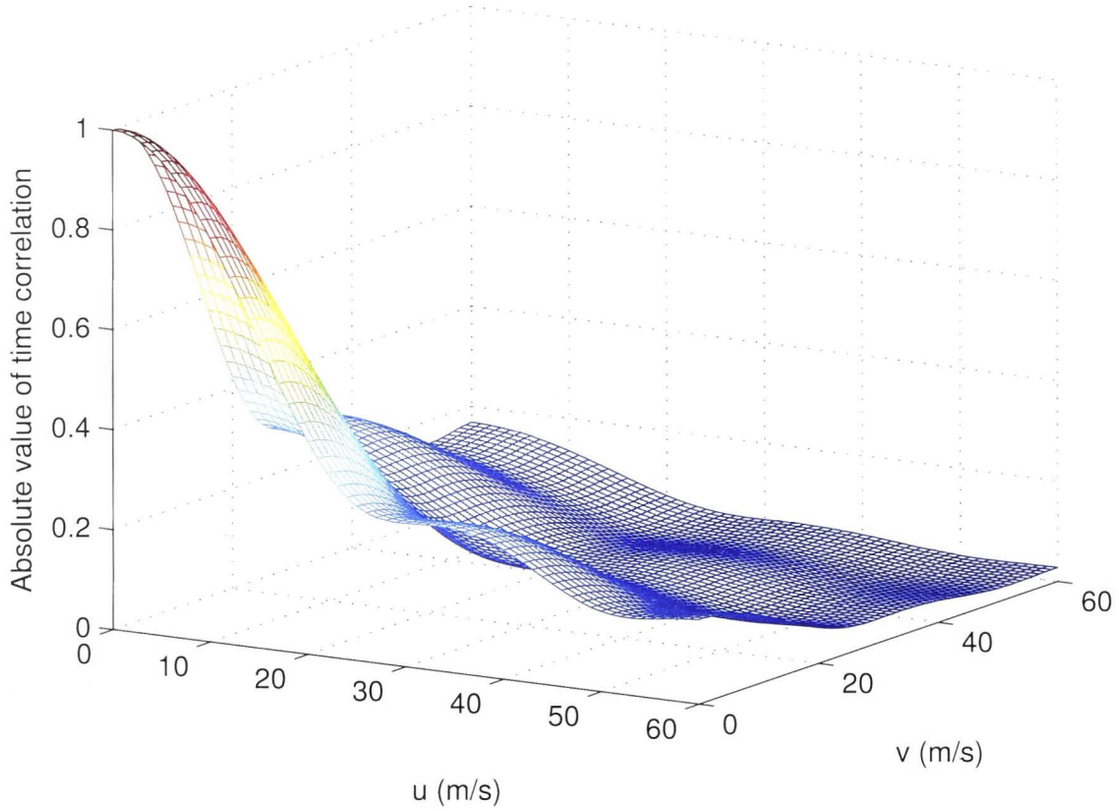

Figure 4.13: The channel temporal correlation after $\tau = 10$ symbol time periods in 3D M2M environment where both transmitter and receiver scattering distributions are von Mises-Fisher with $\kappa = 1$.

Assuming both transmitter and receiver sides are of von Mises-Fisher distribution and separable channels, the magnitude of the channel temporal correlation after 10 symbol period is shown in Fig. 4.13 and contour plot of the same is shown in Fig. 4.14. In this simulation, transmitter and receiver are moving with zero elevation and zero azimuth angles with respect to reference points. In addition, AoA and AoD also have zero elevation and azimuth angles with respect to reference points. In this situation a high degree of correlation (> 0.3) is shown until both reach 25 m/s, but when compared to isotropic case rate of reduction of temporal correlation is less.

The same equation and simulations can be used to understand the impact of

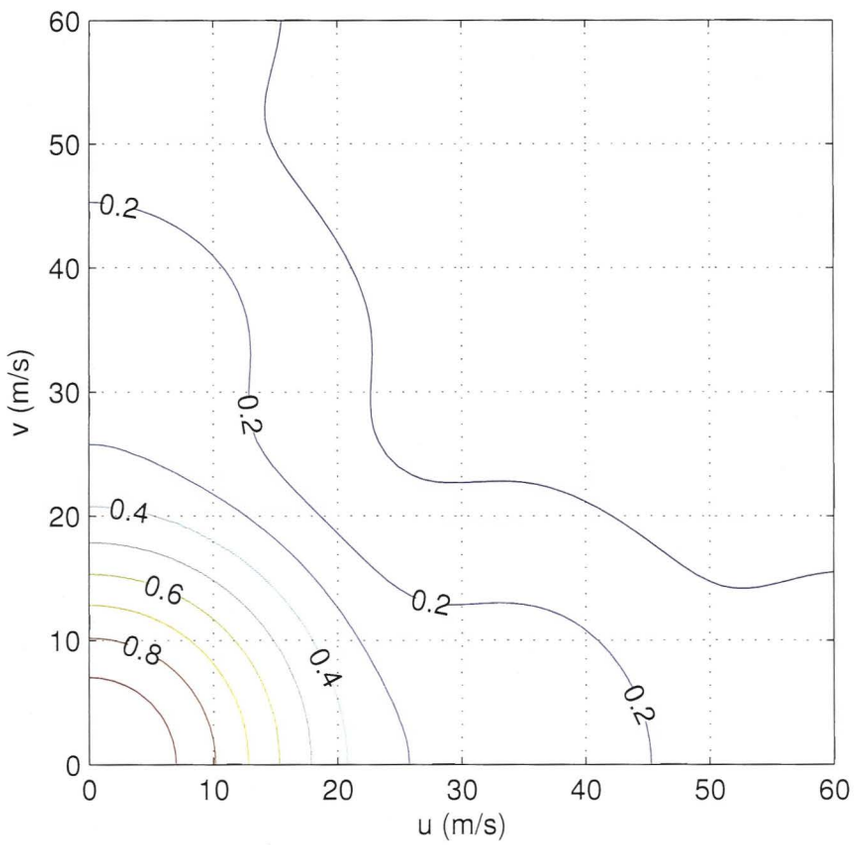

Figure 4.14: Contour plot of the channel temporal correlation after $\tau = 10$ symbol time periods in 3D M2M environment where both transmitter and receiver scattering distributions are von Mises-Fisher with $\kappa = 1$.

the eight angles (elevation and azimuth angles of transmitter velocity, receiver velocity, AoA and AoD) to the temporal correlations. One example of different angles is shown in Fig. 4.15 where transmitter azimuth and elevation angles are 30^0 and other angles remain at zero. In this situation the receiver is reaching the same temporal correlation at lower velocities than the all angles zero example. Hence the rate of reduction of temporal correlation is higher with respect to receiver velocity whereas temporal correlation related to transmitter velocity remains same in both cases.

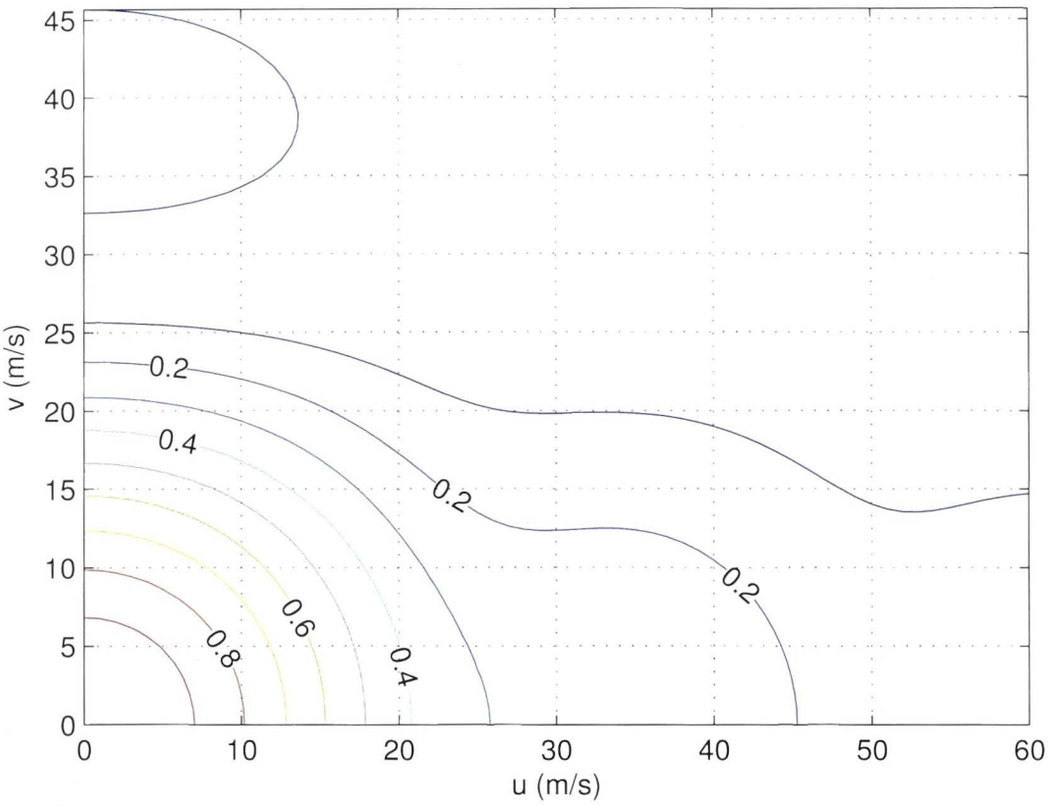

Figure 4.15: Contour plot of the channel temporal correlation after $\tau = 10$ symbol time periods in 3D M2M environment where both transmitter and receiver scattering distributions are von Mises-Fisher with $\kappa = 1$ and transmitter is moving in azimuth 30^0 and elevation 30^0 and other angles remain at zero.

4.6 Contributions and Conclusions

Contributions from this chapter can be summarized as follows.

1. Our generalized channel temporal correlation given in (4.13) is suitable for any 2D scattering environment by selecting coefficients β_m^n which characterize the 2D scattering environment surrounding the transmitter and receiver regions. Similarly it can be applied to space-time correlation of received signals as well.

2. The novel generalized channel temporal correlation given in (4.26) can be used for any 3D scattering environment by selecting coefficients $\beta_{n,m}^{p,q}$ which

characterize the 3D scattering environment surrounding the transmitter and receiver regions. Similar derivation is applied to space-time correlation of received signals as well.

3. Addressing the gap found in the literature, in this chapter in addition to the time delay and receiver antenna spacings, the effect of transmitter velocity, receiver velocity, AoA and AoD to channel temporal correlation are discussed under M2M scattering environments for the first time in M2M channel models.

We have presented unique generalized expressions for space-time cross correlation and channel temporal correlation functions that are capable of capturing 2D and 3D M2M general scattering environments characterized by the power distribution surrounding the transmitter and receiver antenna array region, antenna placement at the transmitter and receiver and velocities and the traveling direction of the transmitter and receiver. These expressions can be used to identify the required spacing between antennas of the receiver systems for a given power distribution, transmitter movement and receiver movement. In addition, many of the statistical properties of the complex envelope can be determined from its time correlation, for example, power spectrum can be obtained by performing the Fourier transform, the time correlation of the complex envelope and also second order statistical properties such as level crossing rate and average fade duration can also be derived.

Chapter 5

Space-Frequency Correlation

5.1 Introduction

We detailed our novel channel models in Chapter 3 and developed the time correlation of those models in Chapter 4. This chapter is devoted to the development of expressions for the space-frequency correlation at the receiver in time invariant frequency selective multicarrier multiple input multiple output (MIMO) mobile to mobile (M2M) channel model introduced in Section 3.5.

When analyzing the literature, we came across two contributions related to frequency correlation of M2M channel models. In [69], they have derived closed-form space-time frequency (STF) correlation functions for MIMO M2M multicarrier Ricean fading channels in non-isotropic scattering environments based on the two ring model with single and double bounced rays. In [70], they have presented a double ring M2M channel model based upon a three dimensional (3D) STF correlation function via combining the antenna pattern, Doppler shift and delay profile.

We identified that the contributions in literature are specific to the environments and the discussion of the impact of transmitter and receiver velocity is lacking in those contributions. Motivated by those gaps in the literature, we propose our generalized framework of space-frequency correlation in multicarrier M2M channel environments. Our objectives in this chapter are mainly twofold, first to introduce the generalized framework that can be used for any multicarrier

M2M environment, and secondly to discuss the impact of transmitter and receiver velocity in space-frequency correlation.

In this chapter we extend the fixed to mobile (F2M) space-frequency correlation model at the receiver side in closed-form applicable in two dimensional (2D) and 3D scattering environments discussed in [71] to the M2M environment. We used modal analysis approach introduced in [65] to derive a space-frequency correlation in the M2M environment. The proposed M2M space-frequency correlation captures the spatial information of the channel through antenna locations while frequency selectivity of the multipath channel is captured through joint angular power delay distribution. The importance of the proposed framework is demonstrated by applying it on an orthogonal frequency division multiplexing (OFDM) system, which is discussed in Section 5.4. The proposed framework is useful for realistic performance evaluation and comprehensive understanding of MIMO M2M multicarrier systems especially for system designing. The currently used high speed downlink packet access (HSDPA) and long term evolution (LTE) radio access technology are providing a very large increase in data transmission capacity in mobile networks. This is being matched and even exceeded by a corresponding increase in the demand for data from users of the latest data hungry devices and applications. Even though they are mainly focusing on F2M applications today, it will be required for M2M applications tomorrow. Our proposed model will play an important role in order to achieve these future requirements.

The rest of this chapter is organized as follows. We introduce multicarrier MIMO M2M space-frequency correlation for 2D and 3D scattering environments in Section 5.2. In Section 5.3 we discuss four different joint angular power delay distributions, which can be used for further analysis of space-frequency correlation. We simulate space-frequency correlation in different situations in Section 5.4. Finally, Section 5.5 concludes the chapter.

5.2 Space-Frequency Correlation

Space-frequency correlation function is a useful indicator of dependencies as a function of space and frequency. In MIMO M2M multi-carrier systems, the space-frequency correlation $\Phi_{sf}(n, m)$ between the n-th subcarrier related to p_1-th trans-

mit antenna and q_1-th receive antenna and the m-th subcarrier related to p_2-th transmit antenna and q_2-th receive antenna is given by

$$\Phi_{sf}(n,m) \triangleq E\left\{H_{p_1,q_1}(n)H^*_{p_2,q_2}(m)\right\}, \tag{5.1}$$

where $E\{\cdot\}$ is the statistical expectation operator, $H_{p_1,q_1}(n)$ is the channel frequency response at the n-th subcarrier related to p_1-th transmit antenna and q_1-th receive antenna, $H_{p_2,q_2}(m)$ is the channel frequency response at the m-th subcarrier related to p_2-th transmit antenna and q_2-th receive antenna and $(\cdot)^*$ denotes the complex conjugate operation. By substituting $H_{p,q}(n)$ from (3.25) we obtain,

$$\begin{aligned}\Phi_{sf}(n,m) = \int_{\Omega_T}\int_{\Omega_T}\int_{\Omega_R}\int_{\Omega_R} E\Big\{ \int_{\tau} g(\widehat{\boldsymbol{\phi}}_1,\widehat{\boldsymbol{\varphi}}_1,\tau)e^{-i2\pi(f_c-(n+0.5)\Delta f)\tau}\,d\tau \\ \times \int_{\tau} g^*(\widehat{\boldsymbol{\phi}}_2,\widehat{\boldsymbol{\varphi}}_2,\tau)e^{-i2\pi(f_c-(m+0.5)\Delta f)\tau}\,d\tau\Big\} \\ \times e^{-i\frac{1}{c}\omega_n \boldsymbol{u}_{p_1}\cdot\widehat{\boldsymbol{\phi}}_1} e^{i\frac{1}{c}\omega_m \boldsymbol{u}_{p_2}\cdot\widehat{\boldsymbol{\phi}}_2} e^{-i\frac{1}{c}\omega_n \boldsymbol{u}_{q_1}\cdot\widehat{\boldsymbol{\varphi}}_1} e^{i\frac{1}{c}\omega_m \boldsymbol{u}_{q_2}\cdot\widehat{\boldsymbol{\varphi}}_2}\, d\widehat{\boldsymbol{\phi}}_1\, d\widehat{\boldsymbol{\phi}}_2\, d\widehat{\boldsymbol{\varphi}}_1\, d\widehat{\boldsymbol{\varphi}}_2,\end{aligned} \tag{5.2}$$

where $\omega_k = 2\pi(f_c - (k+0.5)\Delta f)$.

Equation (5.2) can be further simplified as,

$$\begin{aligned}\Phi_{sf}(n,m) = \int_{\Omega_T}\int_{\Omega_R}\int_{\tau} P(\widehat{\boldsymbol{\phi}},\widehat{\boldsymbol{\varphi}},\tau)e^{-i2\pi(m-n)\Delta f\tau} e^{-i\frac{1}{c}(\omega_n \boldsymbol{u}_{p_1}-\omega_m \boldsymbol{u}_{p_2})\cdot\widehat{\boldsymbol{\phi}}} \\ \times e^{-i\frac{1}{c}(\omega_n \boldsymbol{u}_{q_1}-\omega_m \boldsymbol{u}_{q_2})\cdot\widehat{\boldsymbol{\varphi}}}\, d\tau\, d\widehat{\boldsymbol{\phi}}\, d\widehat{\boldsymbol{\varphi}},\end{aligned} \tag{5.3}$$

$P(\widehat{\boldsymbol{\phi}},\widehat{\boldsymbol{\varphi}},\tau)$ is the joint angular power delay profile denoted as

$$P(\widehat{\boldsymbol{\phi}},\widehat{\boldsymbol{\varphi}},\tau) \triangleq E\left\{|g(\widehat{\boldsymbol{\phi}},\widehat{\boldsymbol{\varphi}},\tau)|^2\right\}.$$

We apply this generalized space-frequency correlation in (5.3) to 2D and 3D scattering environments in next two subsections.

5.2.1 2D Scattering Environment

In deriving the space-frequency correlation function for a 2D scattering environment, we use the cylindrical harmonic expansion of plane waves [58, page 67], $e^{-i(\omega_n \boldsymbol{u}_{p_1} - \omega_m \boldsymbol{u}_{p_2})\cdot\widehat{\boldsymbol{\phi}}/c}$ in (5.3) which can be expanded as

$$e^{-i(\omega_n \boldsymbol{u}_{p_1} - \omega_m \boldsymbol{u}_{p_2})\cdot\widehat{\boldsymbol{\phi}}/c} = \sum_{k=-\infty}^{\infty} i^k e^{ik(\phi_{p_1,p_2}-\phi)} J_k(\frac{1}{c}\|(\omega_n \boldsymbol{u}_{p_1} - \omega_m \boldsymbol{u}_{p_2})\|). \tag{5.4}$$

Similarly, $e^{-i(\omega_n \boldsymbol{u}_{q_1} - \omega_m \boldsymbol{u}_{q_2})\cdot\widehat{\boldsymbol{\varphi}}/c}$ in (5.3) can be expanded as

$$e^{-i(\omega_n \boldsymbol{u}_{q_1} - \omega_m \boldsymbol{u}_{q_2})\cdot\widehat{\boldsymbol{\varphi}}/c} = \sum_{\ell=-\infty}^{\infty} i^\ell e^{i\ell(\psi_{q_1,q_2}-\psi)} J_\ell(\frac{1}{c}\|(\omega_n \boldsymbol{u}_{q_1} - \omega_m \boldsymbol{u}_{q_2})\|). \tag{5.5}$$

By substituting (5.4) and (5.5) in (5.3), we obtain

$$\begin{aligned}\Phi_{sf}(n,m) = \int_{\Omega_T}\int_{\Omega_R} P(\widehat{\boldsymbol{\phi}},\widehat{\boldsymbol{\varphi}},\tau) e^{-i2\pi(m-n)\Delta f\tau} \sum_{k=-\infty}^{\infty} i^k e^{ik(\phi_{p_1,p_2}-\phi)} \\ \times J_k(\frac{1}{c}\|(\omega_n \boldsymbol{u}_{p_1} - \omega_m \boldsymbol{u}_{p_2})\|) \\ \times \sum_{\ell=-\infty}^{\infty} i^\ell e^{i\ell(\psi_{q_1,q_2}-\psi)} J_\ell(\frac{1}{c}\|(\omega_n \boldsymbol{u}_{q_1} - \omega_m \boldsymbol{u}_{q_2})\|)\, d\tau\, d\widehat{\boldsymbol{\phi}}\, d\widehat{\boldsymbol{\varphi}}.\end{aligned} \tag{5.6}$$

Space-frequency correlation for the 2D scattering environment can be further simplified to

$$\begin{aligned}\Phi_{sf}(n,m) = \sum_{\ell=-\infty}^{\infty}\sum_{k=-\infty}^{\infty} \beta_{k,\ell}(n,m) i^k e^{ik\phi_{p_1,p_2}} \\ \times i^\ell e^{i\ell\psi_{q_1,q_2}} J_k(\frac{1}{c}\|(\omega_n \boldsymbol{u}_{p_1} - \omega_m \boldsymbol{u}_{p_2})\|) J_\ell(\frac{1}{c}\|(\omega_n \boldsymbol{u}_{q_1} - \omega_m \boldsymbol{u}_{q_2})\|),\end{aligned} \tag{5.7}$$

where

$$\beta_{k,\ell}(n,m) = \int_0^\pi \int_0^\pi \int_\tau P(\widehat{\boldsymbol{\phi}},\widehat{\boldsymbol{\varphi}},\tau) e^{-i2\pi(m-n)\Delta f\tau} e^{-ik\phi} e^{-i\ell\psi}\, d\tau\, d\widehat{\boldsymbol{\phi}}\, d\widehat{\boldsymbol{\varphi}} \tag{5.8}$$

are the scattering environment coefficients which characterize the 2D scattering environment surrounding the transmitter and receiver antenna arrays and $P(\widehat{\boldsymbol{\phi}}, \widehat{\boldsymbol{\varphi}}, \tau)$ is the joint angular power delay distribution of M2M system. Note that scattering coefficients $\beta_{k,\ell}(n,m)$ are independent of the transmitter and receiver velocity. Hence the $\beta_{k,\ell}(n,m)$ is invariant to Doppler effects and is fixed for a given scattering distribution.

2D angular-delay profile

The joint 2D angular power delay distribution of M2M system, $P(\widehat{\boldsymbol{\phi}}, \widehat{\boldsymbol{\varphi}}, \tau)$ can be expressed using spatial basis functions on scattering free circles of the receivers and transmitters. Using cylindrical harmonics,

$$P(\widehat{\boldsymbol{\phi}}, \widehat{\boldsymbol{\varphi}}, \tau) = \sum_{n=0}^{\infty}\sum_{m=0}^{\infty}\sum_{k=0}^{\infty}\sum_{\ell=0}^{\infty} \beta_{k,\ell}(n,m) e^{-i2\pi(m-n)\Delta f \tau} e^{-ik\phi} e^{-i\ell\psi}. \tag{5.9}$$

This will be further analyzed in Section 5.3 by applying to specific scatterer density models.

5.2.2 3D Scattering Environment

In a similar manner, we derive the space-frequency correlation function for a 3D scattering environment using the spherical harmonic expansion of plane waves [58, page 32], $e^{-i\frac{1}{c}(\omega_n \boldsymbol{u}_{p_1} - \omega_m \boldsymbol{u}_{p_2})\cdot\widehat{\boldsymbol{\phi}}}$ in (5.3) which is expanded as

$$\begin{aligned} e^{-i\frac{1}{c}(\omega_n \boldsymbol{u}_{p_1} - \omega_m \boldsymbol{u}_{p_2})\cdot\widehat{\boldsymbol{\phi}}} &= 4\pi \sum_{k=0}^{\infty} i^k j_k\left(\frac{1}{c}\|(\omega_n \boldsymbol{u}_{p_1} - \omega_m \boldsymbol{u}_{p_2})\|\right) \\ &\quad \times \sum_{v=-k}^{k} Y_{k,v}(\widehat{\boldsymbol{u}}_{p_1,p_2}) Y_{k,v}^{*}(\widehat{\boldsymbol{\phi}}), \end{aligned} \tag{5.10}$$

where $j_k(r)$ is the spherical function defined in (3.14), $\widehat{\boldsymbol{u}}_{p_1,p_2} = (\omega_n \boldsymbol{u}_{p_1} - \omega_m \boldsymbol{u}_{p_2})/\|(\omega_n \boldsymbol{u}_{p_1} - \omega_m \boldsymbol{u}_{p_2})\|$ and $Y_{nm}(\cdot)$ are the spherical harmonics defined in (3.15). By applying

the spherical harmonic expansion (5.10) in (5.3), we obtain

$$\Phi_{sf}(n,m) = 16\pi^2 \sum_{\ell=0}^{\infty}\sum_{k=0}^{\infty} \beta_{k,\ell}(n,m) i^k j_k(\frac{1}{c}\|(\omega_n \boldsymbol{u}_{p_1} - \omega_m \boldsymbol{u}_{p_2})\|) \sum_{v=-k}^{k} Y_{k,v}(\widehat{\boldsymbol{u}}_{p_1,p_2}) \times i^{\ell} j_{\ell}(\frac{1}{c}\|(\omega_n \boldsymbol{u}_{q_1} - \omega_m \boldsymbol{u}_{q_2})\|) \sum_{u=-\ell}^{\ell} Y_{\ell,u}(\widehat{\boldsymbol{u}}_{q_1,q_2}), \tag{5.11}$$

where

$$\beta_{k,\ell}(n,m) = \int_0^{\pi}\int_0^{\pi} P(\widehat{\phi},\widehat{\varphi},\tau) e^{-i2\pi(m-n)\Delta f \tau} Y^*_{k,v}(\widehat{\phi}) Y^*_{\ell,u}(\widehat{\varphi})\, d\widehat{\phi}\, d\widehat{\varphi}. \tag{5.12}$$

3D angular-delay profile

Using spherical harmonics of scattering free spheres of the receivers and transmitters, the joint 3D angular power delay distribution of M2M system, $P(\widehat{\phi},\widehat{\varphi},\tau)$, can be expressed as [66],

$$P(\widehat{\phi},\widehat{\varphi},\tau) = \sum_{n=0}^{\infty}\sum_{m=0}^{\infty}\sum_{k=0}^{\infty}\sum_{v=-k}^{k}\sum_{\ell=0}^{\infty}\sum_{u=-\ell}^{\ell} \beta_{k,\ell}(n,m) e^{-i2\pi(m-n)\Delta f \tau} Y^*_{k,v}(\widehat{\phi}) Y^*_{\ell,u}(\widehat{\varphi}). \tag{5.13}$$

5.3 Joint Angular Power Delay Distribution

The joint angular power delay distribution, $P(\widehat{\phi},\widehat{\varphi},\tau)$ is a joint function of the AoD, $\widehat{\phi}$, angle of arrival (AoA), $\widehat{\varphi}$ and the time of arrival (ToA), τ. As a special case, assuming AoD is independent with AoA and ToA, the function $P(\widehat{\phi},\widehat{\varphi},\tau)$ can be decomposed to $P(\widehat{\phi},\widehat{\varphi},\tau) = P(\widehat{\phi})P(\widehat{\varphi},\tau)$.

Next, to express the joint ToA/AoA density in terms of the original scatterer density function, let the xy coordinate system be defined such that the transmitter is at the origin and the receiver lies on the x axis. Then by relating polar

coordinates to rectangular coordinates through the following equations,

$$x = r_b \cos(\widehat{\varphi}), \tag{5.14}$$

$$y = r_b \sin(\widehat{\varphi}), \tag{5.15}$$

and in [72] the joint ToA/AoA density function as follows:

$$P(\widehat{\varphi}, \tau) = \frac{(D^2 - \tau^2 c^2)(D^2 c + \tau^2 c^3 - 2\tau c^2 D\cos(\widehat{\varphi}))}{4(D\cos(\widehat{\varphi}) - \tau c)^3} \times P_{x,y}(r_b \cos(\widehat{\varphi}), r_b \sin(\widehat{\varphi})), \tag{5.16}$$

where the distance between transmitter and receiver is D and $P_{x,y}(\cdot,\cdot)$ is a scatterer density function. Few examples for scatterer density function are Elliptical and Circular scattering models in [72], Gaussian scatterer density model in [73] and inverted parabolic spatial distribution model in [74]. We map the above general model in (5.16) to a few specific scatterer density models in the subsections to follow.

5.3.1 Uniform Scatterer Density Model

When the scatterers are uniformly distributed within an arbitrarily shaped region R_A with an area A , the scatterer density function is given by

$$P_{x,y}(x,y) = \begin{cases} 1/A & x \text{ and } y \in R_A \\ 0 & \text{otherwise} \end{cases}. \tag{5.17}$$

In this special case, the joint ToA/AoA probability density function (pdf) reduces to

$$P(\widehat{\varphi}, \tau) = \frac{(D^2 - \tau^2 c^2)(D^2 c + \tau^2 c^3 - 2\tau c^2 D\cos(\widehat{\varphi}))}{4A(D\cos(\widehat{\varphi}) - \tau c)^3}, \tag{5.18}$$

where the appropriate range of τ and $\widehat{\varphi}$ are assumed.

5.3.2 Elliptical Scattering Models

Joint ToA/AoA pdf at the receiver is same as the above uniform scatter model but area of an ellipse is given by $A = \pi a_m b_m$. The case when $\widehat{\varphi} = 0$ is considered separately, due to the zero/zero condition which occurs when substituting and directly into the expression of (5.18) we can rewrite elliptical scattering models as follows:

$$P(\widehat{\varphi},\tau) = \begin{cases} \dfrac{(D^2-\tau^2c^2)(D^2c+\tau^2c^3-2\tau c^2 D\cos(\widehat{\varphi}))}{4\pi a_m b_m (D\cos(\widehat{\varphi})-\tau c)^3} & \dfrac{D}{c} \le \tau \le \tau_m,\ \widehat{\varphi} \neq 0 \\ \dfrac{c(D+\tau c)}{4\pi a_m b_m} & \dfrac{D}{c} \le \tau \le \tau_m,\ \widehat{\varphi} = 0 \\ 0 & \text{otherwise} \end{cases} \cdot \tag{5.19}$$

5.3.3 Inverted Parabolic Spatial Distribution

Scatterers here are randomly located with a Cartesian "inverted parabolic" spatial density

$$P_{x,y}(x,y) = \begin{cases} \dfrac{2}{\pi R^2}\left[1 - \dfrac{(x-D)^2+y^2}{R^2}\right] & \text{whenever } (x-D)^2+y^2 \le R^2 \\ 0 & \text{otherwise} \end{cases} . \tag{5.20}$$

In this special case, the joint ToA/AoA pdf reduces to

$$\begin{aligned} P(\widehat{\varphi},\tau) = {} & \frac{(D^2-\tau^2c^2)(D^2c+\tau^2c^3-2\tau c^2 D\cos(\widehat{\varphi}))}{4(D\cos(\widehat{\varphi})-\tau c)^3} \\ & \times \frac{2}{\pi R^2}\left[1 - \frac{(r_b\cos(\widehat{\varphi})-D)^2+(r_b\sin(\widehat{\varphi}))^2}{R^2}\right] \end{aligned} \tag{5.21}$$

By substituting $r_b = (D^2-\tau^2c^2)/2(D\cos(\widehat{\varphi})-\tau c)$ we obtain

$$\begin{aligned} P(\widehat{\varphi},\tau) = {} & \frac{c}{2\pi D}\frac{[1-(\frac{\tau c}{D})^2][1+(\frac{\tau c}{D})^2-2\frac{\tau c}{D}\cos(\widehat{\varphi})]}{(\cos(\widehat{\varphi})-\frac{\tau c}{D})^3} \\ & \times \left(\frac{R}{D}\right)^{-4}\left\{\left(\frac{R}{D}\right)^2 - 1 - \left[\frac{1-(\frac{\tau c}{D})^2}{2(\cos(\widehat{\varphi})-\frac{\tau c}{D})}\right]^2 + \frac{[1-(\frac{\tau c}{D})^2]\cos(\widehat{\varphi})}{\cos(\widehat{\varphi})-\frac{\tau c}{D}}\right\} \end{aligned} \tag{5.22}$$

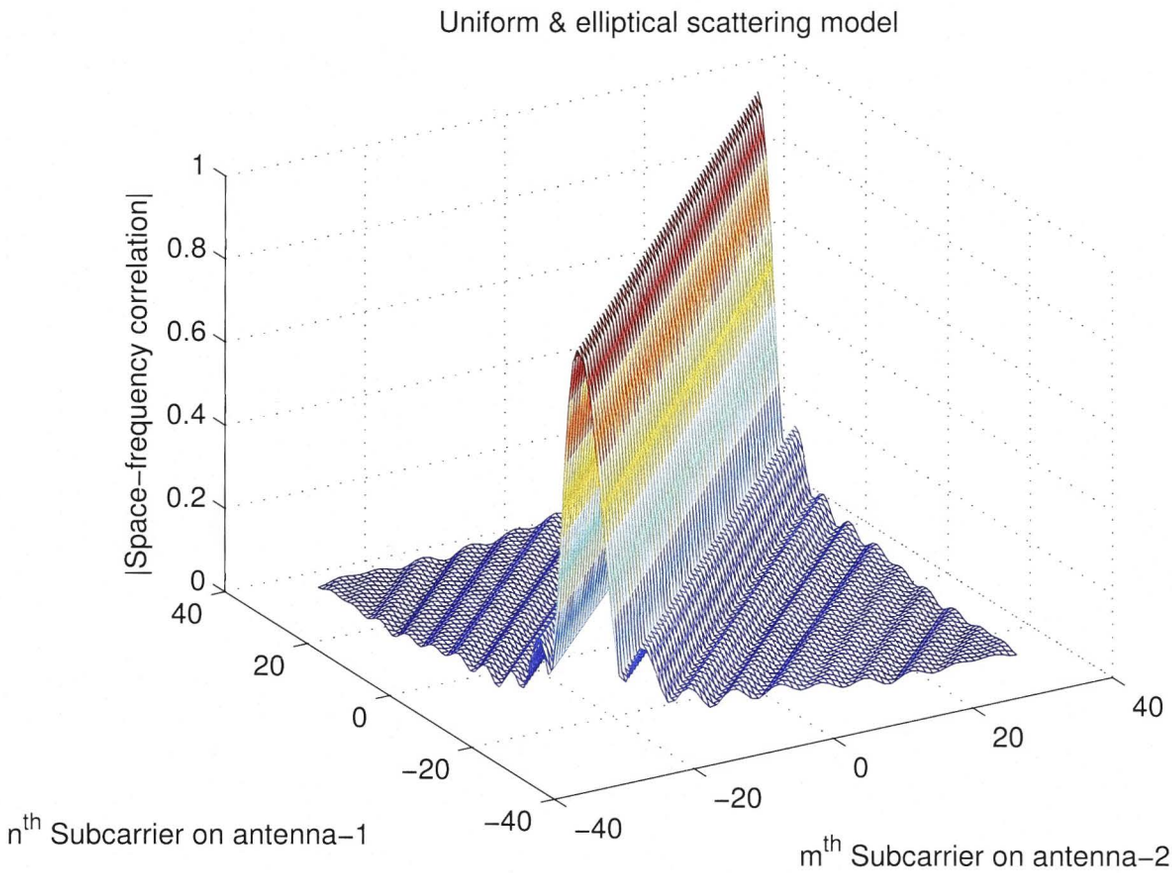

Figure 5.1: Space-frequency correlation function across subcarriers on two receive antennas placed $D = 0.25\lambda$ apart for the elliptical scattering model in 2D M2M environment.

and $P(\widehat{\varphi}, \tau) = 0$ when $(r_b \cos(\widehat{\varphi}) - D)^2 + (r_b \sin(\widehat{\varphi}))^2 \leq R^2$ is false.

5.4 Examples

In this subsection we simulate space-frequency correlation developed above by applying it on a MIMO OFDM system with $fc = 5.25$ GHz, $Ns = 64$ sub-carriers and $\Delta f = 250$ kHz, $P(\widehat{\phi}) = 1/2\pi$. The joint angle delay power distribution $P(\widehat{\varphi}, \tau)$ at the receiver aperture is modeled using elliptical scattering model derived in [72] and inverted-parabolic (IP) spatial distribution model derived in [74].

The space-frequency correlation function as a function of the subcarrier number for the elliptical scattering model and IP model are shown in Fig. 5.1 and Fig. 5.2,

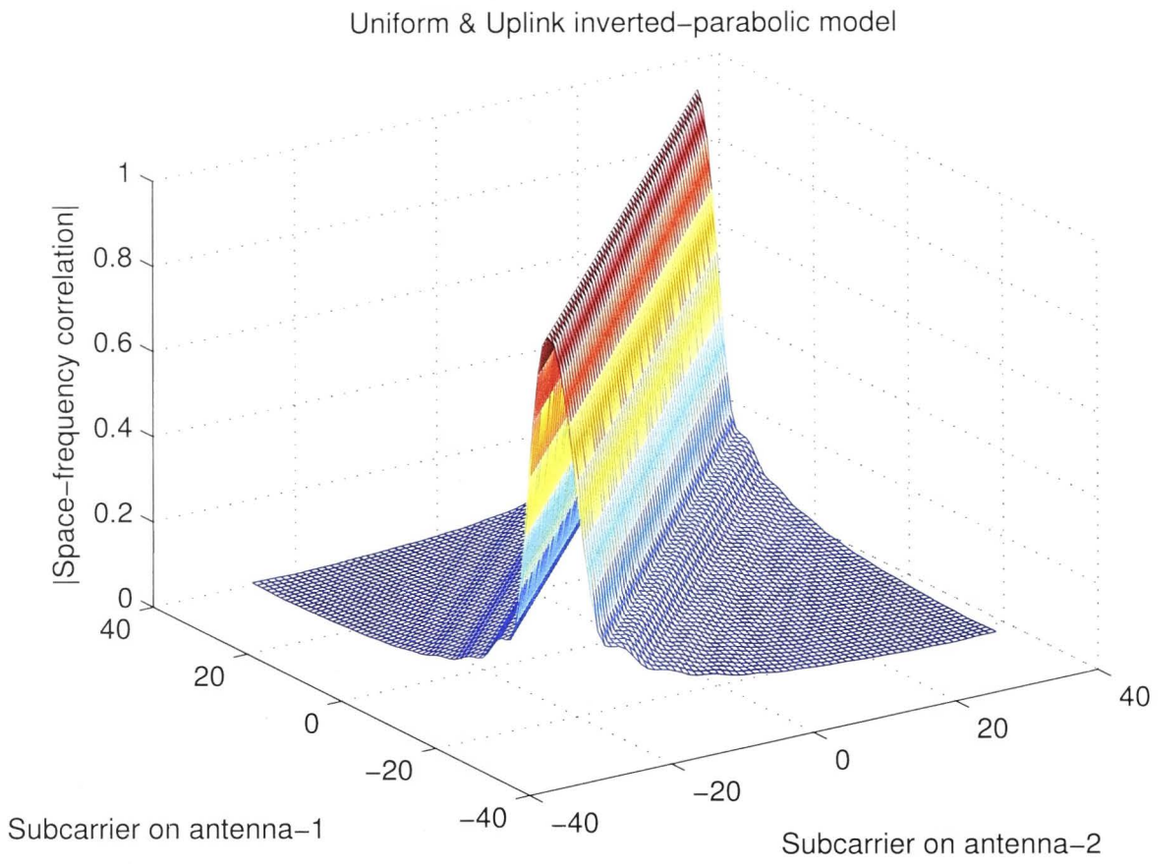

Figure 5.2: Space-frequency correlation function across subcarriers on two receive antennas placed $d = 0.25\lambda$ apart for the inverted-parabolic model in 2D M2M environment.

respectively. We carry out the simulations with the same assumptions and values as in [71] which was performed for F2M systems. The two receive antennas are located on the x-axis symmetrically about the receiver origin and separated by a distance $D = 0.25\lambda$. Similar results are observed for both scattering distributions where space-frequency correlation decreases as the frequency separation increases and high space-frequency correlation is observed at adjacent subcarriers (see Fig. 5.3 for the contour plots of $\Phi_{sf}(n, m)$ for the IP model shown in Fig. 5.2).

In Fig. 5.4 we analyze space-frequency impact due to transmitter and receiver velocities, for which the contour plot in Fig. 5.5 clearly indicates the fact that when transmitter or receiver velocity increases, the space-frequency correlation will be reduced in small amounts.

Similar set of simulations can be carried out using (5.11) with suitable 3D

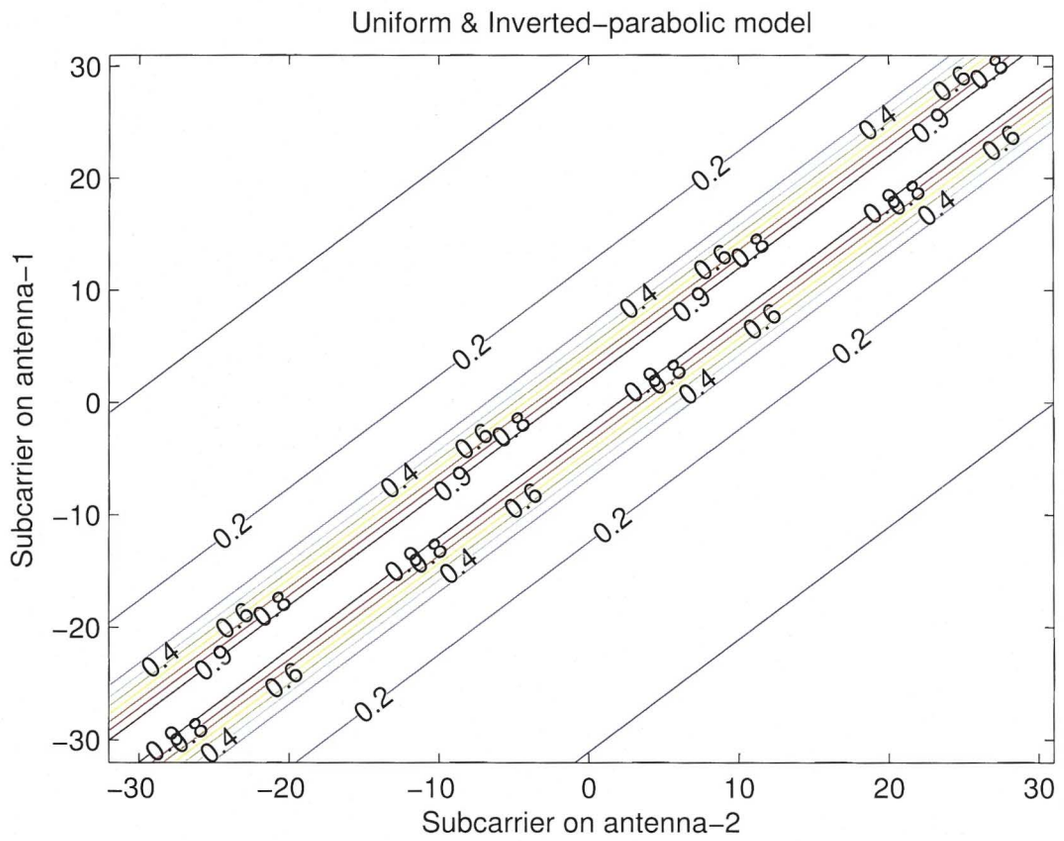

Figure 5.3: Contour plot of the space-frequency correlation function shown in Fig. 5.2 for the inverted-parabolic model in 2D M2M environment.

scattering environments.

5.5 Contributions and Conclusions

Contributions from this chapter can be summarized as follows.

1. Our generalized space-frequency correlation given in (5.7) is suitable for any 2D scattering environment by selecting coefficients $\beta_{z,a}(n,m)$ which characterize the 2D scattering environment surrounding the transmitter and receiver regions.

2. The novel generalized space-frequency correlation given in (5.11) is made to be suitable for any 3D scattering environment by selecting coefficients

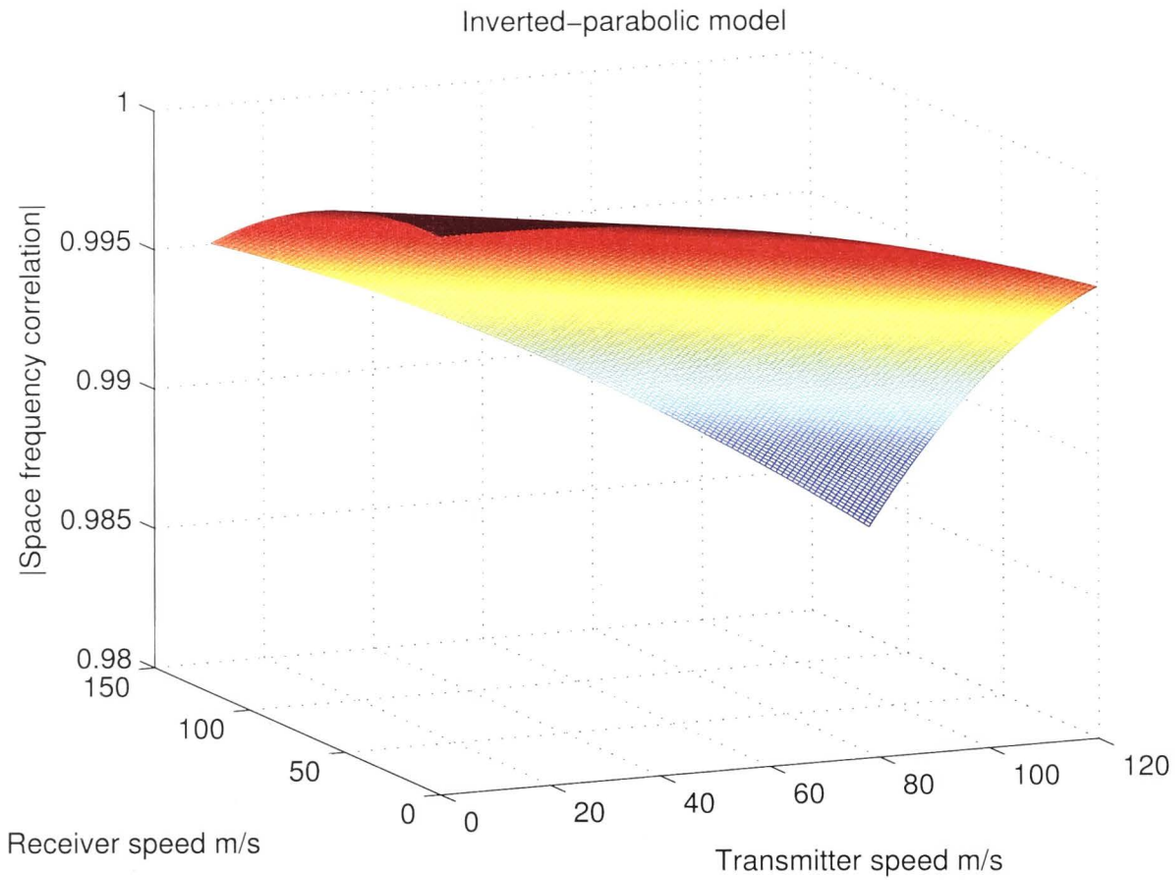

Figure 5.4: Space-frequency correlation function across subcarriers on two receive antennas placed $d = 0.25\lambda$ apart for the inverted-parabolic model in 2D M2M environment.

$\beta_{z,a}(n, m)$ which characterize the 3D scattering environment surrounding the transmitter and receiver regions.

3. Addressing the gap found in the literature, in this chapter the effects of transmitter velocity and receiver velocity to space-frequency correlation are discussed under M2M scattering environments for the first time for M2M channel models.

Thus, a framework has been proposed which can be used to calculate the space-frequency correlation in multicarrier M2M communication systems. The proposed framework captures the space dimensionality of the channel through physical antenna positions while the random frequency selective multipath field is captured through a general joint angular power delay distribution $P(\widehat{\phi}, \widehat{\varphi}, \tau)$.

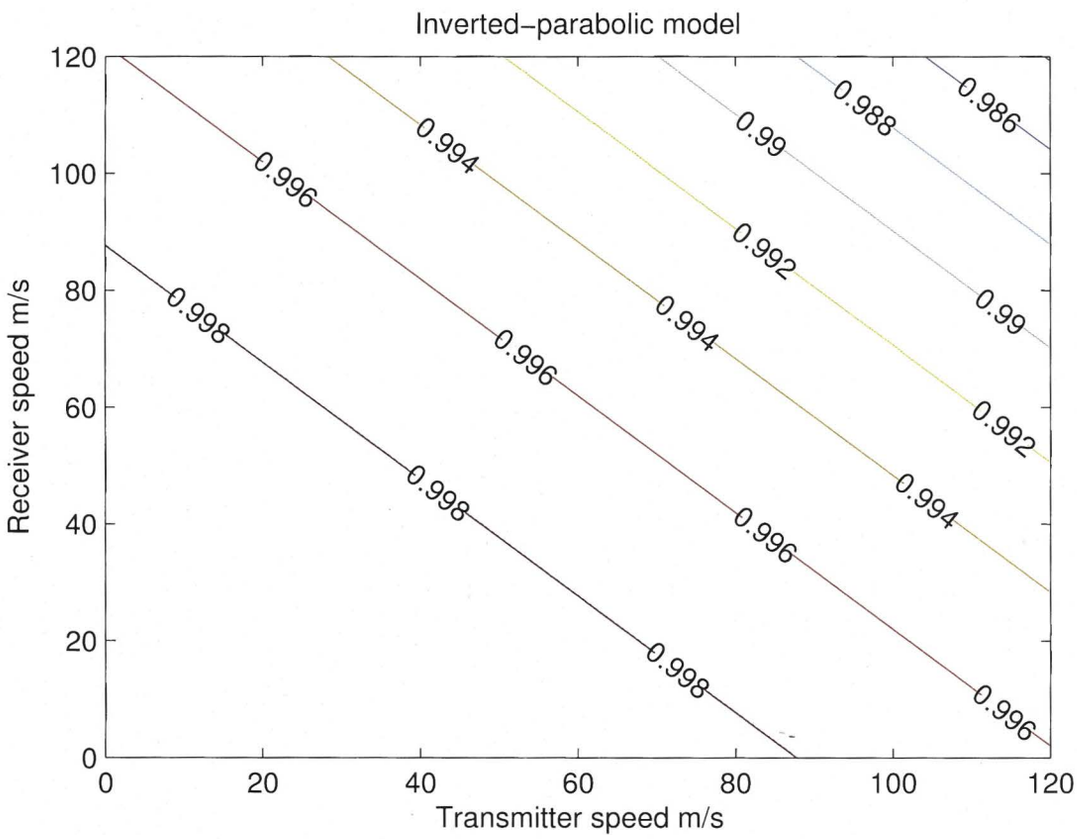

Figure 5.5: Contour plot of the space-frequency correlation function shown in Fig. 5.4 for the inverted-parabolic model in 2D M2M environment.

Chapter 6

Second-Order Channel Statistics

6.1 Introduction

Mathematical channel models are part and parcel of communication system designs, where second order statistics become more important at the final stage of the design. The level crossing rate (LCR) is a measure of the rapidity of the fading. It quantifies how often the fading crosses a certain threshold, usually in the positive-going direction. The average fade duration (AFD) quantifies how long the signal spends below the threshold. These are two important second order statistics to assess system characteristics such as handoff, velocities of the transmitter and receiver, and fading rate [75, 76]. The main applications of mobile to mobile (M2M) systems are in mobile ad hoc wireless networks and intelligent transport systems which are discussed in Section 2.2. In this chapter we discuss LCR and AFD in M2M wireless communication channels under isotropic and non-isotropic scattering environments.

In the literature, LCR and AFD in M2M channels have been discussed under various environments for numerous channel models. Akki and Harber [2, 9], who were the first to propose a M2M channel model, focused on single input single output (SISO) M2M Rayleigh fading radio channel under non line of sight conditions and also derived LCR and AFD for the same M2M channels. In [77] and [76], LCR and AFD are derived for three dimensional (3D) analytical model and 3D wideband model respectively, for which they used von-Mises scattering environment

and Ricean fading channel.

The papers [78] and [79] presented the fading behavior by analyzing LCR and AFD of the received envelope of M2M fading channels in relay-based cooperative networks under line of sight (LoS) conditions and non LoS conditions respectively. In [80], LCR and AFD expressions are developed for non-isotropic M2M Ricean channels.

In this chapter we use our M2M channel model discussed in Chapter 3, based on free-space wave propagation, where the scattering environment surrounding the transmitter and the receiver is characterized using a random scattering gain, which is a function of angle of arrival (AoA) and angle of departure (AoD) to derive and simulate LCR and AFD. We discuss second order statistics of Rice, Rayleigh and Nakagami fading channels for four different non-isotropic scattering environments, namely, Truncated Gaussian distribution and von-Mises distribution under separable channels and Truncated Gaussian bivariate distribution and Truncated Laplacian distribution under non separable channels. Rayleigh fading is a special case of both Rice and Nakagami fading. Unlike previous analysis of LCR and AFD for M2M channels, our analysis in this chapter covers Rayleigh and Nakagami environments in addition to Rice environment for the first time in the literature.

6.2 Second-Order Channel Statistics

6.2.1 Moments of Channel Temporal Correlation Function

To calculate LCR and AFD of a channel we need to derive expressions for the zeroth, first and second moments of the channel temporal correlation function $\Phi(\tau)$. We define the n^{th} moment of the channel temporal correlation function as [81]

$$b_n = \frac{1}{i^n} \frac{d^n \Phi(\tau)}{d\tau^n}\bigg|_{\tau=0}. \tag{6.1}$$

Two Dimensional (2D) Case

For 2D general scattering environments, the temporal correlation function of the M2M channel, as given in (4.16) ,

$$\Phi(\tau) \cong \sum_{m=-M_T}^{M_T} \sum_{n=-M_R}^{M_R} \beta_m^n J_m(ku\tau) J_n(kv\tau) e^{-im(\phi_u+\pi/2)} e^{in(\phi_v+\pi/2)}. \tag{6.2}$$

From (6.1), the zeroth moment of (6.2) can be written as

$$b_0 = \frac{1}{i^0} \frac{d^0\Phi(\tau)}{d\tau^0}\bigg|_{\tau=0} = \Phi(0) = \beta_0^0. \tag{6.3}$$

Theorem 1: The first moment of the 2D general channel temporal correlation function, b_1, can be expressed as:

$$b_1 = \frac{kv}{2}(\beta_0^1 e^{i\phi_v} - \beta_0^{-1} e^{-i\phi_v}) + \frac{ku}{2}(\beta_1^0 e^{-i\phi_u} - \beta_{-1}^0 e^{i\phi_u}), \tag{6.4}$$

for which, the proof is given in Appendix A.1.

Theorem 2: The expression for second moment of the 2D general channel temporal correlation function, b_2, is given as

$$\begin{aligned} b_2 =& \frac{k^2v^2}{4}(\beta_0^2 e^{i2\phi_v} + 2\beta_0^0 + \beta_0^{-2} e^{-i2\phi_v}) + \frac{k^2u^2}{4}(\beta_2^0 e^{-i2\phi_u} + 2\beta_0^0 + \beta_{-2}^0 e^{i2\phi_u}) \\ &+ \frac{k^2uv}{4}(\beta_1^1 e^{i(\phi_v-\phi_u)} - \beta_1^{-1} e^{-i(\phi_v+\phi_u)} - \beta_{-1}^1 e^{i(\phi_v+\phi_u)} + \beta_{-1}^{-1} e^{i(\phi_u-\phi_v)}). \end{aligned} \tag{6.5}$$

The proof is detailed in Appendix A.2.

For 2D isotropic scattering environments, the coefficients of the joint angular power distributions are given in Subsection 4.4.1, where $\beta_0^0 = 1$ and all other $\beta_m^n = 0$;

Applying these values to (6.3), (6.4) and (6.5), $b_0 = 1$, $b_1 = 0$ and $b_2 = \frac{k^2(u^2+v^2)}{2}$. In a similar manner, the coefficients for 2D non-isotropic scattering environments also can be derived.

3D Case

For 3D general scattering environments, the temporal correlation function of the M2M channel, as given in (4.26),

$$\Phi(\tau) = (4\pi)^2 \sum_{n=0}^{\infty} \sum_{m=-n}^{n} e^{-in\pi/2} j_n(ku\tau) Y_{nm}(\widehat{\boldsymbol{u}}) \sum_{p=0}^{\infty} \sum_{q=-p}^{p} e^{ip\pi/2} j_p(kv\tau) Y_{pq}^*(\widehat{\boldsymbol{v}}) \beta_{n,m}^{p,q}. \tag{6.6}$$

From (6.1), the zeroth moment of (6.6) can be written as

$$b_0 = \frac{1}{i^0} \frac{d^0\Phi(\tau)}{d\tau^0}\bigg|_{\tau=0} = \Phi(0) = (4\pi)^2 Y_{00}(\widehat{\boldsymbol{u}}) Y_{00}^*(\widehat{\boldsymbol{v}}) \beta_{0,0}^{0,0} = 4\pi \beta_{0,0}^{0,0} \tag{6.7}$$

Theorem 3: We simplify b_1 in Appendix A.3 to obtain

$$\begin{aligned} b_1 = &- \frac{1}{i}(4\pi)^2 (e^{-i\pi/2} \frac{ku}{3} Y_{00}^*(\widehat{\boldsymbol{v}}) [Y_{1-1}(\widehat{\boldsymbol{u}}) \beta_{1,-1}^{0,0} + Y_{10}(\widehat{\boldsymbol{u}}) \beta_{1,0}^{0,0} + Y_{11}(\widehat{\boldsymbol{u}}) \beta_{1,1}^{0,0}] \\ &+ \frac{kv}{3} Y_{00}(\widehat{\boldsymbol{u}}) [e^{-i\pi/2} Y_{1-1}^*(\widehat{\boldsymbol{v}}) \beta_{0,0}^{1,-1} + Y_{10}^*(\widehat{\boldsymbol{v}}) \beta_{0,0}^{1,0} + e^{i\pi/2} Y_{11}^*(\widehat{\boldsymbol{v}}) \beta_{0,0}^{1,1}]). \end{aligned} \tag{6.8}$$

Theorem 4: Similarly we simplify b_2 in Appendix A.4 to obtain

$$\begin{aligned} b_2 = &- (4\pi)^2 (\frac{2k^2u^2e^{-i\pi}}{15} Y_{00}^*(\widehat{\boldsymbol{v}}) \sum_{m=-2}^{2} Y_{2m}(\widehat{\boldsymbol{u}}) \beta_{2,m}^{0,0} - \frac{k^2u^2}{3} Y_{00}(\widehat{\boldsymbol{u}}) Y_{00}^*(\widehat{\boldsymbol{v}}) \beta_{0,0}^{0,0} \\ &+ \frac{2k^2uv}{9} \sum_{m=-1}^{1} Y_{1m}(\widehat{\boldsymbol{u}}) \sum_{q=-1}^{1} Y_{1q}^*(\widehat{\boldsymbol{v}}) \beta_{1,m}^{1,q} \\ &+ \frac{2k^2v^2e^{i\pi}}{15} Y_{00}(\widehat{\boldsymbol{u}}) \sum_{q=-2}^{2} Y_{2q}^*(\widehat{\boldsymbol{v}}) \beta_{0,0}^{2,q} - \frac{k^2v^2}{3} Y_{00}(\widehat{\boldsymbol{u}}) Y_{00}^*(\widehat{\boldsymbol{v}}) \beta_{0,0}^{0,0}). \end{aligned} \tag{6.9}$$

For 3D isotropic scattering environments, the coefficients of the joint angular power distributions are given in Subsection 4.5.1, where $\beta_{0,0}^{0,0} = 1$ and all other $\beta_{n,m}^{p,q} = 0$; Applying these values to (6.7), (6.8) and (6.9), $b_0 = 1$, $b_1 = 0$ and $b_2 = \frac{k^2(u^2+v^2)}{3}$.

6.2.2 Level Crossing Rate

The LCR, mathematically denoted as N_R, is defined as the expected rate at which the envelope, r, crosses a specified signal level, R, in the positive direction and is given by [82]

$$N_R = \int_0^\infty \dot{r} p(R, \dot{r})\, d\dot{r}, \tag{6.10}$$

where $\dot{r}$ indicates the time derivative of r and $p(R, \dot{r})$ is the joint density function of r and $\dot{r}$ at $r = R$.

The expressions for N_R in Rayleigh [83], Rice [81], and Nakagami [84] models are as follows:

$$N_{\text{Rayleigh}}(\rho) = \sqrt{\frac{b_2}{b_0} - \frac{b_1^2}{b_0^2}} \cdot \frac{\rho e^{-\rho^2}}{\sqrt{\pi}}, \tag{6.11}$$

where $\rho = R/\sqrt{2b_0} = R/R_{rms}$ is the normalized envelope level and b_n is the n^{th} moment of the channel temporal correlation function (denoted by $\Phi(\tau)$) of the fading envelope, and given by

$$b_n = \frac{1}{j^n} \frac{d^n}{d\tau^n} \Phi(\tau) \bigg|_{\tau=0}. \tag{6.12}$$

For Rice [81] we have

$$\begin{aligned} N_{\text{Rice}}(\rho) = & \sqrt{\frac{b_2}{b_0} - \frac{b_1^2}{b_0^2}} \cdot \frac{2\sqrt{K+1}}{\pi^{3/2}} \cdot \rho e^{-K-(K+1)\rho^2} \\ & \times \int_0^{\pi/2} \cosh(2\sqrt{K(K+1)}\rho \cos\theta) \\ & \times [e^{-\chi^2 \sin^2\theta} + \sqrt{\pi}\chi \sin(\theta) \text{erf}(\chi \sin\theta)] d\theta, \end{aligned} \tag{6.13}$$

where $\cosh(\cdot)$ is the hyperbolic cosine function, $\text{erf}(\cdot)$ is the error function,

$$\text{erf}(z) = 2\pi^{-1/2} \int_0^z \exp(-u^2) du, \tag{6.14}$$

and the parameter $\chi = \sqrt{Kb_1^2/(b_0 b_2 - b_1^2)}$.

Rayleigh and Rice distributions efficiently describe the multipath propagation in wireless communication under non LoS and LoS conditions, respectively. The symbol K designates the Ricean factor (ratio of the LoS component power to the diffuse component power). When K is increased, the ratio of Los power to scatter power increased while the fluctuation range of the received signal shrinks.

Finally, for Nakagami [84]

$$N_{\text{Nakagami}}(\rho) = \sqrt{\frac{b_2}{b_0}} \cdot \frac{(m\rho^2)^{m-(1/2)} e^{-m\rho^2}}{\sqrt{2\pi}\Gamma(m)}, \tag{6.15}$$

where $\Gamma(\cdot)$ is the gamma function and m is the shape parameter.

6.2.3 Average Fade Duration

The average fade duration is the time the envelope r spends below some specified value R, which is given by [82]

$$\overline{r} = \frac{p(r < R)}{N_R}, \tag{6.16}$$

where $p(r < R)$ means the cumulative distribution function (CDF) of the given fading model. The CDFs of Rayleigh, Rice and Nakagami models can be written in terms of normalized envelope level, ρ as:

$$F_{\text{Rayleigh}}(\rho) = 1 - e^{-\rho^2}, \tag{6.17}$$

$$F_{\text{Rice}}(\rho) = 1 - Q(\sqrt{2K}, \sqrt{2(K+1)\rho^2}), \tag{6.18}$$

$$F_{\text{Nakagami}}(\rho) = \frac{\Gamma(m, m\rho^2)}{\Gamma(m)}, \tag{6.19}$$

where $Q(\cdot,\cdot)$ and $\Gamma(\cdot,\cdot)$ are the Marcum-Q and incomplete gamma functions, respectively. According to (6.16), AFD of Rayleigh, Rice and Nakagami models can be found using relevant CDFs and LCRs.

For M2M channel in 2D isotropic scattering environment, substituting $b_0 = 1$, $b_1 = 0$, and $b_2 = k^2(u^2 + v^2)/2$ as detailed in Section 6.2.1 to (6.11), (6.13) and (6.15), we derive LCR for relevant models and similarly, derive AFD for all three models. Final closed form expressions of LCRs and AFDs for M2M channel in 2D isotropic scattering environments are summarized in Table 6.1.

In a similar manner, for M2M channel in 3D isotropic scattering environment substituting $b_0 = 1$, $b_1 = 0$, and $b_2 = k^2(u^2 + v^2)/3$, given in Section 6.2.1, we derive LCR and AFD for all three models. Final closed form expressions of LCRs and AFDs M2M channel in 3D isotropic scattering environment are summarized in Table 6.2.

6.3 Simulations

In this chapter, we present two simulation results to corroborate the equations defined in Table 6.1, which could be extended to all other equations with different parameters in a similar manner. To compare LCR, we have used Rayleigh fading channels with 2D isotropic, 2D non-isotropic separable Gaussian, separable von-Mises, non separable Gaussian and non separable Laplacian. In a similar manner, for the comparison of AFD, we have used Nakagami fading channels with 2D isotropic, 2D non-isotropic separable Gaussian, separable von-Mises, non separable Gaussian and non separable Laplacian.

In all the simulations, we have used carrier frequency as 2.435 GHz, transmitter velocity as 10 m/s, receiver velocity as 10 m/s, maximum Doppler frequencies (transmitter and receiver) as 90.86 Hz and Nakagami fading channel fading parameter as 0.65.

In analyzing Fig. 6.1, LCR for Rayleigh fading channels, it shows that non-isotropic case is better than isotropic as the LCR is lower for non-isotropic than isotropic. Further, we note that while Gaussian separable and non separable results are more closer to 2D isotropic, separable von-Mises shows the best results compared to all other scattering environments, as it always has low LCR values with the given parameters. In addition, we experienced similar results in terms of AFD for Nakagami fading channels as shown in Fig. 6.2.

As seen in Fig. 6.3, LCR values are lower in 3D than in 2D under all the fading

Table 6.1: M2M 2D isotropic scattering environment LCR and AFD equations

	Rayleigh Model	Rice Model	Nakagami Model
LCR	$\sqrt{\frac{u^2+v^2}{2\pi}} \cdot k\rho e^{-\rho^2}$	$\sqrt{\frac{(K+1)(u^2+v^2)}{2\pi}} \cdot k\rho e^{-K-(K+1)\rho^2} \cdot J_0(2j\rho\sqrt{K(K+1)})$	$\sqrt{\frac{u^2+v^2}{4\pi}} \cdot \frac{k(m\rho^2)^{m-(1/2)}e^{-m\rho^2}}{\Gamma(m)}$
AFD	$\sqrt{\frac{2\pi}{u^2+v^2}} \cdot \frac{(e^{\rho^2}-1)}{k\rho}$	$\sqrt{\frac{2\pi}{(K+1)(u^2+v^2)}} \cdot \frac{(1-Q(\sqrt{2K},\sqrt{2(K+1)\rho^2}))}{J_0(j\cdot 2\rho\sqrt{K(K+1)})} \cdot \frac{e^{K+(K+1)\rho^2}}{k\rho}$	$\sqrt{\frac{4\pi}{u^2+v^2}} \cdot \frac{\Gamma(m,m\rho^2)}{k(m\rho^2)^{m-(1/2)}e^{-m\rho^2}}$

Table 6.2: M2M 3D isotropic scattering environment LCR and AFD equations

	Rayleigh Model	Rice Model	Nakagami Model
LCR	$\sqrt{\frac{u^2+v^2}{3\pi}} \cdot k\rho e^{-\rho^2}$	$\sqrt{\frac{(K+1)(u^2+v^2)}{3\pi}} \cdot k\rho e^{-K-(K+1)\rho^2} \cdot J_0(2j\rho\sqrt{K(K+1)})$	$\sqrt{\frac{u^2+v^2}{6\pi}} \cdot \frac{k(m\rho^2)^{m-(1/2)}e^{-m\rho^2}}{\Gamma(m)}$
AFD	$\sqrt{\frac{3\pi}{u^2+v^2}} \cdot \frac{(e^{\rho^2}-1)}{k\rho}$	$\sqrt{\frac{3\pi}{(K+1)(u^2+v^2)}} \cdot \frac{(1-Q(\sqrt{2K},\sqrt{2(K+1)\rho^2}))}{J_0(j\cdot 2\rho\sqrt{K(K+1)})} \cdot \frac{e^{K+(K+1)\rho^2}}{k\rho}$	$\sqrt{\frac{6\pi}{u^2+v^2}} \cdot \frac{\Gamma(m,m\rho^2)}{k(m\rho^2)^{m-(1/2)}e^{-m\rho^2}}$

channels considered, namely Rice, Rayleigh and Nakagami. Similar results are observed in Fig. 6.4 for AFD which evidence better results for 3D than 2D.

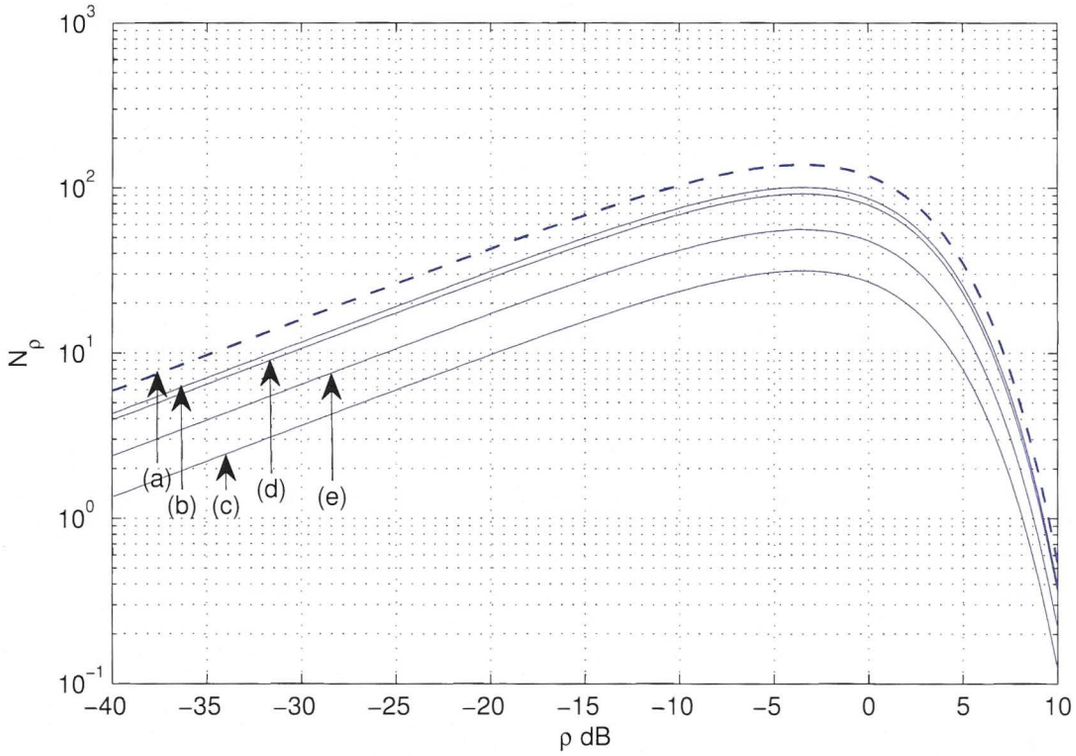

Figure 6.1: LCR in Rayleigh environment when scattering is (a) 2D isotropic (b) Separable Gaussian (c) Separable von-Mises (d) Non separable Gaussian (e) Non separable Laplacian.

6.4 Experimental Validations

For experimental validation, we used the data collected in two urban locations, around Georgia Tech and Atlanta GA [76] and highway in Germany [39]. The details of the settings for the urban locations and highway in Germany are summarized in Table 6.3.

The graphs in Fig. 6.5 and Fig. 6.6 compare the simulated LCR and AFD with the measured LCR and AFD taken from Fig 2(a) and 3(a) of [76], relevant to urban area M2M channel model. For our simulations we used the same parameters as used in [76] and average Rice factor, $K = 2.43$. As this experimental environment

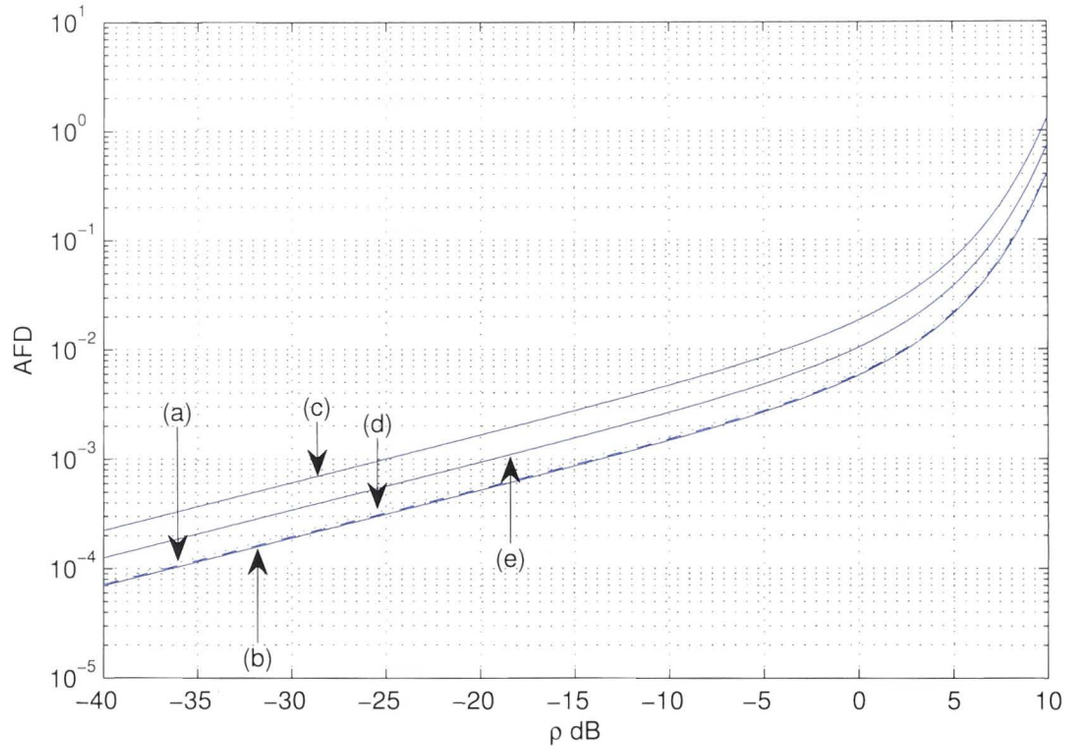

Figure 6.2: AFD in Nakagami environment when scattering is (a) 2D isotropic (b) Separable Gaussian (c) Separable von-Mises (d) Non separable Gaussian (e) Non separable Laplacian.

represents Rice model which means that receiver gets a part of the transmitter signal directly, measured data exactly tallies with Rice model simulation.

In Fig. 6.7 and Fig. 6.8, we compare the simulated LCR and AFD with the measured LCR and AFD taken from Fig 8 of [39] relevant in highway M2M channel model. The same parameters are used in our simulation as in experiments and average Rice factor, $K = 1.73$. As in urban environment, this highway experimental environment also represents Rice model which means receiver receives line of sight portion of transmitter signal directly. Hence our Rice model simulations closely fit to the experimental data results.

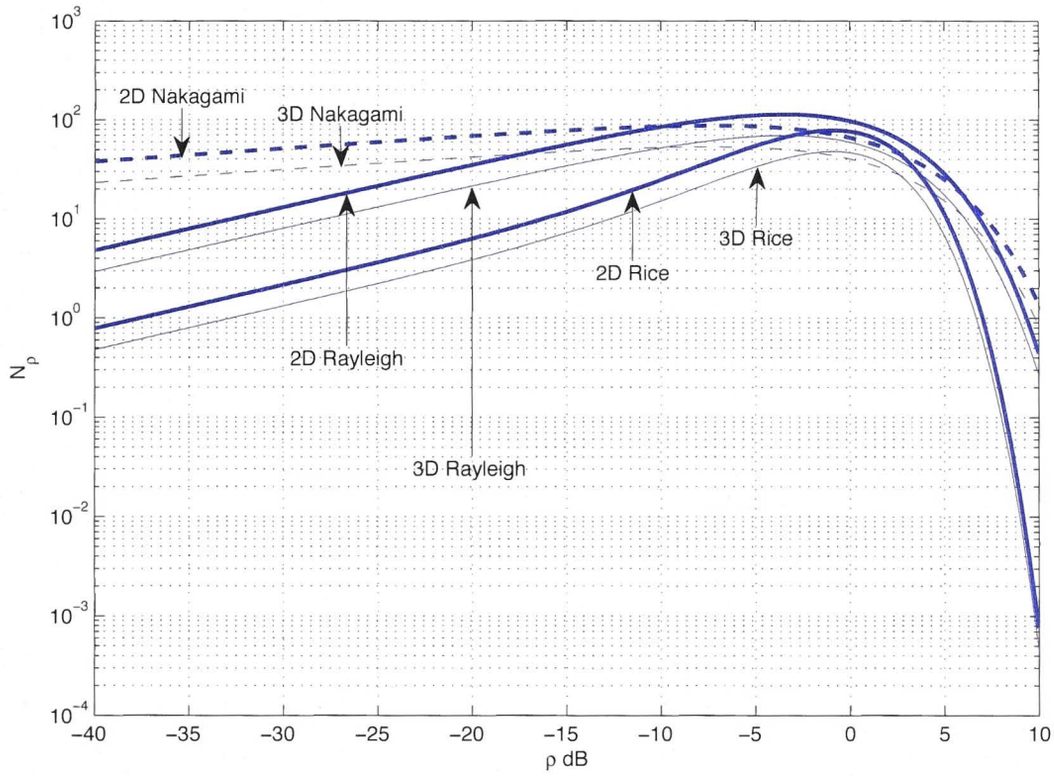

Figure 6.3: (1)LCR in 2D Isotropic M2M environments (2)LCR in 3D Isotropic M2M environments.

6.5 Contributions and Conclusions

In this chapter, using underlying physics of wave propagation in free-space, we have analyzed second order statistics such as LCR and AFD of M2M channels under isotropic and non-isotropic scattering environments. The derived formulas can be used for any practical M2M communication applications to analyze AFD and LCR and thereby to be used for channel parameter design/selection criteria such as choosing the frame length of coded packetized systems, interleaver optimization, efficiently combatting the burst of errors due to long fades and etc. In addition, using our 3D M2M channel model, closed form expressions of level crossing rate and average fade duration for Rayleigh, Rice and Nakagami models are derived. Comparisons of 3D with 2D simulation results show 3D results are better than 2D in all the times. These LCR and AFD expressions can be used to analyze the impacts due to transmitter or receiver velocities in different fading models. The

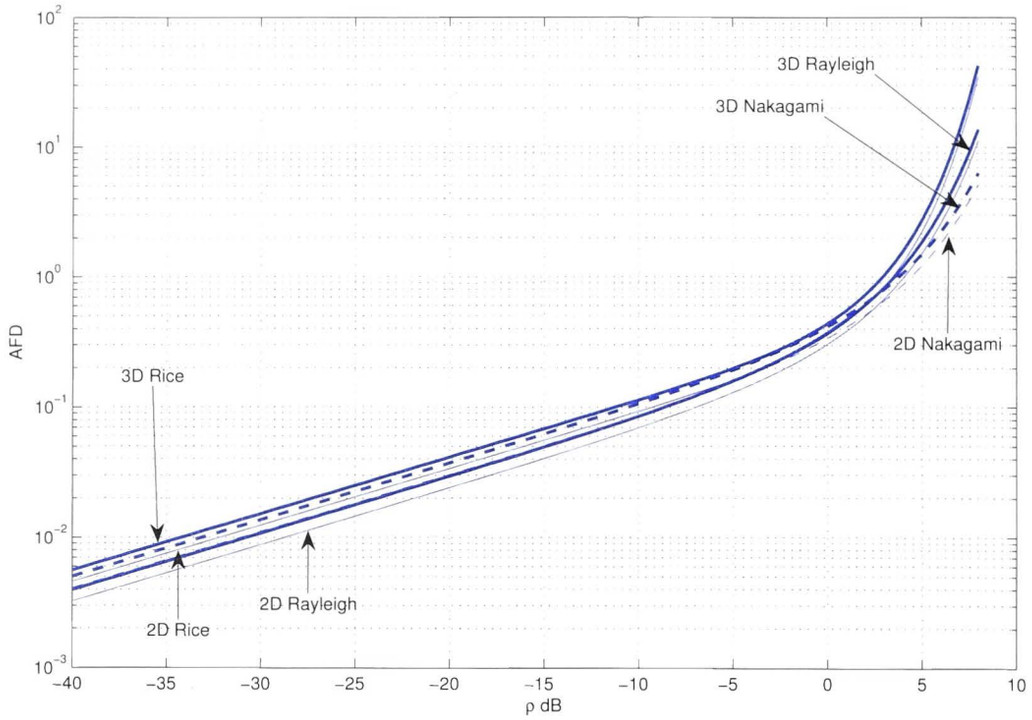

Figure 6.4: (1)AFD in 2D Isotropic M2M environments (2)AFD in 3D Isotropic M2M environments.

simulation results corroborate the experimental data perfectly which are discussed in Section 6.4.

Table 6.3: Experimental settings

	Georgia Tech, Atlanta	**Germany Highway**
Channel measurements	Wideband at 2.435GHz	Narrowband at 5.2GHz
Maximum Doppler frequencies	$f_{\mathrm{Tmax}} = f_{\mathrm{Rmax}}$ 90.86Hz	$f_{\mathrm{Tmax}} = f_{\mathrm{Rmax}}$ 500Hz
Distance between T_x and R_x	$D = 300m$	$D = 300m$
Moving directions of T_x and R_x	$\gamma_T = \gamma_R$ 0	$\gamma_T = \gamma_R$ 0 (assumed)
Antennas of T_x and R_x	Omnidirectional with $\Delta_H = 0$	Omnidirectional with $\Delta_H = 0$

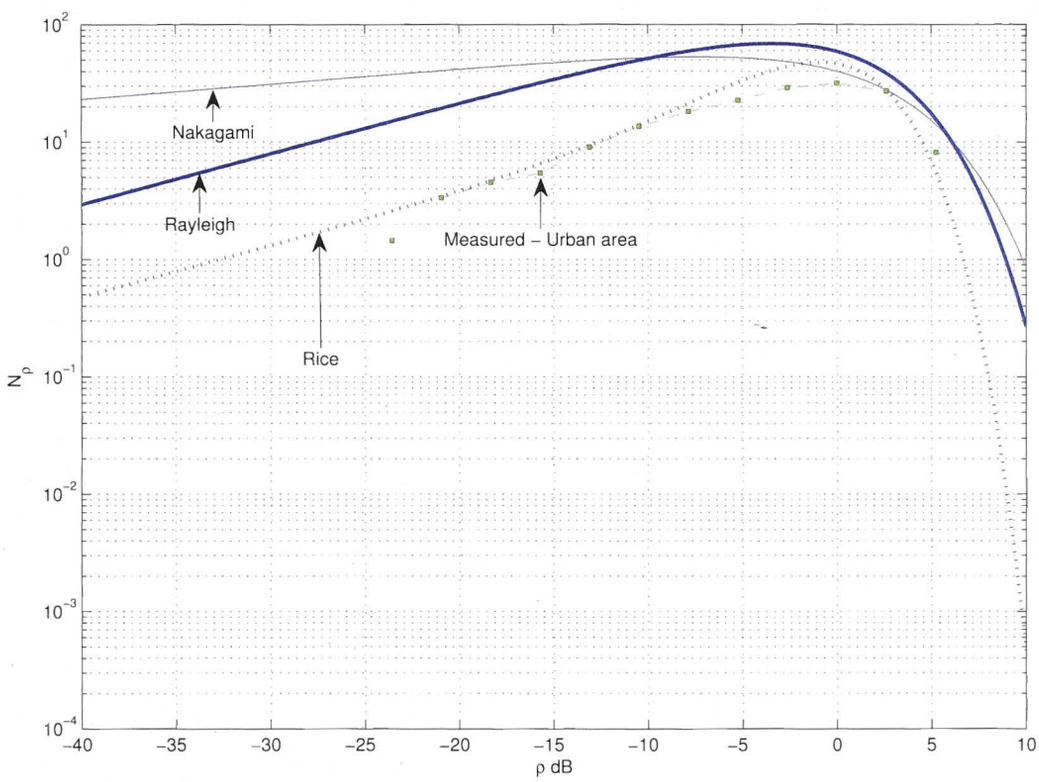

Figure 6.5: LCR in 2D isotropic M2M Rayleigh, Rice, Nakagami distributed environments and measured in urban area environment.

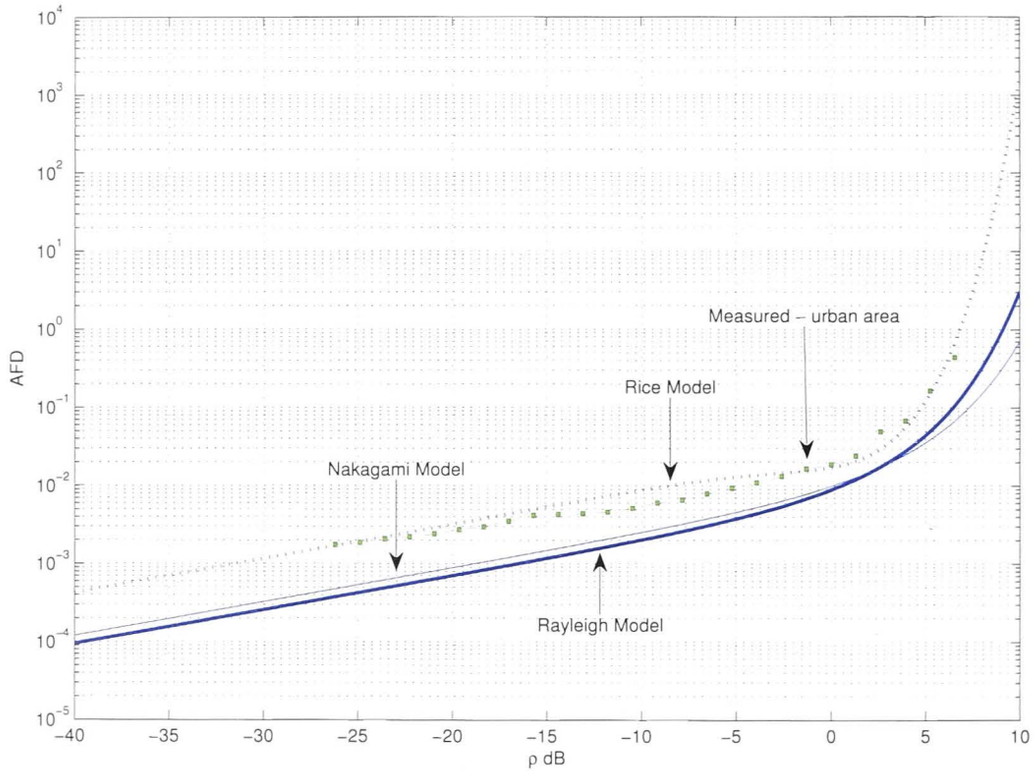

Figure 6.6: AFD in 2D isotropic M2M Rayleigh, Rice, Nakagami distributed environments and measured in urban area environment.

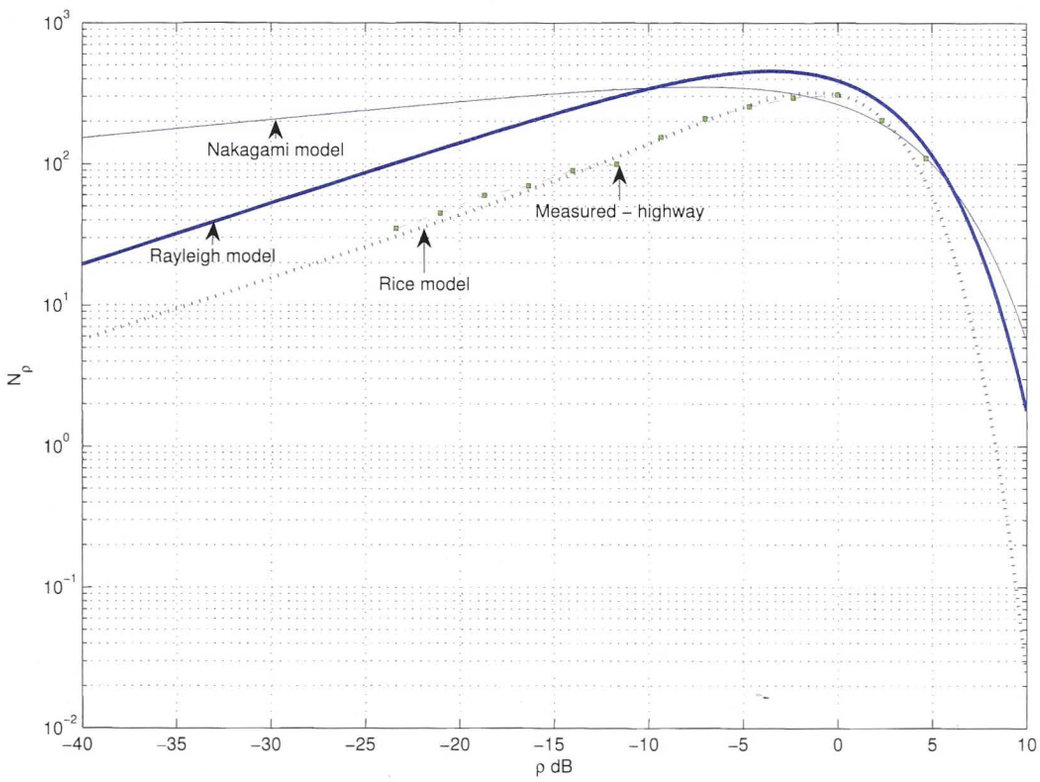

Figure 6.7: LCR in 2D isotropic M2M Rayleigh, Rice, Nakagami distributed environments and measured on a highway.

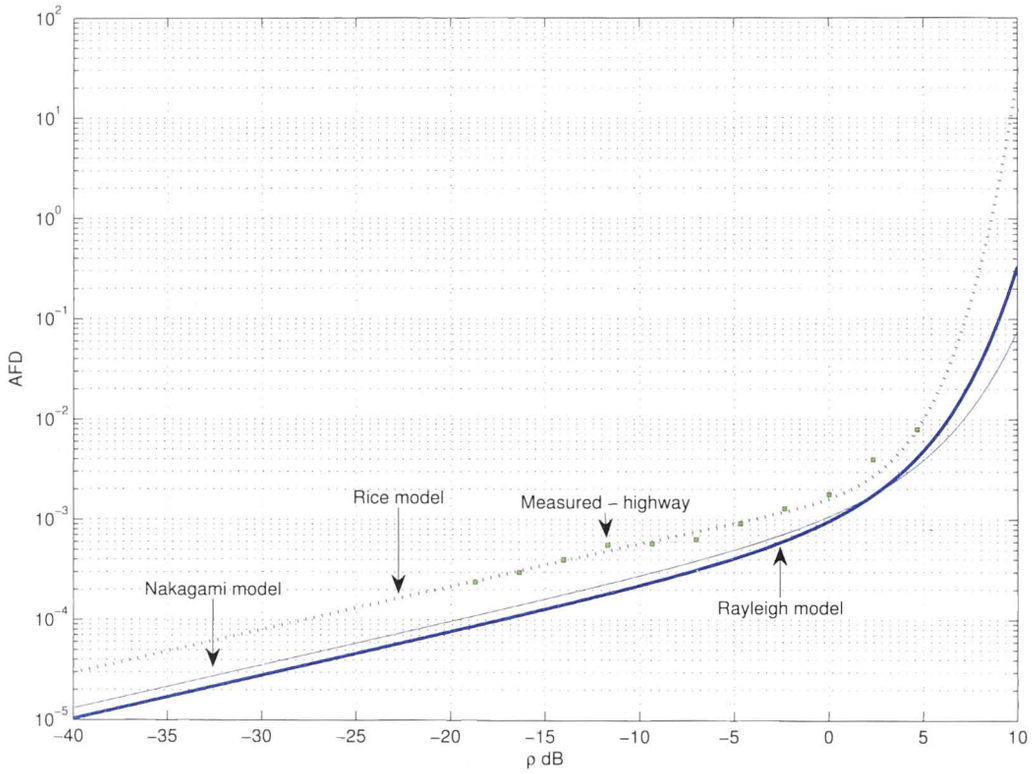

Figure 6.8: AFD in 2D isotropic M2M Rayleigh, Rice, Nakagami distributed environments and measured on a highway.

Chapter 7

Conclusions and Future Work

In this final chapter, we summarize the key findings of our research and general conclusions drawn from the thesis. Further, few future research directions arising out of this research are proposed.

7.1 Conclusions

As mentioned in Chapter 2, though mobile to mobile (M2M) systems are promising in catering the communication requirements in the future, the amount of research dedicated towards facing the challenges of the time-varying nature of the M2M fading channel in the literature is very sparse. In filling this gap, we have delivered few major contributions in our research and the conclusions drawn are summarized in this section.

The major contribution of our research is the introduction of the novel M2M channel model for 2D and 3D scattering environments, which can be used as a framework for any scattering environment by selecting suitable complex scattering gain functions. This channel model is the only mathematical non geometrical stochastic M2M channel model available so far. Further, we extend this novel model to multicarrier M2M which is the first multicarrier channel model in non geometrical stochastic M2M category.

We analyze in detail space-time correlation and space-frequency correlation of received signals in our novel M2M channel model specially with transmitter and

receiver velocities. The impact of transmitter and receiver velocities on correlation in M2M channel models has not been addressed in the literature and we fill this gap with our analysis. The simulation results verify that correlation reduces when transmitter or receiver velocity increases in space-time correlation and the rate of reduction in von Mises-Fisher distribution scattering environment is more than the isotropic environment.

In addition, we analyze second order statistics of our novel M2M channel model and compare with available experimental results. This analysis confirm that our mathematical model perfectly verifies the experimental results.

7.2 Suggested Future Work

Although our research in this thesis was able to contribute and provide valuable insights into M2M channel modeling, there are many outstanding problems yet to be answered. In this section we outline few of them.

Experimental results – Lack of channel measurement capabilities has limited our contributions to propose M2M channel models and carry out related analysis. We could verify only for second order statistics of M2M channel with existing experimental values in the literature where the results are discussed in Chapter 6. Those experimental values were not enough for a complete verification of our novel channel model where more meaningful and relevant measurement data is needed. Thus, we suggest that future research should be directed to introduce more measurement campaigns which would help in identifying and developing correct channel models comparing accuracy and complexity of each model.

Velocity Estimator/determine the velocity of the mobile terminals – It is shown in [85] that the estimation of the velocity of the mobile unit of F2M will improve the design of handoff algorithms, cell architectures and dynamic channel assignments. This can be more effective if applied in M2M systems but only one recent paper [86] discusses about M2M velocity estimator. Few of F2M estimation methods are zero-crossing rate (ZCR) of the inphase or

quadrature phase components [87], the rate of maxima (ROM) of the received signal [88], spectral moment expression of the received signal [85], the spectral moments of the in-phase and quadrature phase components [89] and the usage of Doppler processing of a signal received from a single antenna [90]. A potential research area would be to take our novel channel model as the base and identify the estimation methods for mobile units in M2M environments.

Impact of moving scatterers – In this thesis one of the main assumptions is the stationarity of the scatterers. But in real environment due to the low elevation of the transmitter and receiver, the scatterers are non-stationary. Therefore our novel channel model and its analysis can be extended to incorporate the non-stationary property of the scatterers. For this, [91] can be taken as a guideline which is the only paper published in the literature in this regard.

Single model for relay networks – As mentioned in Chapter 1, relays in wireless networks consist of a cascade of F2M and M2M links. Due to the combination of F2M and M2M, relay channels do not resemble the properties of either M2M or F2M channels. As the M2M novel channel model introduced in this thesis is based on the F2M model in [57], by combining these two models, a novel relay channel model can be introduced and investigated.

Appendix A

A.1 Proof of Theorem 1

The first moment of the two dimensional (2D) general channel temporal correlation function, b_1, can be expressed as

$$b_1 = \frac{1}{j^1}\frac{d^1\Phi(\tau)}{d\tau^1}\bigg|_{\tau=0} = \frac{1}{j}\Phi'(\tau)\bigg|_{\tau=0}. \tag{A.1}$$

By substituting $\Phi(\tau)$ from (6.2),

$$b_1 = \frac{1}{j}\sum_{m=-M_T}^{M_T}\sum_{n=-M_R}^{M_R}\frac{d}{d\tau}(\beta_m^n J_m(ku\tau)J_n(kv\tau)e^{-im(\phi_u+\pi/2)}e^{in(\phi_v+\pi/2)})\bigg|_{\tau=0}. \tag{A.2}$$

Using the following properties of Bessel function to simplify (A.2)

$$J_v'(z) = -J_{v+1}(z) + \frac{v}{z}J_v(z), \tag{A.3}$$

$$J_v'(z) = J_{v-1}(z) - \frac{v}{z}J_v(z), \tag{A.4}$$

$$2J_v'(z) = J_{v-1}(z) - J_{v+1}(z), \tag{A.5}$$

results in

$$b_1 = \frac{1}{j}\sum_{m=-M_T}^{M_T}\sum_{n=-M_R}^{M_R}\beta_m^n(\frac{kv}{2}J_m(ku\tau)(J_{n-1}(kv\tau) - J_{n+1}(kv\tau)) + \frac{ku}{2}J_n(kv\tau)(J_{m-1}(ku\tau) - J_{m+1}(ku\tau)))$$

$$\times\, e^{-im(\phi_u+\pi/2)} e^{in(\phi_v+\pi/2)} \Big|_{\tau=0}.$$

Simplifying further with $\tau = 0$,

$$b_1 = \frac{kv}{2j}(\beta_0^1 e^{i(\phi_v+\pi/2)} - \beta_0^{-1} e^{-i(\phi_v+\pi/2)}) + \frac{ku}{2j}(\beta_1^0 e^{-i(\phi_u+\pi/2)} - \beta_{-1}^0 e^{i(\phi_u+\pi/2)}).$$

Finally,

$$b_1 = \frac{kv}{2}(\beta_0^1 e^{i\phi_v} - \beta_0^{-1} e^{-i\phi_v}) + \frac{ku}{2}(\beta_1^0 e^{-i\phi_u} - \beta_{-1}^0 e^{i\phi_u}).$$

A.2 Proof of Theorem 2

Similar to the proof of Theorem 1, given in Appendix A, the second moment of the channel temporal correlation function for 2D general scattering environments can be written as

$$b_2 = \frac{1}{j^2}\frac{d^2\Phi(\tau)}{d\tau^2}\Big|_{\tau=0} = -\Phi''(\tau)\Big|_{\tau=0},$$

By substituting $\Phi(\tau)$ from (6.2),

$$b_2 = -\sum_{m=-M_T}^{M_T}\sum_{n=-M_R}^{M_R} \frac{d^2}{d\tau^2}(\beta_m^n J_m(ku\tau) J_n(kv\tau) e^{-im(\phi_u+\pi/2)} e^{in(\phi_v+\pi/2)})\Big|_{\tau=0}.$$

Using (A.3), (A.4) and (A.5),

$$\begin{aligned} b_2 = -\sum_{m=-M_T}^{M_T}\sum_{n=-M_R}^{M_R} \beta_m^n \frac{d}{d\tau}\Big(&\frac{kv}{2} J_m(ku\tau)(J_{n-1}(kv\tau) - J_{n+1}(kv\tau)) \\ &+ \frac{ku}{2} J_n(kv\tau)(J_{m-1}(ku\tau) - J_{m+1}(ku\tau))\Big) e^{-im(\phi_u+\pi/2)} e^{in(\phi_v+\pi/2)}\Big|_{\tau=0}. \end{aligned}$$

Simplifying further with $\tau = 0$,

$$b_2 = -\sum_{m=-M_T}^{M_T}\sum_{n=-M_R}^{M_R}\beta_m^n\Big(\frac{k^2v^2}{4}J_m(0)(J_{n-2}(0)-2J_n(0)+J_{n+2}(0)) + \frac{k^2u^2}{4}J_n(0)(J_{m-2}(0)-2J_m(0)+J_{m+2}(0)) + \frac{k^2uv}{4}(J_{n-1}(0)-J_{n+1}(0))(J_{m-1}(0)-J_{m+1}(0))\Big)e^{-im(\phi_u+\pi/2)}e^{in(\phi_v+\pi/2)},$$

resulting in

$$b_2 = \frac{k^2v^2}{4}(\beta_0^2e^{i2\phi_v}+2\beta_0^0+\beta_0^{-2}e^{-i2\phi_v}) + \frac{k^2u^2}{4}(\beta_2^0e^{-i2\phi_u}+2\beta_0^0+\beta_{-2}^0e^{i2\phi_u}) + \frac{k^2uv}{4}(\beta_1^1e^{i(\phi_v-\phi_u)}-\beta_1^{-1}e^{-i(\phi_v+\phi_u)}-\beta_{-1}^1e^{i(\phi_v+\phi_u)}+\beta_{-1}^{-1}e^{i(\phi_u-\phi_v)}). \quad \text{(A.6)}$$

A.3 Proof of Theorem 3

The first moment of the channel temporal correlation function for 3D general scattering environments can be written as

$$b_1 = \frac{1}{j^1}\frac{d^1\Phi(\tau)}{d\tau^1}\bigg|_{\tau=0} = \frac{1}{j}\Phi'(\tau)\bigg|_{\tau=0},$$

By substituting $\Phi(\tau)$ from (6.6),

$$b_1 = \frac{1}{j}\frac{d((4\pi)^2\sum_{n=0}^{\infty}\sum_{m=-n}^{n}e^{-in\pi/2}j_n(ku\tau)Y_{nm}(\widehat{\boldsymbol{u}})\sum_{p=0}^{\infty}\sum_{q=-p}^{p}e^{ip\pi/2}j_p(kv\tau)Y_{pq}^*(\widehat{\boldsymbol{v}})\beta_{n,m}^{p,q}}{d\tau} \quad \text{(A.7)}$$

Using the following property to simplify (A.7),

$$\frac{(2n+1)}{k}\frac{dj_n(kx)}{dx} = nj_{n-1}(kx)-(n+1)j_{n+1}(kx) \quad \text{(A.8)}$$

results in

$$b_1 = -\frac{1}{j}(4\pi)^2\Big(\sum_{n=0}^{\infty}\sum_{m=-n}^{n} e^{-in\pi/2}\frac{ku}{2n+1}(nj_{n-1}(ku\tau) - (n+1)j_{n+1}(ku\tau))Y_{nm}(\widehat{\boldsymbol{u}})\sum_{p=0}^{\infty}\sum_{q=-p}^{p} e^{ip\pi/2}j_p(kv\tau)Y_{pq}^*(\widehat{\boldsymbol{v}})\beta_{n,m}^{p,q} + \sum_{n=0}^{\infty}\sum_{m=-n}^{n} e^{-in\pi/2}j_n(ku\tau)Y_{nm}(\widehat{\boldsymbol{u}})\sum_{p=0}^{\infty}\sum_{q=-p}^{p} e^{ip\pi/2}\frac{kv}{2p+1}(pj_{p-1}(kv\tau) - (p+1)j_{p+1}(kv\tau))Y_{pq}^*(\widehat{\boldsymbol{v}})\beta_{n,m}^{p,q}\Big)\Big|_{\tau=0}.$$

Finally,

$$b_1 = -\frac{1}{j}(4\pi)^2\Big(e^{-i\pi/2}\frac{ku}{3}Y_{00}^*(\widehat{\boldsymbol{v}})[Y_{1-1}(\widehat{\boldsymbol{u}})\beta_{1,-1}^{0,0} + Y_{10}(\widehat{\boldsymbol{u}})\beta_{1,0}^{0,0} + Y_{11}(\widehat{\boldsymbol{u}})\beta_{1,1}^{0,0}] + \frac{kv}{3}Y_{00}(\widehat{\boldsymbol{u}})[e^{-i\pi/2}Y_{1-1}^*(\widehat{\boldsymbol{v}})\beta_{0,0}^{1,-1} + Y_{10}^*(\widehat{\boldsymbol{v}})\beta_{0,0}^{1,0} + e^{i\pi/2}Y_{11}^*(\widehat{\boldsymbol{v}})\beta_{0,0}^{1,1}]\Big).$$

A.4 Proof of Theorem 4

The second moment of the channel temporal correlation function for 3D general scattering environments can be written as

$$b_2 = \frac{1}{j^2}\frac{d^2\Phi(\tau)}{d\tau^2}\Big|_{\tau=0} = -\Phi''(\tau)\Big|_{\tau=0}.$$

Using (A.8),

$$b_2 = \frac{1}{j^2}(4\pi)^2\Big(\sum_{n=0}^{\infty}\sum_{m=-n}^{n} e^{-in\pi/2}\frac{k^2u^2n((n-1)j_{n-2}(ku\tau) - nj_n(ku\tau))}{4n^2-1} \times Y_{nm}(\widehat{\boldsymbol{u}})\sum_{p=0}^{\infty}\sum_{q=-p}^{p} e^{ip\pi/2}j_p(kv\tau)Y_{pq}^*(\widehat{\boldsymbol{v}})\beta_{n,m}^{p,q} - \sum_{n=0}^{\infty}\sum_{m=-n}^{n} e^{-in\pi/2}\frac{k^2u^2(n+1)((n+1)j_n(ku\tau) - (n+2)j_{n+2}(ku\tau))}{(2n+1)(2n+3)}$$

$$
\begin{aligned}
&\times Y_{nm}(\widehat{\boldsymbol{u}}) \sum_{p=0}^{\infty} \sum_{q=-p}^{p} e^{ip\pi/2} j_p(kv\tau) Y_{pq}^*(\widehat{\boldsymbol{v}}) \beta_{n,m}^{p,q} \\
&+ \sum_{n=0}^{\infty} \sum_{m=-n}^{n} e^{-in\pi/2} \frac{ku(nj_{n-1}(ku\tau) - (n+1)j_{n+1}(ku\tau))}{2n+1} Y_{nm}(\widehat{\boldsymbol{u}}) \\
&\times \sum_{p=0}^{\infty} \sum_{q=-p}^{p} e^{ip\pi/2} \frac{kv(pj_{p-1}(kv\tau) - (p+1)j_{p+1}(kv\tau))}{2p+1} Y_{pq}^*(\widehat{\boldsymbol{v}}) \beta_{n,m}^{p,q} \\
&+ \sum_{n=0}^{\infty} \sum_{m=-n}^{n} e^{-in\pi/2} j_n(ku\tau) Y_{nm}(\widehat{\boldsymbol{u}}) \\
&\times \sum_{p=0}^{\infty} \sum_{q=-p}^{p} e^{ip\pi/2} \frac{k^2v^2p((p-1)j_{p-2}(kv\tau) - pj_p(kv\tau))}{4p^2-1} Y_{pq}^*(\widehat{\boldsymbol{v}}) \beta_{n,m}^{p,q} \\
&- \sum_{n=0}^{\infty} \sum_{m=-n}^{n} e^{-in\pi/2} j_n(ku\tau) Y_{nm}(\widehat{\boldsymbol{u}}) \\
&\times \sum_{p=0}^{\infty} \sum_{q=-p}^{p} e^{ip\pi/2} \frac{k^2v^2(p+1)((p+1)j_p(kv\tau) - (p+2)j_{p+2}(kv\tau))}{(2p+1)(2p+3)} Y_{pq}^*(\widehat{\boldsymbol{v}}) \beta_{n,m}^{p,q} \\
&+ \sum_{n=0}^{\infty} \sum_{m=-n}^{n} e^{-in\pi/2} \frac{ku(nj_{n-1}(ku\tau) - (n+1)j_{n+1}(ku\tau))}{2n+1} Y_{nm}(\widehat{\boldsymbol{u}}) \\
&\times \sum_{p=0}^{\infty} \sum_{q=-p}^{p} e^{ip\pi/2} \frac{kv(pj_{p-1}(kv\tau) - (p+1)j_{p+1}(kv\tau))}{2p+1} Y_{pq}^*(\widehat{\boldsymbol{v}}) \beta_{n,m}^{p,q}) \Big|_{\tau=0}.
\end{aligned}
$$

Finally,

$$
\begin{aligned}
b_2 = &-(4\pi)^2 \Big(\frac{2k^2u^2e^{-i\pi}}{15} Y_{00}^*(\widehat{\boldsymbol{v}}) \sum_{m=-2}^{2} Y_{2m}(\widehat{\boldsymbol{u}}) \beta_{2,m}^{0,0} - \frac{k^2u^2}{3} Y_{00}(\widehat{\boldsymbol{u}}) Y_{00}^*(\widehat{\boldsymbol{v}}) \beta_{0,0}^{0,0} \\
&+ \frac{2k^2uv}{9} \sum_{m=-1}^{1} Y_{1m}(\widehat{\boldsymbol{u}}) \sum_{q=-1}^{1} Y_{1q}^*(\widehat{\boldsymbol{v}}) \beta_{1,m}^{1,q} \\
&+ \frac{2k^2v^2e^{i\pi}}{15} Y_{00}(\widehat{\boldsymbol{u}}) \sum_{q=-2}^{2} Y_{2q}^*(\widehat{\boldsymbol{v}}) \beta_{0,0}^{2,q} - \frac{k^2v^2}{3} Y_{00}(\widehat{\boldsymbol{u}}) Y_{00}^*(\widehat{\boldsymbol{v}}) \beta_{0,0}^{0,0} \Big).
\end{aligned}
$$

Bibliography

[1] A. G. Zajic and G. L. Stuber, "3-D MIMO mobile-to-mobile channel simulation," in *Mobile and Wireless Communications Summit, 2007. 16th IST*, July 2007, pp. 1–5.

[2] A. S. Akki and F. Haber, "A statistical model of mobile-to-mobile land communication channel," *IEEE Trans. Veh. Technol.*, vol. 35, no. 1, pp. 2–7, Feb. 1986.

[3] M. Heni and R. Bouallegue, "Performance analysis of a proactive protocol for mobile ad hoc networks with JiST-SWANS," in *Mediterranean Microwave Symposium (MMS), 2011 11th*, Sept. 2011, pp. 189–192.

[4] G. S. Khekare and A. V. Sakhare, "A smart city framework for intelligent traffic system using VANET," in *Automation, Computing, Communication, Control and Compressed Sensing (iMac4s), 2013 International Multi-Conference on*, 2013, pp. 302–305.

[5] L. Verhoeff, D. J. Verburg, H. A. Lupker, and L. J. J. Kusters, "VEHIL: a full-scale test methodology for intelligent transport systems, vehicles and subsystems," in *Intelligent Vehicles Symposium, 2000. IV 2000. Proceedings of the IEEE*, 2000, pp. 369–375.

[6] W. Xiang, P. Richardson, and J. Guo, "Introduction and preliminary experimental results of wireless access for vehicular environments (WAVE) systems," in *Mobile and Ubiquitous Systems: Networking and Services, 2006 Third Annual International Conference on*, July 2006, pp. 1–8.

[7] A. Goldsmith, *Wireless Communications*, vol. 93, Cambridge University Press, New York, 1st edition, 2005.

[8] P. Almers, E. Bonek, A. Burr, N. Czink, M. Debbah, V. Degli-Esposti, H. Hofstetter, P. Kyösti, D. Laurenson, G. Matz, A. F. Molisch, C. Oestges, and H. Özcelik, "Survey of channel and radio propagation models for wireless MIMO systems," *EURASIP J. Wirel. Commun. Netw.*, vol. 2007, pp. 56–56, Jan. 2007.

[9] A. S. Akki, "Statistical properties of mobile-to-mobile land communication channels," *IEEE Trans. Veh. Technol.*, vol. 43, no. 4, pp. 826–831, Nov. 1994.

[10] M. Patzold, B. O. Hogstad, and N. Youssef, "Modeling, analysis, and simulation of MIMO mobile-to-mobile fading channels," *IEEE Trans. Wireless Commun.*, vol. 7, no. 2, pp. 510–520, Feb. 2008.

[11] A. G. Zajic and G. L. Stuber, "Space-time correlated mobile-to-mobile channels: Modelling and simulation," *IEEE Trans. Veh. Technol.*, vol. 57, no. 2, pp. 715–726, Mar. 2008.

[12] G. Acosta-Marum and M. A. Ingram, "Six time- and frequency- selective empirical channel models for vehicular wireless lans," *Vehicular Technology Magazine, IEEE*, vol. 2, no. 4, pp. 4–11, Dec. 2007.

[13] X. Cheng, C. X. Wang, D. I. Laurenson, S. Salous, and A. V. Vasilakos, "An adaptive geometry-based stochastic model for non-isotropic MIMO mobile-to-mobile channels," *IEEE Trans. Wireless Commun.*, vol. 8, no. 9, pp. 4824–4835, Sept. 2009.

[14] A. G. Burr, "Capacity bounds and estimates for the finite scatterers mimo wireless channel," *IEEE J. Sel. Areas Commun.*, vol. 21, no. 5, pp. 812–818, June 2003.

[15] M. Debbah and R. R. Muller, "MIMO channel modeling and the principle of maximum entropy," *IEEE Trans. Inf. Theory*, vol. 51, no. 5, pp. 1667–1690, May 2005.

[16] A. M. Sayeed, "Deconstructing multiantenna fading channels," *IEEE Trans. Signal Process.*, vol. 50, no. 10, pp. 2563–2579, Oct. 2002.

[17] D. S. Shiu, G. J. Foschini, M. J. Gans, and J. M. Kahn, "Fading correlation and its effect on the capacity of multielement antenna systems," *IEEE Trans. Commun.*, vol. 48, no. 3, pp. 502–513, Mar. 2000.

[18] W. Weichselberger, M. Herdin, H. Ozcelik, and E. Bonek, "A stochastic MIMO channel model with joint correlation of both link ends," *IEEE Trans. Wireless Commun.*, vol. 5, no. 1, pp. 90–100, Jan. 2006.

[19] C. Balanis, *Advanced Engineering Electromagnetics*, John Wiley and Sons, New York, USA, 1999.

[20] J. Maurer, T. Fuegen, M. Porebska, T. Zwick, and W. Wiesbeck, "A ray-optical channel model for mobile to mobile communications," *COST 2100 4th MCM, COST 2100 TD(08) 430, Wroclaw, Poland*, Feb. 2008.

[21] A. F. Molisch, "A generic model for MIMO wireless propagation channels in macro- and microcells," *IEEE Trans. Signal Process.*, vol. 52, no. 1, pp. 61–71, Jan. 2004.

[22] M. Patzold, B. O. Hogstad, N. Youssef, and D. Kim, "A MIMO mobile-to-mobile channel model: Part I - the reference model," in *Personal, Indoor and Mobile Radio Communications, 2005. PIMRC 2005. IEEE 16th International Symposium on*, Sept. 2005, vol. 1, pp. 573–578.

[23] G. J. Byers and F. Takawira, "Spatially and temporally correlated MIMO channels: modeling and capacity analysis," *IEEE Trans. Veh. Technol.*, vol. 53, no. 3, pp. 634–643, May 2004.

[24] A. G. Zajic and G. L. Stuber, "Simulation models for MIMO mobile-to-mobile channels," in *Military Communications Conference, 2006. MILCOM 2006. IEEE*, Oct. 2006, pp. 1–7.

[25] G. Bakhshi, R. Saadat, and K. Shahtalebi, "A modified two-ring reference model for mimo mobile-to-mobile communication channels," in *Telecommu-*

nications, 2008. IST 2008. International Symposium on, Aug. 2008, pp. 409–413.

[26] S. Wang, A. Abdi, J. Salo, H. M. El-Sallabi, J. W. Wallace, P. Vainikainen, and M. A. Jensen, "Time-varying MIMO channels: Parametric statistical modeling and experimental results," *IEEE Trans. Veh. Technol.*, vol. 56, no. 4, pp. 1949–1963, July 2007.

[27] C. Wei, H. Zhiyi, and Z. Lili, "A reference model for MIMO mobile-to-mobile fading channel," in *Wireless Communications, Networking and Mobile Computing, 2007. WiCom 2007. International Conference on*, Sept. 2007, pp. 228–231.

[28] X. Cheng, C.X. Wang, and D.I. Laurenson, "A geometry-based stochastic model for wideband MIMO mobile-to-mobile channels," in *Global Telecommunications Conference, 2009. GLOBECOM 2009. IEEE*, Dec. 2009, pp. 1–6.

[29] G. Bakhshi, K. Shahtalebi, and H.S. Rad, "A novel full-three-dimensional MIMO mobile-to-mobile channel reference model," in *Signal Processing and Communication Systems, 2009. ICSPCS 2009. 3rd International Conference on*, Sept. 2009, pp. 1–6.

[30] A. Chelli and M. Patzold, "A MIMO mobile-to-mobile channel model derived from a geometric street scattering model," in *Wireless Communication Systems, 2007. ISWCS 2007. 4th International Symposium on*, Oct. 2007, pp. 792–797.

[31] A. G. Zajic and G. L. Stuber, "A three-dimensional MIMO mobile-to-mobile channel model," in *Wireless Communications and Networking Conference, 2007. WCNC 2007. IEEE*, Mar. 2007, pp. 1883–1887.

[32] T. Aulin, "A modified model for the fading signal at a mobile radio channel," *IEEE Trans. Veh. Technol.*, vol. 28, no. 3, pp. 182–203, Aug. 1979.

[33] J. D. Parsons and A. M. D. Turkmani, "Characterisation of mobile radio signals: model description," *Communications, Speech and Vision, IEE Proceedings I*, vol. 138, no. 6, pp. 549–556, Dec. 1991.

[34] A. G. Zajic and G. L. Stuber, "3-D simulation models for wideband MIMO mobile-to-mobile channels," in *Military Communications Conference, 2007. MILCOM 2007. IEEE*, Oct. 2007, pp. 1–5.

[35] A. G. Zajic, G. L. Stuber, T. G. Pratt, and S. T. Nguyen, "Wideband MIMO mobile-to-mobile channels: Geometry-based statistical modeling with experimental verification," *IEEE Trans. Veh. Technol.*, vol. 58, no. 2, pp. 517–534, Feb. 2009.

[36] D. Gesbert, H. Bölcskei, D. A. Gore, and A. J. Paulraj, "Outdoor MIMO wireless channels: Models and performance prediction," *IEEE Trans. Commun.*, vol. 50, no. 12, pp. 1926–1934, Dec. 2002.

[37] A. G. Zajic and G. L. Stuber, "A three dimensional parametric model for wideband MIMO mobile-to-mobile channels," in *Global Telecommunications Conference, 2007. GLOBECOM '07. IEEE*, Nov. 2007, pp. 3760–3764.

[38] H. Bischl and W. Schafer, "The 60 GHz mobile-to-mobile radio channel-fading statistics and estimated packet error rates," in *Vehicular Technology Conference, 1994 IEEE 44th*, June 1994, vol. 2, pp. 910–913.

[39] J. Maurer, T. Fugen, and W. Wiesbeck, "Narrow-band measurement and analysis of the inter-vehicle transmission channel at 5.2 GHz," in *Vehicular Technology Conference, 2002. VTC Spring 2002. IEEE 55th*, 2002, vol. 3, pp. 1274–1278.

[40] L. Cheng, B. E. Henty, D. D. Stancil, F. Bai, and P. Mudalige, "Mobile vehicle-to-vehicle narrow-band channel measurement and characterization of the 5.9 GHz dedicated short range communication (DSRC) frequency band," *IEEE J. Sel. Areas Commun.*, vol. 25, no. 8, pp. 1501–1516, Oct. 2007.

[41] I. Sen and D. W. Matolak, "Vehicle-vehicle channel models for the 5-GHz band," *IEEE Trans. Intell. Transp. Syst.*, vol. 9, no. 2, pp. 235–245, June 2008.

[42] G. Acosta, K. Tokuda, and M. A. Ingram, "Measured joint doppler-delay power profiles for vehicle-to-vehicle communications at 2.4 GHz," in *Global*

Telecommunications Conference, 2004. GLOBECOM '04. IEEE, Nov. 2004, vol. 6, pp. 3813–3817.

[43] A. Paier, J. Karedal, N. Czink, C. Dumard, T. Zemen, F. Tufvesson, A. Molisch, and C. Mecklenbrüker, "Characterization of vehicle-to-vehicle radio channels from measurements at 5.2 GHz," *Wireless Personal Commun.*, vol. 50, pp. 19–32, 2009, 10.1007/s11277-008-9546-6.

[44] S. Demmel, A. Lambert, D. Gruyer, A. Rakotonirainy, and E. Monacelli, "Empirical IEEE 802.11p performance evaluation on test tracks," in *Intelligent Vehicles Symposium (IV), 2012 IEEE*, June 2012, pp. 837–842.

[45] C. S. Patel, S. L. Stuber, and T. G. Pratt, "Simulation of Rayleigh faded mobile-to-mobile communication channels," in *Vehicular Technology Conference, 2003. VTC 2003-Fall. 2003 IEEE 58th*, Oct. 2003, vol. 1, pp. 163–167.

[46] N. Hajri, N. Youssef, and M. Patzold, "Simulation of mobile-to-mobile radio fading channels," in *Electronics, Circuits and Systems, 2005. ICECS 2005. 12th IEEE International Conference on*, Dec. 2005, pp. 1–4.

[47] B. O. Hogstad, M. Patzold, N. Youssef, and D. Kim, "A MIMO mobile-to-mobile channel model: Part ii - the simulation model," in *Personal, Indoor and Mobile Radio Communications, 2005. PIMRC 2005. IEEE 16th International Symposium on*, Sept. 2005, vol. 1, pp. 562–567.

[48] R. Wang and D. Cox, "Channel modeling for ad hoc mobile wireless networks," in *Vehicular Technology Conference, 2002. VTC Spring 2002. IEEE 55th*, 2002, vol. 1, pp. 21–25.

[49] T. Rappaport, *Wireless Communications: Principles and Practice*, IEEE Press, NY, Prentice Hall, 1996.

[50] G. L. Stuber, *Principles of Mobile Communications*, Kluwer Academic Publisher, 2nd Ed., 2001.

[51] Y. R. Zheng and C. Xiao, "Improved models for the generation of multiple uncorrelated Rayleigh fading waveforms," *IEEE Commun. Lett.*, vol. 6, no. 6, pp. 256–258, June 2002.

[52] A. G. Zajic and G. L. Stuber, "Three-dimensional modeling and simulation of wideband MIMO mobile-to-mobile channels," *IEEE Trans. Wireless Commun.*, vol. 8, no. 3, pp. 1260–1275, Mar. 2009.

[53] J. I. Smith, "A computer generated multipath fading simulation for mobile radio," *IEEE Trans. Veh. Technol.*, vol. 24, no. 3, pp. 39–40, Aug. 1975.

[54] D. J. Young and N. C. Beaulieu, "The generation of correlated Rayleigh random variates by inverse discrete fourier transform," *IEEE Trans. Commun.*, vol. 48, no. 7, pp. 1114–1127, July 2000.

[55] Y. H. Wang, Y. Wei, and J. Liu, "A new IFFT method for mobile-to-mobile rice channels in VANET," in *Wireless Communications Networking and Mobile Computing (WiCOM), 2010 6th International Conference on*, Sept. 2010, pp. 1–3.

[56] A. Petrolino, J. Gomes, and G. Tavares, "A mobile-to-mobile fading channel simulator based on an orthogonal expansion," in *Vehicular Technology Conference, 2008. VTC Spring 2008. IEEE*, May 2008, pp. 366–370.

[57] T. A. Lamahewa, T. D. Abhayapala, R. A. Kennedy, and J. T. Y. Ho, "Space-time cross correlation and space-frequency cross spectrum in non-isotropic scattering environments," in *Proc. IEEE Int. Conf. on Acoustics, Speech, and Signal Proc., (ICASSP'06)*, Toulouse, France, May 2006, vol. IV, pp. 609–612.

[58] D. Colton and R. Kress, *Inverse Acoustic and Electromagnetic Scattering Theory*, vol. 93, Springer, New York, 2 edition, 1998.

[59] R. A. Kennedy, P. Sadeghi, T. D. Abhayapala, and H. M. Jones, "Intrinsic limits of dimensionality and richness in random multipath fields," *IEEE Trans. Signal Process.*, vol. 55, no. 6, pp. 2542–2556, June 2007.

[60] T. A. Lamahewa, R. A. Kennedy, T. D. Abhayapala, and T. Betlehem, "MIMO channel correlation in general scattering environments," *Proc. 7th Australian Communication Theory Workshop, AusCTW'06*, pp. 93–98, Feb. 2006.

[61] J. Salz and J. H. Winters, "Effect of fading correlation on adaptive arrays in digital mobile radio," *IEEE Trans. Veh. Technol.*, vol. 42, no. 4, Nov. 1994.

[62] M. Kalkan and R. H. Clarke, "Prediction of the space frequency correlation function for base station diversity reception," *IEEE Trans. Veh. Technol.*, vol. VT-46, no. 1, Feb. 1997.

[63] K. I. Pedersen, P. E. Mogensen, and B. H. Fleury, "Power azimuth spectrum in outdoor environment," *IEE Electronics Letters*, vol. 33, no. 18, Aug. 1997.

[64] A. Abdi, J. A. Barger, and M. Kaveh, "A parametric model for the distribution of the angle of arrival and the associated correlation function and power spectrum at the mobile station," *IEEE Trans. Veh. Technol.*, vol. 51, no. 3, May 2002.

[65] P. D. Teal, T. D. Abhayapala, and R. A. Kennedy, "Spatial correlation for general distributions of scatterers," *IEEE Signal Process. Lett.*, vol. 9, no. 10, pp. 305–308, Oct. 2002.

[66] T. D. Abhayapala, T. S. Pollock, and R. A. Kennedy, "Characterization of 3D spatial wireless channels," in *Proc. IEEE Vehicular Technology Conference, VTC'03-Fall*, Orlando, Florida, USA, Oct. 2003, vol. 1, pp. 123–127.

[67] K. V. Mardia and P. E. Jupp, *Directional Statistics*, Wiley Series in Probability and Statistics. John Wiley and Sons, 2000.

[68] P. H. Leong, T. A. Lamahewa, and T. D. Abhayapala, "Framework to calculate level-crossing rate and average fade duration in two-dimensional and three-dimensional scattering environments," *IET Commun.*, vol. 6, no. 15, pp. 2474–2479, 2012.

[69] X. Cheng, C. X. Wang, D. I. Laurenson, H. H. Chen, and A. V. Vasilakos, "Space-time-frequency characterization of non-isotropic MIMO mobile-to-mobile multicarrier ricean fading channels," in *Wireless Communications and Mobile Computing Conference, 2008. IWCMC '08. International*, 2008, pp. 994–999.

[70] T. M. Wu and C. M. Kuo, "3-D space-time-frequency correlation functions of mobile-to-mobile radio channels," in *Vehicular Technology Conference, 2007. VTC2007-Spring. IEEE 65th*, 2007, pp. 334–338.

[71] T. A. Lamahewa, T. D. Abhayapala, R. Iqbal, and C. Athaudage, "A framework to calculate space-frequency correlation in multi-carrier systems," *IEEE Trans. Commun.*, vol. 9, pp. 1825–1831, June 2010.

[72] R. B. Ertel and J. H. Reed, "Angle and time of arrival statistics for circular and elliptical scattering models," *IEEE J. Sel. Areas Commun.*, vol. 17, no. 11, pp. 1829–1840, 1999.

[73] R. Janaswamy, "Angle and time of arrival statistics for the Gaussian scatter density model," *IEEE Trans. Wireless Commun.*, vol. 1, no. 3, pp. 488–497, 2002.

[74] A. Y. Olenko, K. T. Wong, and M. Abdulla, "Analytically derived toa-doa distributions of uplink/downlink wireless-cellular multipaths arisen from scatterers with an inverted-parabolic spatial distribution around the mobile," *IEEE Signal Process. Lett.*, vol. 12, no. 7, pp. 516–519, July 2005.

[75] A. Abdi, K. Wills, H. A. Barger, M. S. Alouini, and M. Kaveh, "Comparison of the level crossing rate and average fade duration of Rayleigh, Rice and Nakagami fading models with mobile channel data," in *52nd Vehicular Technology Conference, 2000. IEEE VTS-Fall VTC 2000*, 2000, vol. 4, pp. 1850–1857.

[76] A. G. Zajic, G. L. Stuber, T. G. Pratt, and S. Nguyen, "Envelope level crossing rate and average fade duration in mobile-to-mobile fading channels," in *IEEE International Conference on Communications, 2008. ICC '08.*, May 2008, pp. 4446–4450.

[77] A. G. Zajic and G. L. Stuber, "Statistical properties of wideband MIMO mobile-to-mobile channels (special paper)," in *Wireless Communications and Networking Conference, 2008. WCNC 2008. IEEE*, Apr. 2008, pp. 763–768.

[78] B. Talha and M. Patzold, "Level-crossing rate and average duration of fades of the envelope of mobile-to-mobile fading channels in cooperative networks under line-of-sight conditions," in *Global Telecommunications Conference, 2008. IEEE GLOBECOM 2008. IEEE*, Dec. 2008, pp. 1–6.

[79] B. Talha and M. Patzold, "Level-crossing rate and average duration of fades of the envelope of mobile-to-mobile fading channels in K-parallel dual-hop relay networks," in *Wireless Communications Signal Processing, 2009. WCSP 2009. International Conference on*, Nov. 2009, pp. 1–5.

[80] X. Cheng, C. X. Wang, D. I. Laurenson, and A. V. Vasilakos, "Second order statistics of non-isotropic mobile-to-mobile Ricean fading channels," in *IEEE International Conference on Communications, 2009. ICC '09.*, June 2009, pp. 1–5.

[81] M. Patzold, U. Killat, and F. Laue, "An extended Suzuki model for land mobile satellite channels and its statistical properties," *IEEE Trans. Veh. Technol.*, vol. 47, no. 2, pp. 617–630, May 1998.

[82] S. O. Rice, "Mathematical analysis of random noise," *Bell Syst. Tech. J.*, pp. 46–156, Jan. 1945.

[83] W. C. Jakes, *Microwave Mobile Communications*, John Wiley, New York, NY, 1974.

[84] N. Youssef, T. Munakata, and M. Takeda, "Fade statistics in Nakagami fading environments," in *IEEE 4th International Symposium on Spread Spectrum Techniques and Applications Proceedings, 1996*, Sept. 1996, vol. 3, pp. 1244–1247.

[85] J. T. Y. Ho, "A novel velocity estimator based on closed form spectral moment of the received signal," in *Communications, 2005. ICC 2005. 2005 IEEE International Conference on*, 2005, vol. 4, pp. 2195–2199.

[86] A. G. Zajic, "Estimation of mobile velocities and direction of movement in mobile-to-mobile wireless fading channels," *IEEE Trans. Veh. Technol.*, vol. 61, no. 1, pp. 130–139, 2012.

[87] M. D. Austin and G. L. Stuber, "Velocity adaptive handoff algorithms for microcellular systems," *IEEE Trans. Veh. Technol.*, vol. 43, no. 3, pp. 549–561, 1994.

[88] A. Abdi and M. Kaveh, "A new velocity estimator for cellular systems based on higher order crossings," in *Signals, Systems amp; Computers, 1998. Conference Record of the Thirty-Second Asilomar Conference on*, 1998, vol. 2, pp. 1423–1427.

[89] C. Tepedelenlioglu and G. B. Giannakis, "On velocity estimation and correlation properties of narrow-band mobile communication channels," *IEEE Trans. Veh. Technol.*, vol. 50, no. 4, pp. 1039–1052, 2001.

[90] A. Freedman, "Velocity estimation of cellular terminals in urban environment using ray tracing," in *Positioning Navigation and Communication (WPNC), 2012 9th Workshop on*, 2012, pp. 206–211.

[91] A. Chelli and M. Patzold, "The impact of fixed and moving scatterers on the statistics of MIMO vehicle-to-vehicle channels," in *Vehicular Technology Conference, 2009. VTC Spring 2009. IEEE 69th*, 2009, pp. 1–6.